Proton dynamics in ultrathin GdO_xH_y films for magneto-ionics

by

Sara Sheffels

B.S., Stanford University (2016)
M.S., Stanford University (2017)

Submitted to the Department of Materials Science and Engineering
in partial fulfillment of the requirements for the degree of

Doctor of Philosophy in Materials Science and Engineering

at the

MASSACHUSETTS INSTITUTE OF TECHNOLOGY

June 2023

Proton dynamics in ultrathin GdO_xH_y films for magneto-ionics

by

Sara Sheffels

Submitted to the Department of Materials Science and Engineering
on May 19, 2023, in partial fulfillment of the
requirements for the degree of
Doctor of Philosophy in Materials Science and Engineering

Abstract

Dynamic tuning of materials properties with simple voltage control is desirable for a variety of applications, from magnetic memory, to neuromorphic computing, to solid state pixels and optical circuit components. Metal oxides can conduct ionic current, allowing their properties and those of adjacent materials to be controlled through voltage control of ion transport and electrochemical reactions. This thesis focuses on protonic defects in gadolinium oxide and gadolinium hydroxide (GdO_xH_yy). Protons are mobile in this oxide at room temperature, and hydrogen incorporation can control a variety of materials properties, making these devices a promising platform for thin film solid state ionic devices with very simple and robust architectures. However, the proton transport and hydrogen storage properties of GdO_xH_y are not sufficiently well understood to determine the limits and optimal operation conditions for this material platform. Additionally, the mixed ionic and electronic conductivity of the material poses challenges for measuring these properties. This thesis sheds light on proton dynamics in nanoscale GdO_xH_y films in order to understand proton conductivity and hydrogen storage. The work investigates the effects of hydration and gating on the structure of GdO_xH_y films and devices, measures the devices' electrical and electrochemical properties, and focuses on applications in magneto-ionics, where voltage control of protons is used to toggle the magnetic properties of a ferromagnetic or ferrimagnetic layer.

Acknowledgments

I would like to thank Professor Caroline Ross for serving on my committee, for allowing me to learn from your teaching and leadership style in 3.091, and for providing a much more realistic view of the timeline and goals for my thesis work than anyone else (including me).

I would like to thank Professor Harry Tuller for serving on my committee and for keeping my work grounded in an understanding of defects in ceramics and electrochemical techniques. I thank him in particular for introducing me to Dynamic IV Analysis, a technique developed in his research group, and for various other collaborations over the years.

I would like to thank my advisor, Professor Geoff Beach, for the freedom he gave me to dive deeper into a topic that was relatively new to the research group and the grace he gave me as I tried and failed many times at coming up with experimental techniques that could probe the device electrochemistry. Geoff is amazing at crafting the flow of an explanation or argument, and I have learned a lot from observing how teaches and explains research. He is also a stickler for font sizes, line weights, and tick marks on plots – I have used the "Geoffify plots" method I made in Python four years ago on every plot I've made in grad school and will continue to use it in the future, because, let's be real, Geoff is right, they do look better that way!

Thanks to past and present members of the Beach group and other collaborators at MIT – thanks to AJ, Mantao, Alex, Usama, and Sunho for collaborating on our magneto-ionics projects, as well as Lucas, Max, Ethan, Felix, Can, Angela, Kai, Jason, Sasha, Ivan, Siying, Daniel, Don, Jonas, Maarten, Cassie, Liza, Byunghun, Pooja, Allison, and Michael.

I would like to thank the DMSE and shared facility staff at MIT who have helped me with my research, including David, Brian, Colin, Mike, Geetha, Meri, Shaymus, Charlie, and Jordan. Thanks to Mike also for running MADMEC and giving me and my PHAntastic co-conspirators the opportunity to play with polymers for a while.

Thanks a million to the amazing researchers whom I had the pleasure of working

with at the NIST Center for Neutron Research. You all kept me and my research going at key points in my grad school career and pushed me to keep at it even amid messy inconclusive data, devices that never seemed to work how they should during beamtime, and a reactor shutdown. Thank you to Joe, Julie, Purnima, Shin, and especially Alex for your collaboration and camaraderie!

Thanks to Ty, Lily, and Margaret for being the best study-buddies-turned-actual-friends I could ask for and for supporting me from afar this past year. I don't think any of us are actually researching hydrogen anymore; maybe we should rethink the group chat name!

Thanks to the members of the MIT Women's Volleyball Club for keeping me in good shape and good spirits for much of my time in grad school. I'd like to thank our coaches Tony and Max in particular for all the time they put into making the club a good experience for us and challenging me to be a better player and teammate.

Thank you to my union comrades for everything these past 3 years. I am so proud of what we've accomplished together to make MIT a better place for ourselves and for future grad students, and I consider the skills and memories that I've built alongside y'all to be some of the most meaningful parts of my time at MIT. Thank you to Jeff and Ki-Jana for getting me started on this path; I really look up to you as organizers. Thanks to the rest of the DMSE crew, Sophie, Serita, Nadia, Ashutosh, Lauren, and Grace, as well as our lovely staff members Maddie and Royce. I also want to shout out the UE staff and other organizers who mentored me during the lead-up to our election – I learned so much from John, Matt, Brian, Tristan, Lyndsey, Valentina, Townes, and Husayn.

Thanks to my extended dance family; you provided much-needed spaces for me to take a break from my MIT life and realize that there is a lot more to life than being a scientist. Thanks in particular to Lucas-Michael for seriousness and levity in equal measure (in dance and in D&D), for giving me space to come out of my shell, and for being the cheerleader I never knew I wanted; to Harsh for countless interesting event invitations and for epic lyrical dances that make my heart sing; to Ken for being my dance-organizing mentor and for always offering patient support and 1-1 dancing; and

to Alex for cozy dance weekends and many concerts and conversations. Thanks also to anyone who ever came to a Waltz @ MIT event at Ashdown and to Alborz and Rose for keeping that dance going. I look forward to dancing the night away with you all much more often once this thesis is submitted.

Thanks to Govind for being my support system for the first few years of grad school and weathering the beginning of the pandemic (as well as a lot of personal growth) together. I'm really grateful to have had that time with you.

Thanks to Gabe for helping me talk through the ups and downs of grad school and other life changes, and for sharing the ups and downs of your life with me too. Thank you for being you and becoming even you-er.

Thanks to Kunal for a lot of ice cream, dances, nerding out about dance, nerding out about being nerds, and judicious grad school advice. I think you've more than paid me back for all the work I put in to get you through your last couple years of grad school!

Thanks to Omari for your steadfast support and for always adjusting your date night ideas to match the time and energy I had available. Thanks for taking me in when COVID hit, for taking me out when you knew I needed more dance in my life, for new experiences and mundane experiences together, and for being such a powerful community-building force.

Thanks to Dylan for talking me through my research problems countless times, helping me understand and regulate my motivation and my work habits, and sometimes literally putting my hands back on the keyboard to keep me on task. Even more, though, thank you for expanding my ideas about myself. I am so looking forward to building stuff and learning with you.

Thanks to David for providing motivation, taking care of me, and making me work when I needed to work during my last few semesters. You have been so good to me, and I look forward to co-working on bigger and better projects.

Thanks to Miel for being my perpetual travel buddy and providing a little bit of home and family connection in Boston. It has been so cool to watch your hard work pay off these past few years!

Thanks to Erin for being my main role model my entire life. I think I'm finally about to deviate from your path!

Thanks to Christopher for helping me with my homework for mechanical properties of materials class and for doing all the work to make my dream house come to fruition in Terraria.

Thanks to Grandma Pauline for all the advice on research, writing, and behavior modification you have given me these past few years. You have always reminded me that creativity, artistry, and compassion are important parts of my life and work.

Thanks to my dad for being my original engineering mentor and for passing his curiosity about all the cool science and tech in the world onto me. He would have thought my research was cool too. I'm sad I didn't get to share it with him, but I know he would be really proud of me.

Thanks to my mom for always keeping track of what I'm up to, what research problems I'm having and helping me talk through them from afar. You have always been there for me to call on when I need it, and often when I didn't realize I needed it. Your unconditional love and support mean so much to me, and it has been inspiring to see you grow and adapt over the past 6 years as well. I love you!

Contents

List of Figures

Chapter 1

Introduction

Simple voltage control of ion movement can lead to control of a variety of properties that are useful in devices, opening up the possibilty of "voltage programmable materials".[9] Ionic movement can change the properties of the oxide itself (e.g. optical properties[6], resistivity [13, 14, 15, 16]) or can be used to change properties of adjacent materials (e.g. switching the magnetization of an adjacent metal layer by conducting oxygen ions to the interface) [17]. Metal oxides have rich electrochemistry and tunable ionic and electronic conductivity, making them a promising platform for thin film solid state ionic devices with very simple and robust architectures – dramatic changes in properties can be achieved by voltage gating devices with a simple metal/oxide/metal structure. Their ease of processing and CMOS compatibility makes metal oxides strong candidate materials for next-generation devices for information storage and computing, sensing, energy generation (fuel cells), and energy storage (batteries).

Voltage control of magnetic films and interfaces using ionic transport, or magneto-ionics,[18, 17] has introduced the possibility of inducing large changes in magnetic properties using straightforward low-voltage gating. Magneto-ionic mechanisms have the potential to dramatically improve the energy efficiency of magnetic memories and spintronic devices.[19] This can be done through various mechanisms. One mechanism is modifying the energy barrier for switching the magnetization during writing (modifying the magnetic anisotropy of the magnetic layer being switched), making it

temporarily less energy intensive to write the bit and then using ionic control to increase the energy barrier (increase magnetic anisotropy) after writing, setting the bit back to a nonvolatile state. Magneto-ionic control can also be used directly to switch magnetization direction by 180°.[12] A variety of ions have been used, most notably oxygen, [18, 17, 20, 21] lithium, [22] hydrogen, [21, 4, 10, 23] and nitrogen, [24] and large changes in properties such as magnetic anisotropy, [17, 25, 26, 4] magnetization, [17, 25, 22, 21, 26, 27] exchange bias, [20, 28] spin-orbit torque, [29, 30] and control of magnetic textures [12, 31] have been observed. Pt/Co/oxide stacks are common magneto-ionic devices, where the Co is the ferromagnetic layer, Pt provides the spin-orbit coupling needed to give the Co film perpendicular magnetic anisotropy (PMA), and the oxide is the ionic conductor and reservoir and also contributes to interfacial PMA through Co-O bonding.[32] Until recently, oxygen ion migration alone was assumed to cause ionically-induced property changes in Co/GdO_x. Previous work illuminates hydrogen's important role in the redox chemistry of these devices and establishes room temperature proton conduction as a fast mechanism for modulating the Co magnetism.[4, 10] Other works have highlighted the importance of humidity and protonic defects in memristors and magneto-ionic devices. [33, 34, 35, 13, 16]

Many ionic technologies already exist in commercial production – yttria-stabilized zirconia (YSZ) and CeO_2 in particular have been optimized as fast oxygen ion conducting electrolytes and are commonly used in commercial devices such as solid oxide fuel cells. Voltage control of magnetic [36] and electrical [14] properties of oxides through oxygen ion conduction has also been demonstrated. However, devices that rely on movement of oxygen ions commonly require high temperatures and are susceptible to structural degradation over time. This thesis instead focuses on hydrogen ion (proton) conduction. Protons are small and diffuse interstitially in most oxides, without affecting the material's crystal structure. Protons can be conducted through oxide ceramics relatively quickly at low temperatures due to their small size. Protonic defects are already present in some oxides at high levels due to reactions with water vapor in the atmosphere, and their concentration can be further enhanced by hydrating (humidifying) the oxide [37]. Protonic defects are also ubiquitous in many

materials and may not always require protective layers to prevent their diffusion into surrounding materials, making protonic devices more CMOS compatible than those that rely on alkali metal cations [38, 39]. All of these characteristics make protonic devices an appealing alternative to devices that rely on oxide or alkali ion conduction.

This work investigates proton transport and hydrogen storage in devices using GdO_xH_y as the proton conducting electrolyte. While most magneto-ionics work so far has focused on demonstrating new effects (i.e. using different ions, different ion conductors, or switching different properties of different magnetic layers), this thesis aims to shed light on the actual mechanisms through which magneto-ionic switching happens. In particular, we investigate where the protons and hydrogen go, what the proton conductivity of the GdO_xH_y is, how much of the current is protonic, and what limits the timescale for switching.

Chapter 2

Background

2.1 Ionic conduction in ceramics

Ceramics comprise lattices of cations and anions bound together by the strong attractive Coulomb forces experienced by oppositely charged particles. Ceramics can be found in a wide variety of crystal structures, and their crystal structure to a large extent determines their material properties (e.g. mechanical and magnetic properties). Defects within these materials also play a large role. Here we focus on electrical conduction in metal oxide ceramics due to large concentrations of point defects such as oxygen vacancies or interstitial ions. Metal oxide ceramics are often poor electronic conductors in bulk form due to the localization of electrons in their ionic bonds (although metallic and superconducting oxides do exist). Ionic defects, however, allow ions to move through the lattice, allowing metal oxides to conduct charge through ionic current.[40] In general, conductivity of a species through a material depends on the concentration of that species, its charge, and its mobility in the given environment (mobility can be related to diffusivity through the Einstein equation). In order to understand ion conductivity in oxides, then, we need to rely on a model for ion diffusion through ceramics. Diffusion occurs in ceramics when ionic species hop from site to site within the crystal lattice (or through the free volume in an amorphous ceramic). Diffusion through a crystalline lattice is modeled with a diffusion coefficient and an energy barrier that describe the relative difficulty of ion hopping from site to

site:

$$D = D_0 \exp \frac{-E_{\text{act}}}{\text{kT}}$$

Overall ionic diffusivity can be broken down into contributions from multiple ionic species and into bulk and grain boundary components. It is possible for grain boundary diffusivity to be either higher or lower than bulk diffusivity depending on the crystal structure and the density and degree of disorder in the grain boundary. Different contributions may therefore dominate in different temperature regimes. In general, defects can diffuse through two main mechanisms: vacancy or interstitial. For example, oxygen anions typically move through an oxide film using an oxygen vacancy ($\text{V}_\text{O}^{\bullet\bullet}$) diffusion mechanism. Oxygen vacancies in an oxide are in equilibrium with the gaseous oxygen in the environment, described with the following defect reaction:

$$\text{O}_\text{O}^x \rightarrow \text{V}_\text{O}^{\bullet\bullet} + \frac{1}{2}\text{O}_2 + 2\text{e}^-.$$

Doping with cations with a different valence from the native metal cation can also increase oxygen vacancy concentration and can therefore be used to increase ion conductivity. The following defect reaction between a metal cation (M, with an oxide formula of MO_2) and a dopant ion with lower valency (D, with an oxide formula DO) demonstrates this process:

$$\text{DO} \rightarrow \text{D}'_\text{M} + \frac{1}{2}\text{V}_\text{O}^{\bullet\bullet} + \text{O}_\text{O}^x.$$

Ions can also diffuse through an interstitial mechanism; interstitial defects are described by the following defect reaction (for ions with valence n):

$$\text{M}_\text{M}^\times \rightarrow \text{V}_\text{M}^{n-} + \text{M}_\text{i}^{n+}$$

These reaction demonstrate the interplay between ionic and electronic charge carriers in ceramics – in order to maintain charge neutrality, defects of various charge lead

to creation of oxygen vacancies or electronic carriers in the oxide. In general, the concentration of each species (and therefore the material's conductivity), including electronic carriers, can depend greatly on the other species present and the partial pressures of the gases present in the environment. This is what makes the electrical properties of ceramics so diverse and so tunable.

2.2 Oxygen ion conductors

Many established ionic technologies are based on oxygen ion conduction in ceramic materials. One of the most prominent and commercially developed is the solid oxide fuel cell. Oxygen ion based devices, including fuel cells, typically require temperatures ranging from 600°C to 1200°C for operation. Materials used as oxygen-conducting electrolytes must be stable under large temperatures and oxygen nonstoichiometry changes and must be made sufficiently dense to prevent mixing of the gas phase species on either side. Modern oxygen ion electrolytes have oxygen conductivities around 0.1 S cm^{-1} [41, 42]. Yttria-stabilized zirconia (YSZ) and doped ceria are most commonly used in commercial solid oxide fuel cells. Other established technologies involving oxygen ion conduction include oxygen separation membranes, oxygen sensors, and electryolysis cells. For all of these applications, oxide ion conductivity of 0.1 S cm^{-1} is desirable for device thicknesses around 1mm, although lower conductivities may be acceptable for thinner electrolyte layers [43]. The main disadvantage of using oxygen ions as the charge carrier in a technology is the high temperature generally required for operation. High temperature and large changes in temperature during operation can lead to materials degradation over many thermal cycles, as well as contributing to phase change instabilities and changes in morphology during operation that decrease the efficiency over time (such as grain growth and coarsening in ceramics, leading to lower catalytic activity in the electrode materials of devices operated at high temperatures). Using a different charge carrier that can have sufficiently high conductivity at lower temperature is therefore desirable, as the electrolyte and electrode materials need not be designed for such high temperature applications.

Oxygen ion control has also been used to manipulate magnetic properties including magnetization [44], exchange bias [20], and magnetic anisotropy [25, 17]. Voltage control of oxygen ions can change magnetic properties by changing the oxygen stoichiometry of the bulk or by changing the oxidation state at an interface. Magnetoelectric coupling through oxygen defects accompanied by resistive switching due to filament formation has also been observed [36]. Like solid oxide fuel cells and other oxygen-based ionic devices, devices based on this method of magnetic property switching have the disadvantage of structural instability and degradation over many cycles [4].

2.3 Proton conduction in oxides

2.3.1 Proton incorporation and conduction mechanism

Protonic defects ($OH_O^{\cdot}$) are created through the following reaction (given in Kroger-Vink notation) when oxides absorb water from the atmosphere[45, 46, 40]:

$$H_2O + O_O^x + V_O^{\cdot\cdot} \rightarrow 2OH_O^{\cdot} \tag{2.1}$$

Protons in oxides typically conduct through the Grotthuss mechanism, which consists of a reorientation step of the proton around the oxide ion and a hopping step to the next oxygen site.[46] Protonic defects are especially important in rare earth oxides, which have high pH and are very hygroscopic.[47] Rare earth oxides react with water to form hydroxides such as $Gd(OH)_3$.[48] This phase transition from oxide to hydroxide has been shown to change the ionic [2] and electrical[48] properties.

Hydrogen defect creation and diffusion has been studied in various oxides, including rare earth oxides [2]. Hydrogen is incorporated into the bulk of oxide ceramics through reactions at the oxide surface [35]. Hydrogen defects in oxides can be thought of as a hydroxide group on an oxygen site (or a proton attached to an oxygen sitting on an oxygen site) and can be written as such: $(OH)_O^{\bullet}$. Many oxides readily absorb water from the atmosphere and incorporate hydrogen into the lattice through the

following defect reaction [49]:

$$H_2O + V_O^{\bullet\bullet} + O_O^x \rightarrow 2(OH)_O^{\bullet}$$

In the presence of molecular hydrogen, the following defect reaction may also occur [1]:

$$H_2 + 2O_O^x \rightarrow 2(OH)_O^{\bullet} + 2e^-.$$

Protons can in general be transported as part of a larger molecule (e.g. NH_4^+, H_3O^+), termed the "vehicle mechanism", or independently as H^+, called the free-proton or Grotthuss mechanism, which was originally used to describe how hydrogen diffuses through liquid water. The Grotthuss mechanism is a common form of proton conduction in solid proton conductors [49] and is shown in Figure 2-1. In general, it refers to the transfer of a proton from one water molecule to the next through the exchange of a covalent bond with a hydrogen bond [50, 51]. In a crystalline oxide lattice, this means that hydrogen ions "hop" from one oxygen to the next, moving interstitially from oxygen site to oxygen site [2].

Solids may conduct protons in two different ways (or some combination of the two). The first is conduction through liquid layers or liquid-like regions surrounding the solid, which occurs in some hydrated polymers and in ceramics where a layer of water is adsorbed on each grain. The protonic transport in this case is identical to proton transport through liquid water. The second is hopping between crystallographic lattice sites in a material in which protons are bonded to oxygen ions. Some materials (e.g. solid acids or hydroxides) have a crystallographically fixed number of protons; the degree of acidity or basicity is determined by the strength of the anion-proton bond. This type of material becomes dehydrated at sufficiently high temperatures (usually 100-200°C). Conduction occurs when proton vacancies and/or interstitials form and protons hop between these sites. Solids that do not have hydrogen as part of their structure can also conduct protons if they are introduced as interstitial defects, meaning the incorporation of protons does not affect the crystal-

lographic structure of the solid and the protons can diffuse freely through the existing crystal [49]. Moisture does not always have the same effect on different metal oxides, or the same oxide with a different microstructure [52].

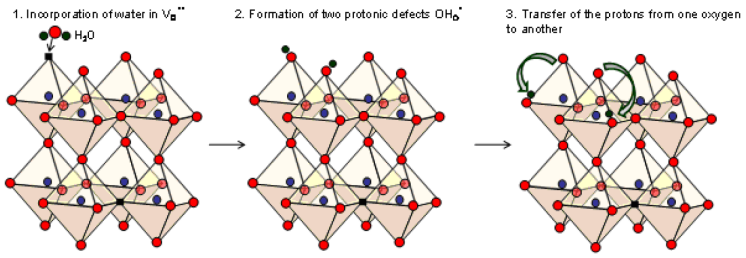

Figure 2-1: Schematic of hydrogen defect formation and the Grotthuss mechanism of proton transfer in an oxide ceramic [1]

2.3.2 Measurement of proton conductivity

The ionic conductivity of a material is usually measured using electrochemical impedance spectroscopy (EIS). In AC impedance spectroscopy, an AC voltage signal with an amplitude of approximately 10 mV is applied to a device, and the device impedance is measured at frequencies ranging from 10 MHz to 0.01 Hz. Measuring at a wide range of frequencies separates out all of the electrochemical and transport processes that happen within the device by the effective speed of the process, given by the RC time constant for each process. In a metal/oxide/metal device, therefore, one part of the impedance spectrum can be attributed to the ion conduction through the oxide electrolyte. From the measured resistance value and the device geometry, an ionic conductivity can be calculated [3]. Figure 2-2 shows a schematic of a typical Nyquist plot: a plot of the imaginary part of the impedance versus the real part over a range of frequencies. Impedance data can be fit to semicircles similar to this Nyquist plot schematic, and can be used to find a model circuit for an electrochemical system [53].

Plotting the ionic conductivity over a temperature range and with a range of different partial pressures of oxygen and water vapor reveals the different conduction regimes of an oxide material. It has been shown, for example, that doped gadolinium

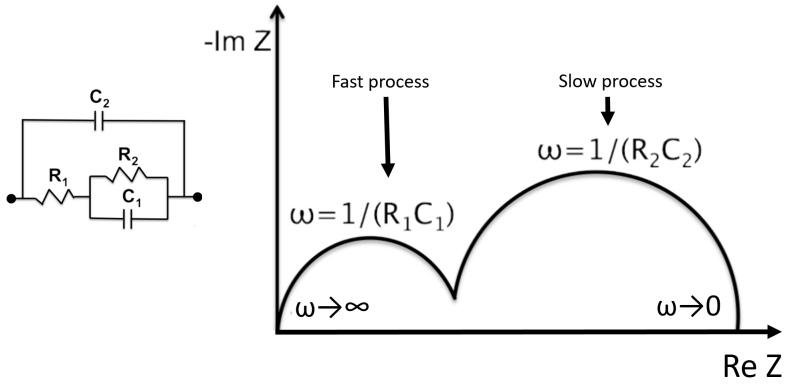

Figure 2-2: Features of a typical Nyquist plot, with the circuit that generates it shown on the left. The capacitances C_1 and C_2 can be calculated based on the frequency at which the peak of each semicircle occurs.

oxide near room temperatures is well into the proton conduction regime, and therefore, the ionic conduction can be attributed almost entirely to protons [2]. Similar measurements could be carried out to determine the conduction regimes and ionic conductivities for protons in different oxides. Figure 2-3 shows such Arrhenius plots that demonstrate the conduction regimes for doped gadolinium oxide. Grain boundary and bulk contributions may also be distinguished in the spectrum if their effective time constants are sufficiently different, which they are in many ceramics. Figure 2-4 shows data for gadolinium-doped ceria that demonstrates the relative contributions of bulk and grain boundary conduction at different temperatures.

2.3.3 Proton conducting perovskite oxides

The first proton conducting solid state materials were hydrous inorganic compounds; later, proton conducting polymers were developed and interest in proton-conducting metal oxide ceramics also developed [49]. Much of the current work in proton-conducting metal oxides is on perovskite materials, particularly $BaCeO_3$ (orthorhombic structure at room temperature) and $BaZrO_3$ (cubic structure at room temperature), and similar solid solutions doped with different cations [54]. $BaCeO_3$ has high proton conductivity but poor chemical stability, while $BaZrO_3$ has good stabil-

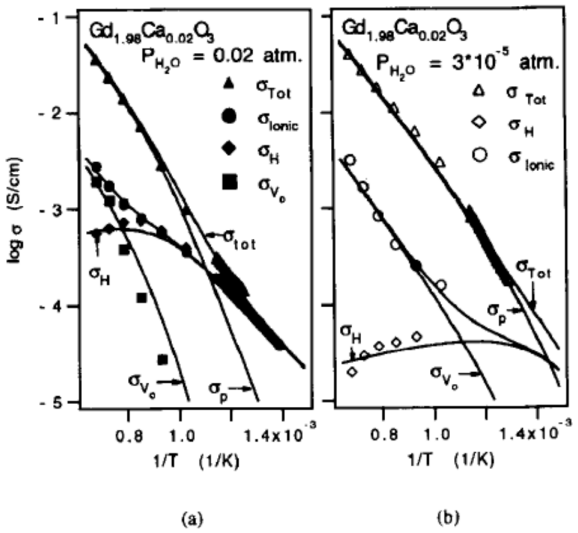

Figure 2-3: Plot of log of conductivity versus inverse temperature for Ca-doped gadolinium oxide in a) wet and b) dry atmosphere, showing proton conductivites of 10^{-4} S cm^{-1} at low temperatures. In the wet environment, proton conductivity (σ_{H}) clearly dominates at low temperatures [2].

ity but worse proton conductivity. Intermediate solid solutions, $BaCe_{0.8-x}Zr_xY_{0.2}O_{3-\delta}$ (BCZY) demonstrate desirable combinations of these properties, with proton conductivites on the order of 10^{-5} S cm^{-1} at 473 K[55]. Humidification (exposure to environment with high partial pressure of water vapor) has been found to improve the proton conductivity of perovskite oxides [54]. However, these perovskites have been found to exhibit large structural expansion and phase transitions upon hydration [56]. This phenomenon can lead to delamination at interfaces and degradation of the functional ceramic when used as a proton conductor in solid oxide fuel cells, electrolysis cells, and other devices. Other challenges with proton conducting perovskites include degradation due to cation segregation and coarsening, even at low temperatures. Perovskites can also exhibit chemical degradation in environments with high humidity or high partial pressure of CO_2, with the degree of degradation depending on the cation dopants and the structure of the perovskite [57]. Perovskite proton conductors have very high ionic conductivity compared to oxide ion conductivity in YSZ and ceria, so they can be operated around 300-500°C, which is much lower than the 600-1000°C required for oxide ion conductors. However, this temperature is still well

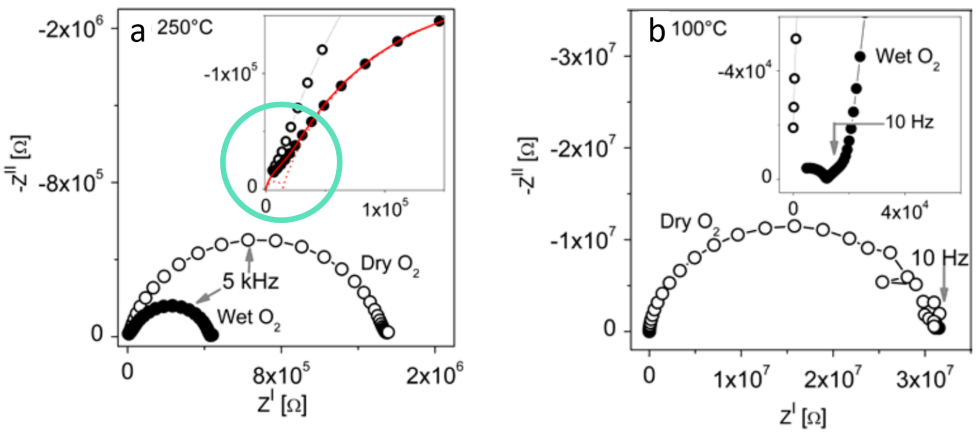

Figure 2-4: Measured Nyquist plots for gadolinium-doped ceria in wet (filled circle) and dry (open circle) oxygen environments at a) 250°C, where a small semicircle attributed to conduction through the bulk is highlighted in the green circle; b) 100°C, where the bulk contribution is no longer there (only one semicircle is found), indicating that bulk conduction is short-circuited through another conduction mechanism [3].

above room temperature, so there is still room for improvement in the development of room temperature devices. Proton-conducting oxides are fabricated using solid state processing or the Pechini (liquid mix) method, and their electrical properties are typically measured using EIS [55].

2.3.4 Proton conducting oxides in ionic devices

Devices that rely on ionic conduction in ceramics are not new; examples include lithium ion batteries (in which lithium ions are conducted through an electrolyte and lithium is stored in cathode and anode materials, which may also be ceramics), solid oxide fuel cells (in which oxygen ions, protons, or other ions are transported through an electrolyte to react with fuels and produce electricity), and gas sensors (which rely on ceramic materials' response to changing partial pressures of oxygen, water vapor, or other gases in the environment).

Some of the first ionic devices that knowingly relied on protonic defects were humidity sensors. The conductivity change of certain oxides in environments with different humidity has been well known for several decades, and had obvious applica-

tions in measurement of humidity. Some metal oxide humidity sensors relied on the conduction of protons through the chemisorbed hydroxyl layer and physisorbed water layer on the ceramic surface, while another type relied on the change in electronic conductivity caused by chemisorbed water molecules [58].

As mentioned above, perovskite oxides are increasingly being used in devices as proton conductors, especially as alternative materials to oxide-conducting ceramics for solid oxide fuel cells [59], electrolysis cells, and reversible solid oxide cells (which work both ways, producing electricity from fuel or vice versa). These materials work at lower temperatures than oxide ion conductors (although at higher temperatures than the proton-conducting polymers also sometimes used in fuel cells (PEMFCs), which have stablity problems of their own) and are referred to as high-temperature proton conductors (HTPCs) [60].

2.3.5 Gating

Gating can be achieved through simple application of a voltage across electrodes. This creates an electric field across the gated material. For nanoscale films (10-100 nm) and voltages on the order of 1 V, this electric field is $10^7 - 10^8$ V m^{-1}.

Ionic liquid gating is also of increasing interest for gating properties of oxides and other materials. Ionic liquids are capable of producing surface charge densities much greater than those possible with traditional solid oxide gate dielectric materials, and are therefore capable of producing phase transitions, defect generation and motion, and metal-insulator transitions in ceramics that would not be observable with traditional voltage gating. [61]. Ion gels are also used and have been demonstrated to produce surface charge carrier densities above 10^{14} cm^{-2}. Ion gel gating has been used to modulate properties including resistivity, magnetoresistance, and Curie temperature in oxides such as $La_{0.5}Sr_{0.5}CoO_{3-\delta}$ [62]. Gating of properties in oxides can be attributed to a buildup of charge carriers at the interface (electrostatic mechanism, which affects only the surface layer of the oxide), to electrochemical reactions (such as the formation of oxygen vacancies or the intercalation of hydrogen, which can change the properties of the whole film), or to a combination of both [63].

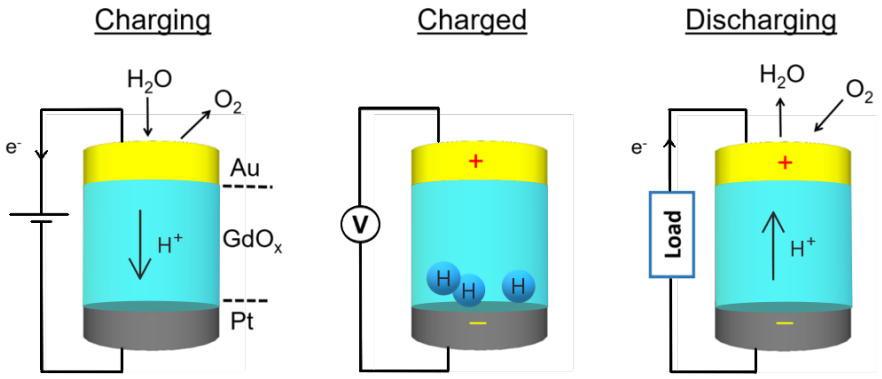

Figure 2-5: Illustration of the proton pumping mechanism of the GdO_x device under positive bias (charging), in the charged state with hydrogen stored at the bottom interface, and under negative bias (discharging). The device shown here is $Pt/GdO_xH_y/Au$.

2.3.6 Gating of GdO_x device

Prior works show that positively gating a $Pt/GdO_x/Au$ stack (the Au electrode adjacent to air at high potential) electrochemically splits water from the ambient water vapor and pumps protons into the GdO_x. The electric field drives protons to the back electrode (Pt), where it is reduced. The resulting neutral hydrogen is stored at the bottom interface (as H or H_2O depending on the chemistry of the bottom electrode or magnetic layer). Upon discharge, the process is reversed. Figure 2-5 illustrates the basic charging and discharging mechanisms for the proton pump.

The electrode reactions occurring are as follows:

$$\text{Anode (top electrode): } 2H_2O \rightarrow O_2 + 4e^- + 4H^+ \tag{2.2}$$

$$\text{Cathode (bottom electrode): } 4H^+ + 4e^- \rightarrow 4H \tag{2.3}$$

2.4 Protonic control of electrical, magnetic, and optical properties

2.4.1 Memristors and resistive switches

The resistivity change of various oxides has been demonstrated in memristors, which switch between an "off" (high-resistance) and "on" (low-resistance) state when ionic defects move to form regions with higher electronic conductivity under sufficiently high applied voltage (usually greater than 10^6 Vm^{-1}). Before the defect mechanism was discovered, it was observed that resistance switching occurs in virtually all transition metal oxides [64]. Hydrogen ion (proton) incorporation controlled with environmental humidity has been shown to affect the resistance of many oxides, including TiO_2 [65], SnO_2 [66], $BaTiO_3$ [67], and Al_2O_3 [68], which makes this effect extremely relevant in the field of memristors [35]. The mechanism by which protons affect the conductivity of the oxide can vary between oxides and between temperature and defect density regimes. Protons adsorbed on the surface can improve proton conduction; protons can also be incorporated into the bulk of the oxides when water molecules in the gas phase dissociate, are incorporated into the oxide at the surface, and diffuse into the bulk. Previously, it was often assumed that oxygen vacancies were the most important or only important species in memristive oxides; however, it has been shown recently that water and protonic defects at the surface are essential for memristance in $SrTiO_3$ due to the interaction between protonic defects, oxygen defects, and electronic carriers [34]. Since the importance of protons in memristive oxides has only been discovered recently, much more study is needed to fully understand their role.

2.4.2 Magnetic switching

Switching of the magnetic properties of metal layers through proton conduction has been achieved through two different mechanisms. In devices with an added magnetic layer at the back electrode, the hydrogen influences the magnetic properties by causing a redox reaction or diffusing into the magnetic material. In devices with an initially

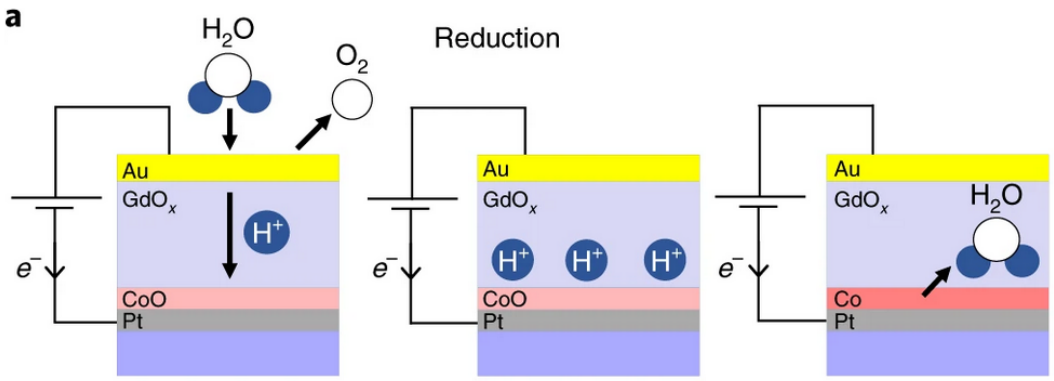

Figure 2-6: Switching of the Pt/CoO/GdO_xH_y/Au device from a non-magnetic (CoO) to a magnetic (Co) state. Protons pumped in during gating reduce the CoO to Co. Reprinted from Ref. [4].

oxidized Co layer (Pt/CoO/GdO_xH_y/Au), pumping in hydrogen reduces the CoO to Co.[4, 10] The reverse process happens under negative bias, with H_2O oxidizing the Co.[4] Figure 2-6 shows an initially CoO device in which the presence of water vapor allows for the reduction of cobalt oxide to cobalt. The MOKE data in Figure **??**, demonstrated by the appearance of the square magnetic hysteresis loop associated with the out-of-plane magnetization of the cobalt metal upon gating the device in atmospheres where water is present. It has been shown that water plays a key role in the oxidation of the cobalt layer through ion pumping – in this case, it is not the conduction of oxygen anions towards the cobalt layer that causes the oxidation, but rather the conduction of protons to the interface, which allows for the cobalt reduction reaction. The top electrode reaction is given by Equation 2.2. The bottom electrode reaction is as follows [4]:

$$\text{Cathode (bottom electrode): } 4H^+ + 2Co^{2+} + 2O^{2-} + 4e^- \rightarrow 2H_2O + 2Co \qquad (2.4)$$

This voltage-gated switching between cobalt (low resistance) and cobalt oxide (high resistance) via protonic defects has also been used to form a resistive switching device, demonstrating a potential method to couple electrical and magnetic properties [15].

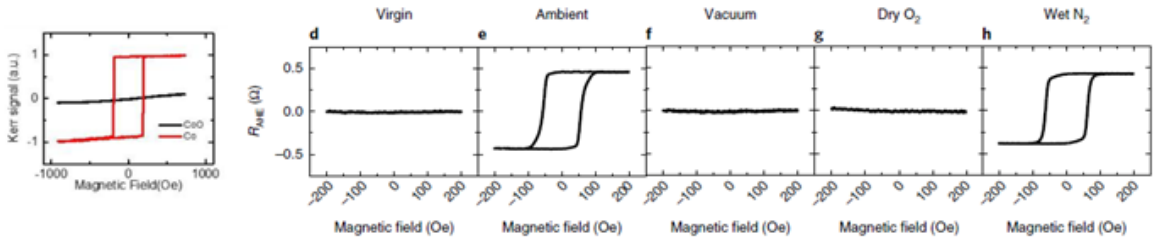

Figure 2-7: a) Polar Magneto-optic Kerr effect (MOKE) magnetic hysteresis loops for 1nm thick CoO and Co films, showing out-of-plane magnetization for the Co ("square" loop) and no magnetization for the CoO [5], b) hysteresis loops for Ta(4 nm)/Pt(3 nm)/Co(0.9 nm)/GdO_x(30 nm)/Au(3 nm) devices in d) virgin state, and after applying +3 V for 1000 s in e) ambient conditions, f) under vacuum, g) under dry O_2, or h) under wet N_2 [4].

For devices that have metallic cobalt during positive gating (Pt/Co/GdO_xH_y/Au), the presence of hydrogen at the oxide/metal interface can also switch the anisotropy of the magnetic layer between out-of-plane and in-plane, allowing for a switching of the *direction* of magnetization (rather than switching the the net magnetic moment on and off by converting the material to a nonmagnetic one through a redox reaction). This type of switching has been achieved in a solid state device using gadolinium oxide as a proton conducting material to switch the anisotropy of a cobalt thin film [4]. When a positive gate voltage is applied, hydrogen accumulates at the oxide/cobalt interface and the magnetization switches from perpendicular to in-plane. After the voltage is set to 0 V (grounded), the hydrogen diffuses away from the interface and perpendicular magnetic anisotropy (PMA) is recovered [4]. Switching of magnetic anisotropy upon changes in partial pressure of hydrogen gas has also been previously demonstrated in other ultrathin ferromagnetic films [69] and in multilayer stacks of ferromagnetic materials [70].

2.4.3 Optical switching and electrochromic devices

Electrochromic devices based on hydrogen intercalation have been demonstrated. One such device, based on tungsten oxide (WO_3), switches between the transparent, high-resistance oxide and the dark blue, electrically conductive protonated oxide (H_xWO_3)

using a transparent water-infiltrated nano-porous glass as a gate insulator [71]. The device exhibits good cyclability, and demonstrates that optical and electrical properties can be coupled.

Optical property switching due to hydrogen incorporation in gadolinium oxide has also been demonstrated. In a simple metal/oxide/metal crossbar device, when a positive gate voltage is applied, the water splitting reaction occurs at the top electrode and hydrogen is incorporated into the oxide in the form of interstitial protonic defects. The refractive index of the oxide changes with increasing proton concentration, changing the effective optical path length through the oxide. Figure 2-8 shows a schematic of the device and a demonstration of a color change from blue to green due to the refractive index change of gadolinium oxide upon hydration. Optical properties of an adjacent metal layer can also be reversibly switched by conducting hydrogen through the oxide and hydrogenating the metal, changing its refractive index [6]. This type of protonic device could have applications in display technologies and other photonics applications where modulating the refractive index is required.

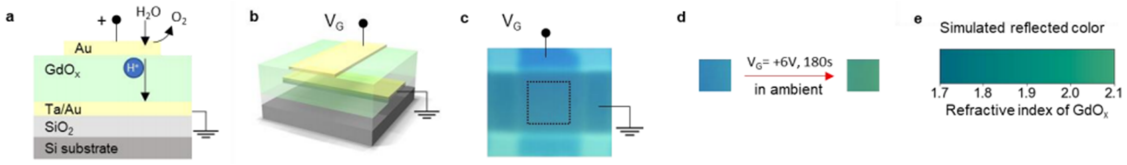

Figure 2-8: a) Schematic of the device showing the water splitting reaction at the top electrode and the incorporation of H+ into the GdOx, b) Schematic of the cross bar device architecture, c) image of the device before H+ incorporation, showing the original blue color of the device, d) image of the device before and after applying +6V for 180s, showing the color change from blue to green, e) simulation of the expected color change when the refractive index of GdOx is varied between 1.7 and 2.1.[6]

Chapter 3

Experimental Methods

3.1 Sample fabrication

3.1.1 Sputtering

Sputtering is a physical vapor deposition method for thin films. The sample substrate is placed in a vacuum chamber and pumped down to high or ultrahigh vacuum (10^{-5} to 10^{-8} Torr). An inert sputtering gas, usually argon, is pumped in (at around P=3.0 mbar) and a large voltage is applied across the sample and the target material. The argon is ionized to form a plasma, and the ions are accelerated towards the target material. The impact of the ions on the target material removes some of the target material, which travels towards the sample and sticks on the substrate surface. In this manner, a thin film of the target material is built up with a controlled growth rate on the substrate. DC magnetron sputtering employs a DC current to sputter an electrically conductive material (usually metals). RF sputtering involves an alternating sputtering current and is used for insulating materials (ceramics). Sputtering allows for nanometer scale control of the film thickness, as well as control over the morphology of the film through process parameters such as background pressure, argon pressure, oxygen pressure, current, and power.

3.1.2 Sample structure and patterning

The sample stacks used for the devices in this work are:

1. Ta/Pt/GdOx/Au. Ta is the adhesion layer that makes the rest of the stack stick to the substrate, Pt is the bottom electrode, GdOx is the ionic-conducting oxide, and Au is the top electrode.

2. Ta/Pt/Co/GdOx/Au. Ta is the adhesion layer, Pt is the bottom electrode, Co is the the magnetic layer, GdOx is the ionic-conducting oxide, and Au is the top electrode.

3. Ta/Pd/GdCo/Pd/GdOx/Au. Ta is the adhesion layer, Pd is the bottom electrode, GdCo is the the magnetic layer, Pd is the capping layer preventing oxidation of the GdCo, GdOx is the ionic-conducting oxide, and Au is the top electrode.

All devices are sputter deposited on p-doped Si substrate with 50nm of thermal oxide (SiO_2). The devices geometry is a crossbar structure, which typically consists of a back electrode stripe, a large area oxide deposition, and a top electrode stripe deposited perpendicular to the bottom electrode, forming a rectangular device at the intersection of the electrodes (see Figure 3-1. Patterning is done using shadow mask lithography, which involves putting a PEEK, acetal, or metal mask over the sample surface to allow deposition only in the desired areas. In general, due to the constraints on which materials can be sputtered together in our system and due to the number of different shadow masks that must be used to pattern the devices, three or four sputter runs (with two or three vacuum breaks) are required to make these devices:

1. Ta/Pt or Ta/Pd/GdCo/Pd back electrodes with bottom crossbar mask. The GdCo magnetic layer can be sputtered with the same mask as the rest of the back electrode since it is metallic and has a metallic Pd capping layer.

2. (for Ta/Pt/Co/GdOx/Au device only) Co/GdOx (GdOx here is a thin, 4 nm capping layer to prevent Co oxidation), sputtered with back electrode and large

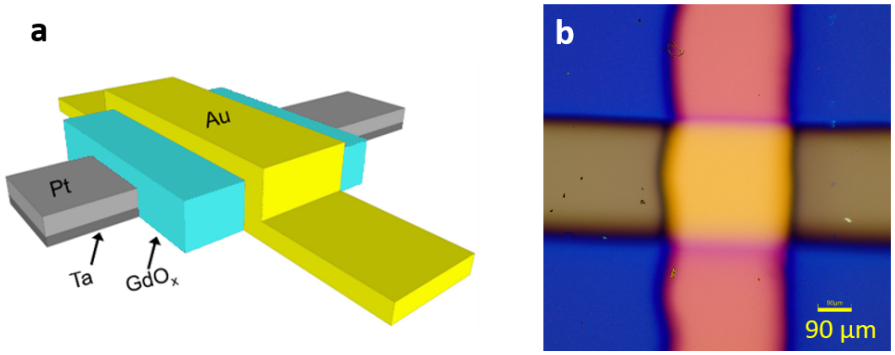

Figure 3-1: a) Schematic of the Pt/GdO_x/Au crossbar devices. b) Optical micrograph of one crossbar device.

area masks stacked on top of each other to prevent Co/GdOx deposition on the back electrode contact pads.

3. GdOx electrolyte layer (typically 20-40 nm) with large area mask.

4. Au top electrode with top crossbar mask.

3.2 Materials characterization

3.2.1 X-ray reflectometry

X-ray reflectometry (XRR) is a technique used to probe the electronic densities and thicknesses of the layers in a thin film stack. X-rays primarily interact with the electrons in a material; their scattering cross-section is roughly proportional to the electron density in a material. X-rays therefore interact more strongly with heavier elements and not very strongly with light elements such as hydrogen.

3.2.2 Polarized neutron reflectometry

Polarized neutron reflectometry (PNR) is another type of reflectometry and operates on many of the same principles as XRR. In this case, however, the incoming radiation is neutrons, which have wavelengths ranging from 10^{-14} to 10^{-8} m. Neutrons primar-

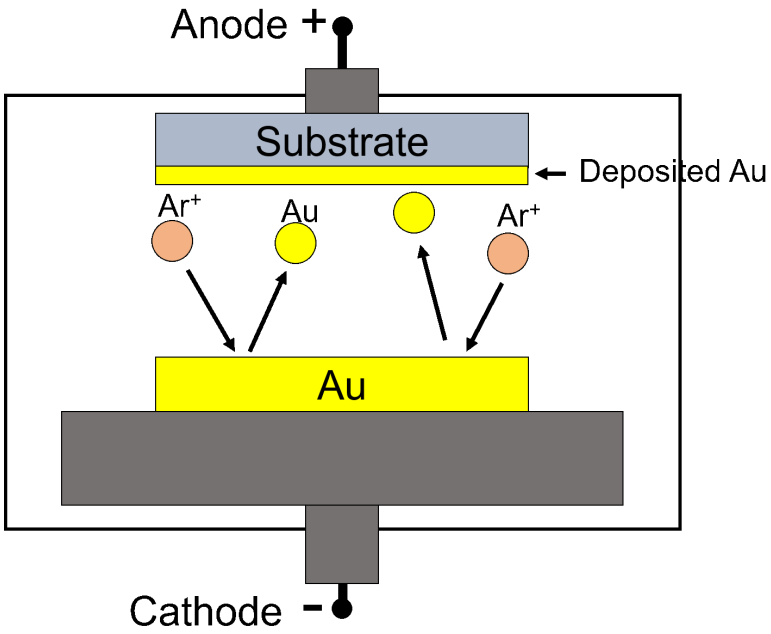

Figure 3-2: Schematic of the sputtering process for gold (Au).[5]

ily interact with the nuclei in a material (rather than the electron cloud), making this technique complementary to XRR.

3.2.3 Secondary ion mass spectrometry

Secondary ion mass spectrometry (SIMS) uses a focused ion beam to mill away the region of interest on the sample, measuring the mass of the ions that are ejected from the sample to determine their identity. It is a destructive method, so typically multiple devices must be used to show changes in device chemistry across different states or environments (rather than analyzing a single device in multiple states in series). Time-of-flight mass spectroscopy can be very sensitive to small mass differences, so SIMS can be used to distinguish between similar ions (e.g. those differing only by one H atom).

3.3 Electrical and electrochemical characterization

All electrical and electrochemical measurements were done using a Keithley 6430 source meter in a Lakeshore CPX-VF probe station. The probe station chamber can be pumped down to 10^{-4} mbar using a dry scroll pump. Gases such as N_2 (with purity >99%, dry or made wet by bubbling through a water bubbler) can be introduced directly into the chamber using a venting valve. Temperature was controlled using a Lakeshore temperature controller, built into the probe station.

3.3.1 Cyclic voltammetry

Cyclic voltammetry is a voltage sweep method used to determine properties of an electrochemical system, most notably the diffusivity of the relevant ionic species through the electrolyte and the voltages at which particular redox reactions (or steps in a reaction) occur. The voltage is swept at a specific rate (usually 1-500 mV/s) through the overpotentials at which the reactions of interest will occur. Consider the following general redox reaction:

$$\mathrm{Red} \rightarrow \mathrm{Ox} + n\mathrm{e}^- \tag{3.1}$$

As the voltage increases (becomes more anodic), the oxidation reaction(s) will proceed. As the reactant is used up, a diffusion layer is established between the electrode surface (low concentration of reactant) and the bulk of the electrolyte (bulk concentration of reactant). The concentration gradient in this diffusion layer determines the flux of the reactant to the electrode, and therefore also determines the magnitude of the reaction current. This gradient increases over time as more of the reactant is depleted, until the concentration of the reactant at the electrode reaches zero, at which point the steepness of the concentration gradient must decrease as the width of the diffusion layer increases farther into the electrolyte. This leads to a decrease in the reaction current, giving the characteristic peak in the cyclic voltammetry plot as the voltage is swept.

The Randles-Ševčik equation can be used to extract a diffusivity from measurements of peak current, i_{peak}, as a function of scan rate, ν (equation given for a room

temperature reaction):

$$i_{peak} = \left(2.69 \times 10^5 \text{ C mol}^{-1} \text{ V}^{-\frac{1}{2}}\right) n^{\frac{3}{2}} AC\sqrt{D\nu} \tag{3.2}$$

where n is the number of electrons transferred in the reaction, A is the electrode area, C is the concentration of the relevant ionic species, and D is the diffusivity of the ionic species. The linear relationship between i_{peak} and $\sqrt{\nu}$ described by the Randles-Ševčik equation is indicative of a reversible, diffusion-limited reaction.

3.3.2 Dynamic IV Analysis

Dynamic IV Analysis (DIVA) is a technique developed by Dr. Dmitri Kalaev and applied extensively in Professor Harry Tuller's research group at MIT, as a way to measure the mobility of ionic species in mixed ionic and electronic conductors (MIEC).[7, 8, 72] The technique assumes that there is one carrier of each type (e.g. electrons are the primary electronic carriers and oxygen ions are the primary ionic carrier) and relies on using electrodes that are ion-blocking to ensure that the number of ionic carriers is constant. A schematic of the working principle of DIVA in a device with oxygen vacancies as the primary ionic species is shown in Figure 3-3. A voltage sweep up to some low value (typically under 1V) is applied and the current is recorded (this current is entirely electronic due to the ion-blocking electrodes). Under bias, the charged ionic defects are accelerated in the electric field and build up at one end, leaving an area deficient in those defects at the other electrode. In the case of oxygen ions, a ceramic deficient in oxygen ions has a higher electronic conductivity than the stoichiometric phase. This movement of oxygen ions and vacancies thus creates a region of high electronic conductivity and a region of lower electronic conductivity in series, which overall lowers the electronic conductivity. The result is an effective negative resistance as the voltage is swept, leading to a peak in the IV curve. Example data is shown in Figure 3-4. These peaks should be symmetric (a negative voltage sweep should produce the same gradient in ion concentration at the opposite electrodes, resulting in the same peak in electronic current for positive and

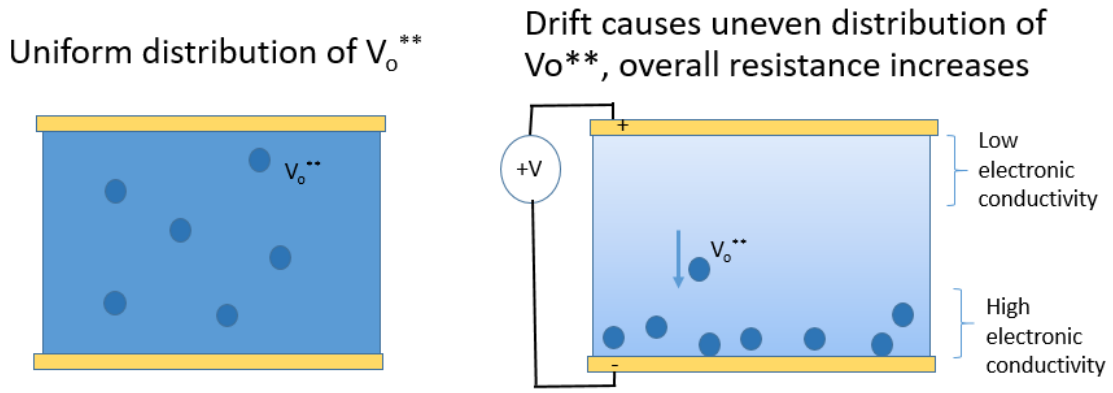

Figure 3-3: Schematic of the mechanism for negative resistance under voltage sweep in DIVA.[7]

negative voltage sweeps at the same sweep rate). The peak shifts for different voltage sweep rates, as the ionic defects have more or less time to rearrange in each case. The mobility can be calculated by measuring the time to peak current for several sweep rates, according to the following equation:

$$\nu^{-1} = C\mu_i l^{-2} t_{peak}^2 \tag{3.3}$$

where ν is the voltage sweep rate, C is a constant equal to 2, μ_i is the ionic mobility, l is the device length, and t_{peak} is the time elapsed between the start of the experiment and when the peak current is reached. The advantage of DIVA over other electrochemical techniques is that it allows for the direct measurement of the mobility of an ionic species – i.e. the ionic species's transport under the influence of an electric field (drift), as opposed to measuring diffusivity or diffusive transport.[7]

DIVA was considered for measurement of proton transport in the Pt/GdO_x/Au devices. However, the criterion of ion-blocking electrodes and a constant number of ionic defects is likely not met in these devices. Under vacuum, no additional protons are added from water splitting at the top electrode. Without this electrode reaction, the cathodic reaction (reduction of H^+ at the back electrode) should also not occur. However, in a device made from a large area oxide film, protons can diffuse laterally out of the device area, meaning the concentration of protons cannot be assumed to be

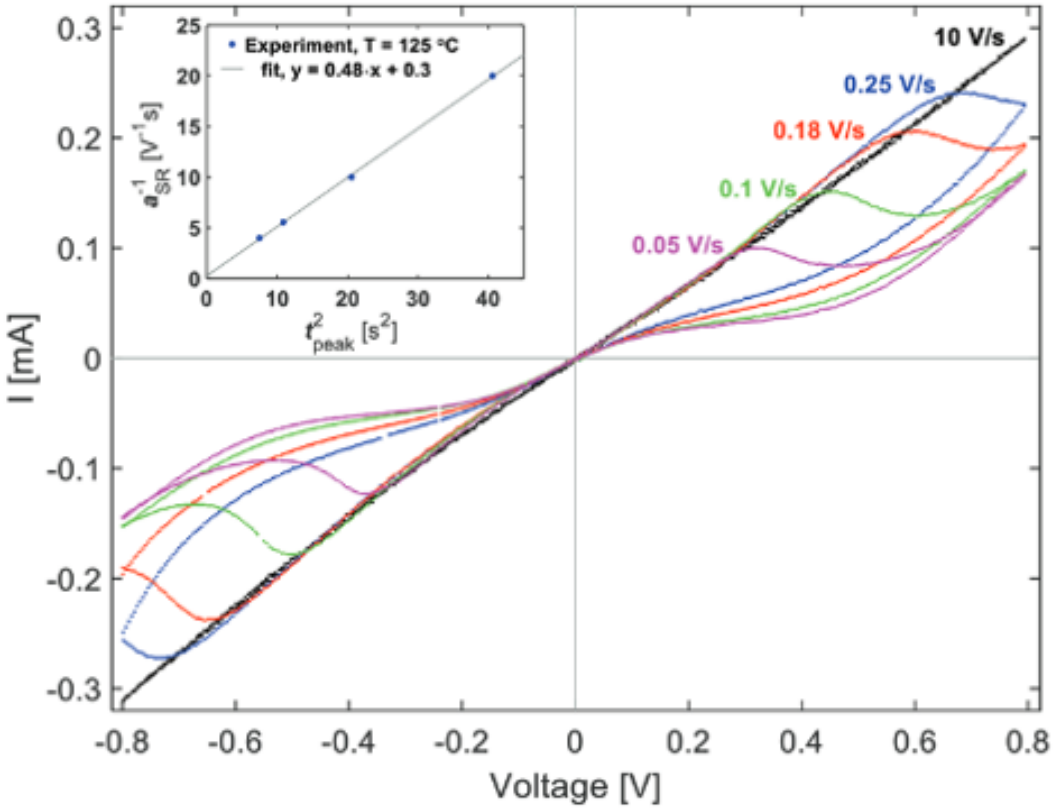

Figure 3-4: Example of DIVA data on praseodymium-doped ceria (PCO) devices (with an Au/PCO/Au crossbar structure), showing peaks for voltage sweeps at different rates. Reprinted from Kalaev et al. [8].

constant. Additionally, the reverse reaction (discharge of the cell) can still take place under negative bias, producing hydrogen gas rather than water vapor. In devices with thick Au electrodes that prevent the H_2 gas from escaping into the atmosphere, bubbles form when the device is under negative bias, indicating that protons are still leaving the oxide and being reduced to form H_2 gas. Since the redox reaction is still occurring, the electrode cannot be considered to be ion-blocking, and the concentration of protons in the system is not constant. This means that even in a device with patterned oxide (such that the oxide is present only under the electrode and there can be no lateral diffusion of protons), DIVA would not work under negative bias. In a patterned device, the positive sweep of a DIVA curve may yield a correct analysis of the proton mobility. This of course assumes that the concentration of protons in the oxide significantly affects the oxide's electronic conductivity, leading to a change in electronic current when the protons are driven to one side of the device.

3.3.3 Relative humidity control and measurement

Relative humidity in the sample chamber was controlled by bubbling nitrogen gas through a Fisher Scientific bubbler with water at room temperature, unless otherwise specified. The flow rate of nitrogen controlled the %RH in the chamber.

Relative humidity (%RH) was measured using an EXTECH RH30 sensor, a Sensirion SHT31, or a Sensirion SHT40 "SmartGadget" sensor, which I recommend due to its small size and Bluetooth capability (making it suitable for humidity readouts from sealed environmental chambers). Humidity sensors were calibrated by sealing them in a chamber with a saturated NaCl solution at room temperature and allowing the humidity to settle at its equilibrium value of 75 %RH. The humidity sensors used all also measure temperature, making it easy to ensure that the sample temperature was constant for different nitrogen flow rates.

3.4 Magnetic characterization

3.4.1 Magneto-optic Kerr effect

The magneto-optic Kerr effect (MOKE) is one of the easiest ways to obtain information about the magnetization of a sample. It measures the rotation of light as it reflects off of a surface with a net magnetization. The basic setup for a MOKE system is a laser, a polarizing film, optical parts that direct the laser light to bounce off of the sample surface, an analyzing polarizer (or analyzer) rotated so that it is near extinction compared to the polarizer, and a detector (see Figure **??** for a schematic). At the most basic level, the magnetic moment from the sample rotates the polarization of the laser light. With crossed polarizers, one would expect no light to get through to the detector. The rotation introduced by the sample allows some light to get to the detector, and its amplitude is proportional to the magnetization of the sample. A MOKE system can be built with a relatively small set of optical parts and is a quick and easy way to measure a sample's hysteresis loop.

In this work, magnetic characterization is done using a polar MOKE configuration, which measures out-of-plane magnetic hysteresis loops. We use a red laser source with wavelength of 655nm is used. The laser spot is focused to 10-200 μm. A CCD camera along the vertical axis allows us to image the sample. An out-of-plane electromagnetic coil capable of producing 1000 Oe of out-of-plane field is located under the sample stage. The magnetic field is swept to the desired value and the reflected intensity is measured using a photodetector in order to produce a hysteresis loop. The amplitude of the hysteresis loop is proportional to the out-of-plane magnetization of the sample, while the x-intercepts give the coercivity (H_c) of the sample. Note that the intensity does not give a quantitative measurement of the saturation magnetization, M_S, but allows us to track its relative value over time, which is relevant for voltage gating experiments during which we are interested in the relative magnetization of the sample under different environmental conditions or amounts of hydrogen present in the magnetic layer.

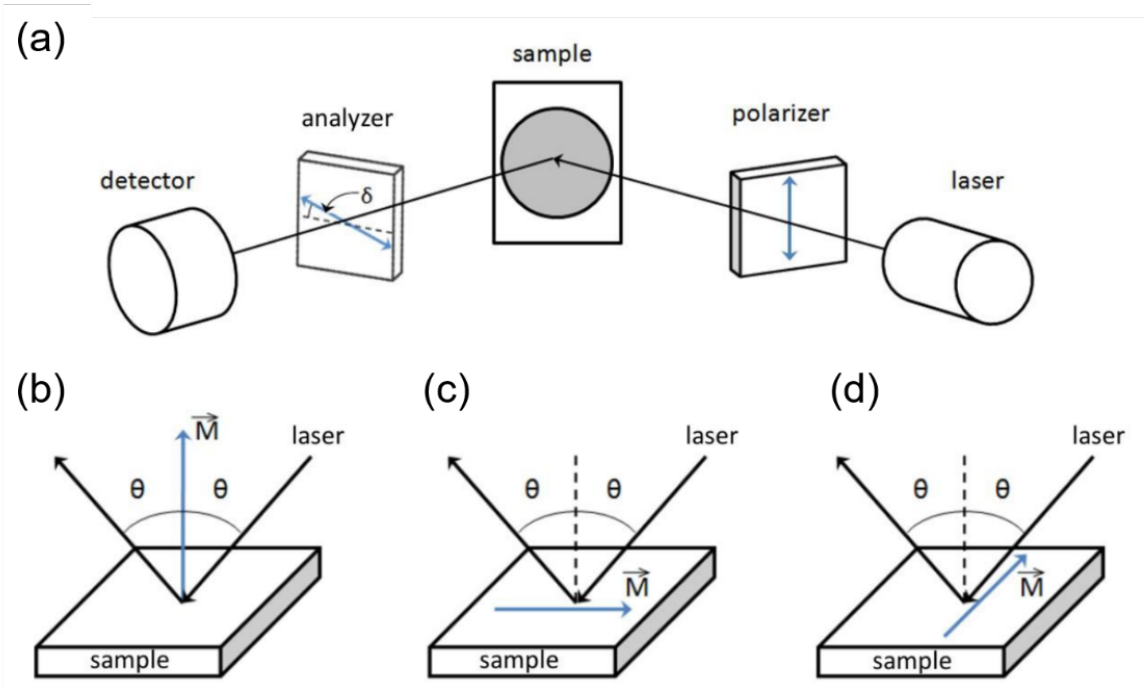

Figure 3-5: a) Schematic of a MOKE setup. The magnetic field (not shown) would be applied perpendicular to or in the plane of the sample. The blue arrows indicate the polarization axis of the polarizer and analyzer. b)-d) Illustrations of polar, longitudinal, and transverse MOKE measurements, respectively. The blue arrows indicate the net magnetization of the sample film. Reprinted from Ref. [9].

Chapter 4

Characterization of GdO_xH_y under hydration and gating

Previous work has characterized the GdO_xH_y, including XRR[10], cross-sectional SEM showing a dense non-porous oxide[4] and cross-sectional TEM[73] showing that the GdO_xH_y is polycrystalline with 5-10 nm grain size.

Investigating the role of hydration in GdO_xH_y, previous works used x-ray reflectivity (XRR) and x-ray absorption spectroscopy to show that during hydration of a GdO_x film in a humid environment, a layer of $Gd(OH)_3$ grows from the surface, and that without this hydration step, the device does not function.[10] Other works have used a combination of x-ray and neutron reflectivity experiments to show similar protonated surface layers in proton-conducting oxide films (e.g. In-doped $BaZrO_3$[74]).

X-ray probes are relatively insensitive to hydrogen and instead probe changes in electron density, primarily controlled by the density of Gd. Unlike other elements in the system of interest, hydrogen has a negative neutron scattering length, so significant protonation sharply suppresses the neutron scattering length density (SLD), making the degree of protonation measureable with neutron techniques. Polarized neutron reflectometry (PNR) is also sensitive to the in-plane net magnetization depth profile of the thin film. PNR is therefore an ideal way to examine the movement of hydrogen and changes in magnetism in protonic devices.

In section 4.1, we first investigate the hydrogen depth profile in GdO_xH_y films

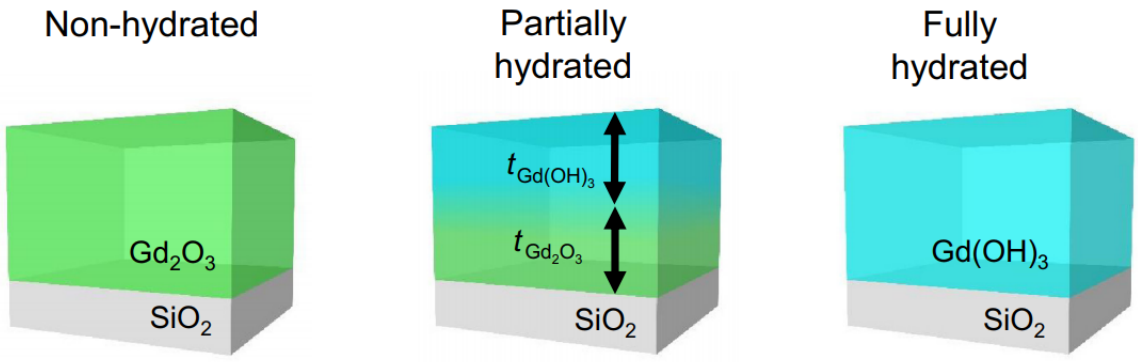

Figure 4-1: Schematic of the phase transformation from Gd_2O_3 to $Gd(OH)_3$, from Ref. [10].

during hydration and heating (dehydration) using XRR and unpolarized neutron reflectometry (NR). In section 4.2 we use PNR to probe the hydrogen depth profile and the magnetism in the Pt/Co/GdO_x/Au stack during *in operando* positive biasing. We verified the results with ex-situ secondary ion mass spectrometry (SIMS) after positive and negative gating.

This chapter is adapted from "Insight on hydrogen injection and GdOx/Co interface chemistry from in operando neutron reflectometry and secondary ion mass spectrometry" (Reference [75]).

4.1 Passive hydration

4.1.1 X-ray reflectometry comparison of reactive and RF GdO_xH_y

Previously, it was discovered that reactively sputtered GdO_x undergoes a phase transformation to $Gd(OH)_3$ after being exposed to a high humidity environment (see Figure 4-1). Figure 4-2 shows the x-ray scattering length density (SLD) profiles taken throughout the 6-day hydration of a 22.8 nm film, showing the growth of a lower-density $Gd(OH)_3$ layer that starts on the surface of the film and eventually encompasses the entire film. This transformation leads to a film expansion of 50%, as $Gd(OH)_3$ is less dense than Gd_2O_3.[10]

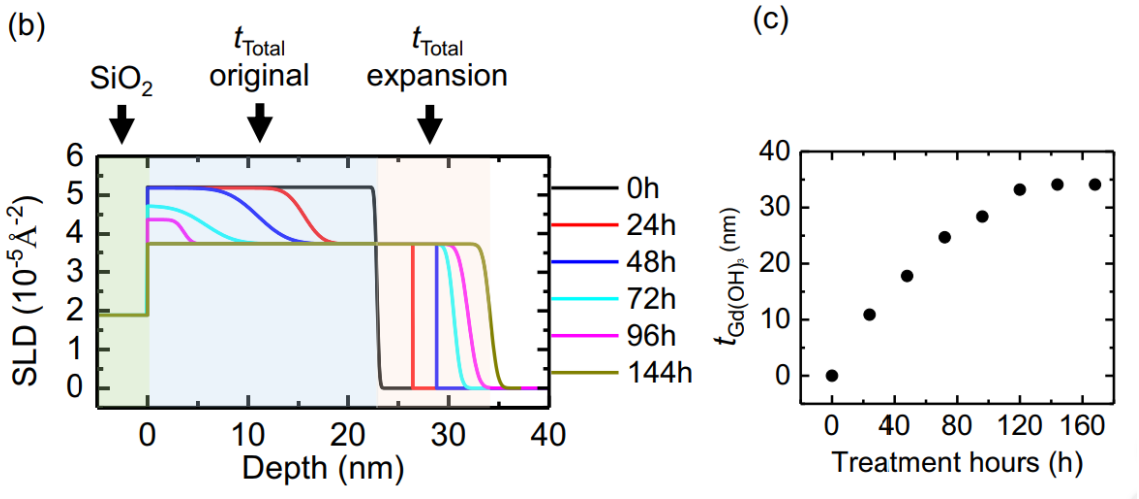

Figure 4-2: X-ray SLD profiles showing expansion over the course of 6 days, from Ref. [10].

Further study with XRR demonstrates that the hydration of GdO_x can be reversed with heating. Furthermore, we show that different methods of sputtering GdO_x can produce different phases, which hydrate in different ways. Figure 4-4 shows the relative thicknesses of Gd_2O_3 and $Gd(OH)_3$ in a reactively sputtered film in the as-grown state, after hydration, and after heating to 300°C and back down to 25°C. Figure 4-5 shows the changes in an RF sputtered film from the as-grown state, hydrated state, and after heating to 300°C. In each case, the XRR spectra were fit with a bilayer, with the bottom layer corresponding to the higher density (higher-SLD) Gd_2O_3 phase and the top layer corresponding to the lower density (lower-SLD) $Gd(OH)_3$ phase. The relative thicknesses of the two layers were allowed to vary. Gd_2O_3 The reactive film undergoes a large expansion with hydration as the Gd_2O_3 (green) absorbs H_2O and transforms to $Gd(OH)_3$ (blue). As the film is heated, the $Gd(OH)_3$ layer persists until 240 °C, at which point it begins to shrink as the water is driven out and the phase transformation is reversed. The film does not shrink back to its original thickness, which we attribute to the irreversible uptake of oxygen during the hydration. As the film cools from 300°C to 25°C in relatively low humidity conditions, it does not uptake a significant amount of water – to become rehydrated, it would need to be exposed to high humidity conditions again.

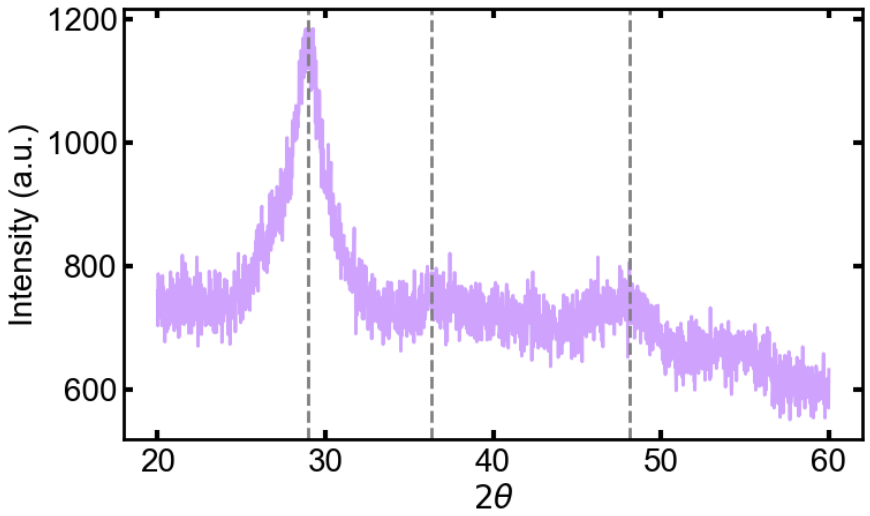

Figure 4-3: XRD of 100 nm unhydrated RF sputtered GdO_x film showing peaks at 2θ values of 28.9, 36.3, and 48.2, indicated by the dotted lines.

The RF film, surprisingly, is best fit in the as-grown state with a lower-density GdO_x film, indicating that it is $Gd(OH)_3$ in the as-grown state. This is confirmed with XRD (Figure 4-3). The broad peaks around 30°and 50°match with the XRD spectrum of amorphous or nanocrystalline $Gd(OH)_3$, without any strong Gd_2O_3 peaks.[76] The RF film starting out as a hydroxide without a specific hydration step could be due to a microstructure that allows for quick uptake of water in ambient conditions, or it could be that the "Gd_2O_3" target used for sputtering is actually partially or completely $Gd(OH)_3$ or hydrated Gd_2O_3 (Gd_2O_3 with interstitial protonic defects). This is likely given that the target has been kept under ambient conditions for several years. The RF film undergoes very slight expansion with hydration, and slight contraction with heating to 300 °C. It may be that the heating experiment was not carried out on a timescale long enough to see significant water loss and conversion of the film back to Gd_2O_3.

4.1.2 Neutron reflectometry

We investigated the hydration of an unpatterned, large area GdO_x film with NR. A 1 cm^2 GdO_x film was grown on a Si substrate with a thermally grown oxide layer. The

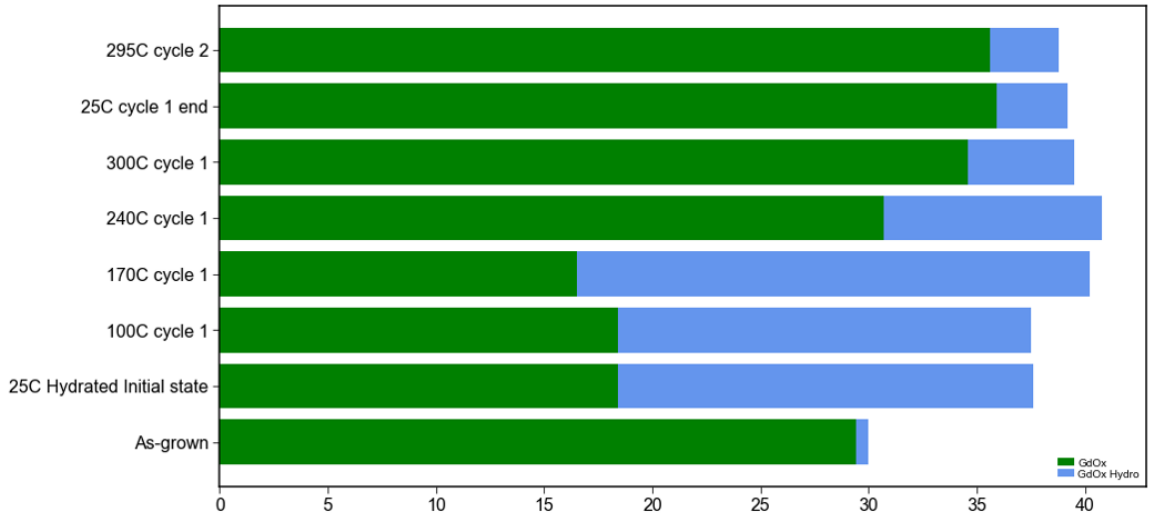

Figure 4-4: Relative thicknesses of high density Gd_2O_3 and low density $Gd(OH)_3$ layers in a reactively sputtered GdO_x film, showing the relative growth of the hydrated layer during hydration and subsequent annealing at high temperature. Thicknesses calculated from the best bilayer fit to the XRR spectrum for each condition. The film was hydrated at 70°C and 95%RH for 6 days after the as-grown state was measured.

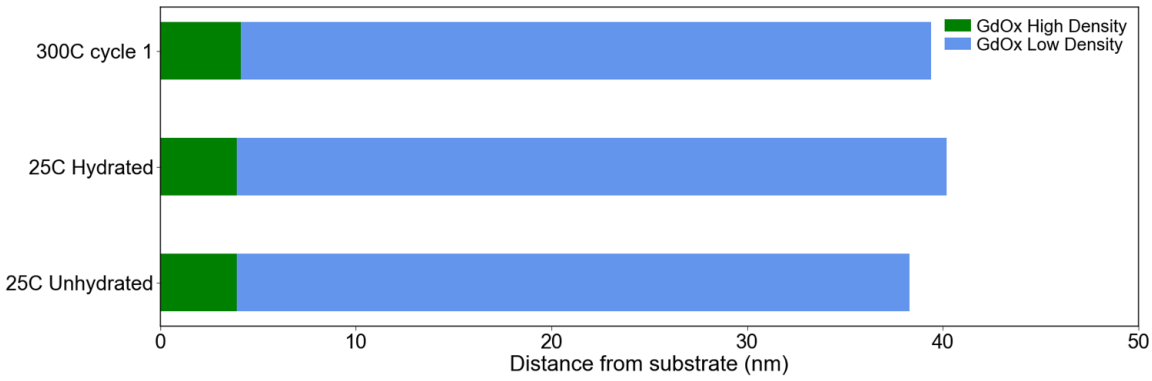

Figure 4-5: Relative thicknesses of high density Gd_2O_3 and low density $Gd(OH)_3$ layers in an RF sputtered GdO_x film. Thicknesses calculated from the best bilayer fit to the XRR spectrum for each condition. The film was hydrated at 70°C and 95%RH for 6 days after the as-grown ("unhydrated") state was measured.

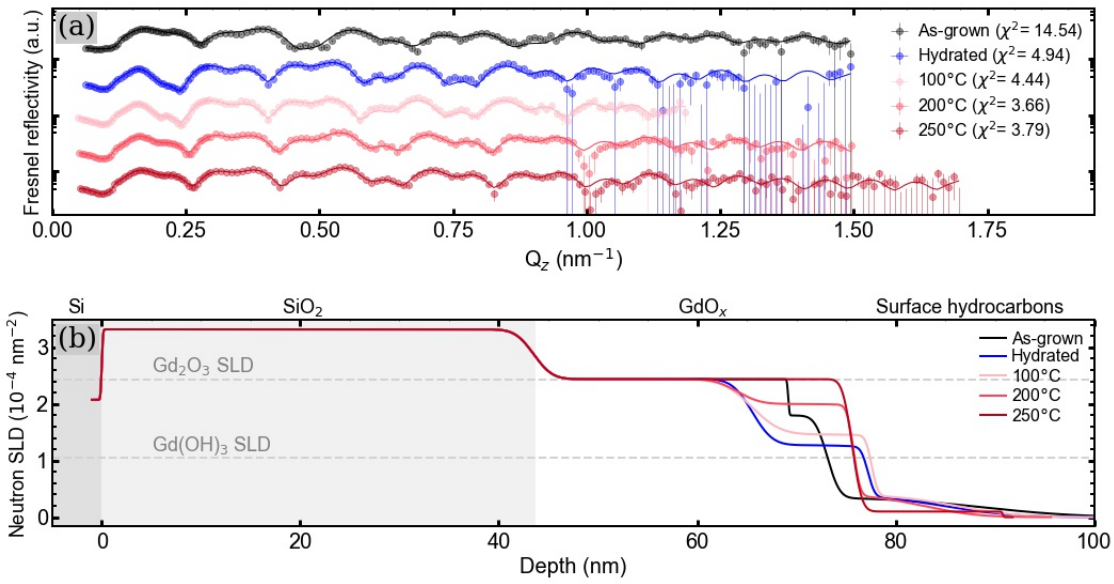

Figure 4-6: NR on unpatterned film showing passive hydration under humid conditions and dehydration upon vacuum annealing. a) Fresnel reflectivities for as-grown, hydrated for 20 hours, and vacuum annealed at 100 °C, 200 °C, and 250 °C. b) Best fit neutron SLD profiles for the same conditions.

film was held at 50 °C and 90%RH for 20 hours and was then vacuum annealed at 100 °C, 200 °C, and 250 °C, all while NR scans were performed continuously. The sample was held under each condition until no drift occurred between scans (approximately 2 hours). Fig. 4-6 shows the neutron reflectivities and associated SLD profiles for the film in each condition. Note that error bars and uncertainties in this chapter represent one standard error.

The as-grown GdO_x film thickness is 29.58 ± 0.14 nm, including a 3.94 ± 0.07 nm layer with reduced SLD at the surface, indicating some combination of oxygen deficiency and partial hydration from exposure to ambient humidity. Such surface regions have been seen in proton conducting perovskites.[74] After hydration, the neutron SLD near the air interface decreases further and the thickness of the low-SLD region increases. The hydrated GdOx lyer is best fit by a bilayer oxide/hydroxide structure with a hydroxide layer thickness of 11.64 ± 0.09 nm, for a total GdOx thickness of 33.67 ± 0.18 nm. For comparison to a linear gradient fit, see Section 4.4 and Figure 4-7. The quality of the bilayer fit rules out a gradient in hydrogen concentration,

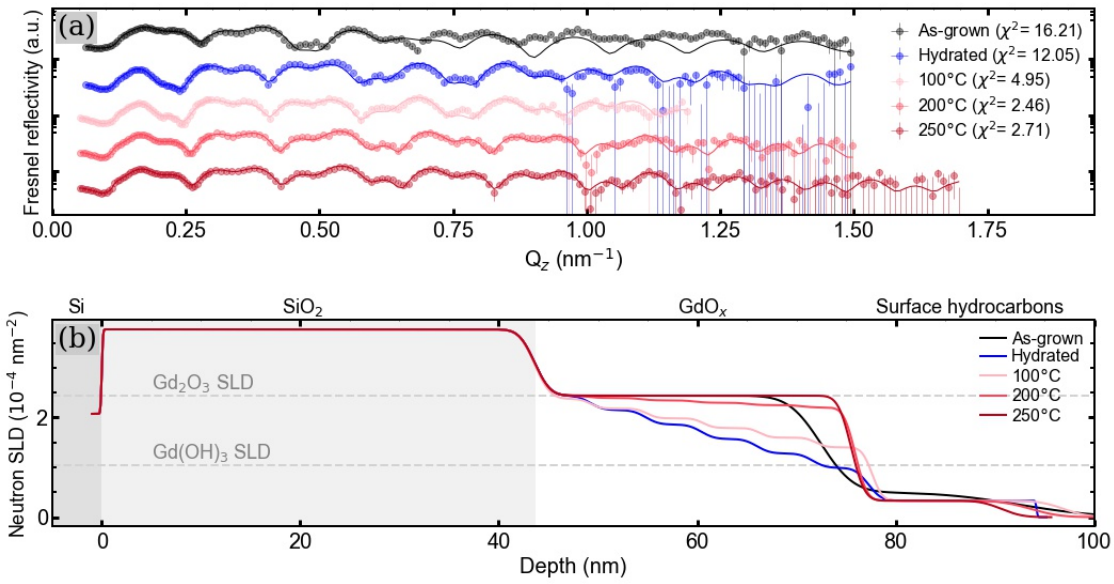

Figure 4-7: Alternate linear gradient fit for NR on unpatterned film during hydration and vacuum annealing. (a) Fresnel reflectivities for as-grown, hydrated 20 hours, and vacuum annealed at 100 °C, 200 °C, and 250 °C states, with fit line for best gradient fit. (b) Neutron SLD profiles for the gradient fit.

as any nonuniformity should make the fit significantly worse. This bilayer structure confirms that hydration occurs through a phase transition to $Gd(OH)_3$ with a front that extends deeper into the film with longer hydration time (see Figure 4-8 for NR reflectivities showing the hydroxide expansion over time). During 20-hour hydration, the total oxide thickness increases by 13.8% compared to the as-grown state. This is consistent with previously reported 15% thickness increase measured for 24-hour hydration of a similar film with XRR.[10]

Here we note that several factors simultaneously affect the hydroxide SLD. As the phase transition to $Gd(OH)_3$ occurs, the overall material density decreases from 7.41 g/cm^3 (bulk Gd_2O_3) to 6.0 g/cm^3 (previously measured density of $Gd(OH)_3$).[10] Hydrogen incorporation causes the phase transformation and the expansion of the lattice, so these processes are inherently connected. However, it is useful to consider their relative effects on the SLD. From the decreased number density of Gd and O atoms in the hydroxide phase alone, we expect an SLD decrease of 19%, to a value of 1.98×10^{-4} nm^{-2}. Hydrogen incorporation suppresses the SLD further; SLD values

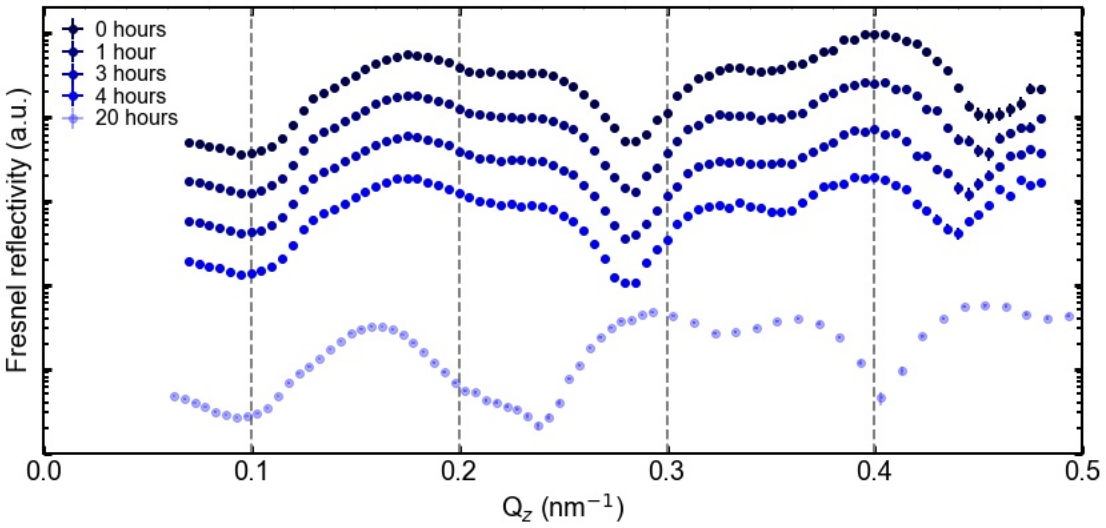

Figure 4-8: Unpolarized neutron reflectivities for short scans taken during the first several hours of hydration of the unpatterned GdO_x film. Hydration was done at 50 °C and 90% RH. The shifting of the features to lower Q_z is a result of the gradual growth of the thickness of the low-SLD hydroxide layer at the surface of the film. The state at 20 hours of hydration (also plotted as the "Hydrated" state in Fig. 4-6a) is plotted for comparison.

significantly below 1.98×10^{-4} nm^{-2} in the hydrated sample therefore argue strongly for increased H concentration. The final hydroxide layer SLD is slightly higher than the expected value of 1.05×10^{-4} nm^{-2} (see the gray dotted line in Fig. 4-6a), meaning the Gd and O density is higher than expected (perhaps due to some remaining Gd_2O_3) or the H concentration is lower than expected for stoichiometric $Gd(OH)_3$.

When vacuum annealed at 100 °C, the hydroxide layer SLD increases as hydrogen is driven out. The film thickness decreases above 200 °C, with further reduction in hydrogen concentration in the hydrated layer. At 250 °C, the GdO_x SLD has returned to the as-grown value. Interestingly, the film thickness does not shrink back to its original value. The 250 °C state does not have a low-SLD surface layer, meaning that between the as-grown and 250 °C states, the H in the surface layer of the as-grown film has been driven out and the oxygen content of that surface layer has increased to match the rest of the film. Oxygen could be incorporated into the film during the phase transition to a hydroxide (according to Equation 2.1) and then may not be

removed during vacuum annealing. This is consistent with the previously mentioned XRR results – although we did not comment on this previously, after 6 days of hydration, the film expanded by 50% and decreased its SLD by 28%, giving a 10% increase in total integrated x-ray SLD between the as-grown and the fully hydrated states.[10] This increase is consistent with additional oxidation of the film.

The low SLD tail in each profile above Z = 79 nm is probably due to adsorbed hydrocarbons, which desorb above 200 °C. The 250 °C SLD profile thus shows a sharp interface instead of a tail.

4.2 Characterization of gated device

4.2.1 Structural characterization

We now turn to the Pt/Co/GdO_x/Au patterned devices and examine how hydration and voltage gating affect their structure, hydrogen profile, and magnetism. The Pt/Co/GdO_x/Au devices are susceptible to pinholes at device areas above 5 mm^2, so in order to have a device area large enough for PNR, we used an array of thirty 1 mm^2 square crossbar devices (see sample schematic in Figure 4-9). We measured the PNR in the as-grown state, after hydration, and during *in operando* biasing at +3V and +10V. The bias voltages were held constant and PNR scans were done continuously until the reflectivities stabilized for the duration of one scan (around 12 hours). Fig. 4-10 shows the PNR reflectivities and the SLD profiles for all conditions.

After scanning the as-grown state, the sample was hydrated for 6 days at 90 °C, since previous XRR data found that the thickness change was complete within that time.[10] A saturated K_2SO_4 solution maintained the relative humidity in the sample chamber at 95%. Comparing the as-grown and hydrated SLD profiles in Fig. 4-10b, we see that the GdO_x layer becomes approximately 25% thicker with hydration. This change is not as dramatic as was seen in the XRR measurement, which could be explained by the Au electrode capping our film. Figure 4-11 shows XRR data for a two sibling GdO_x films (films grown simultaneously with a rotating planetary sample

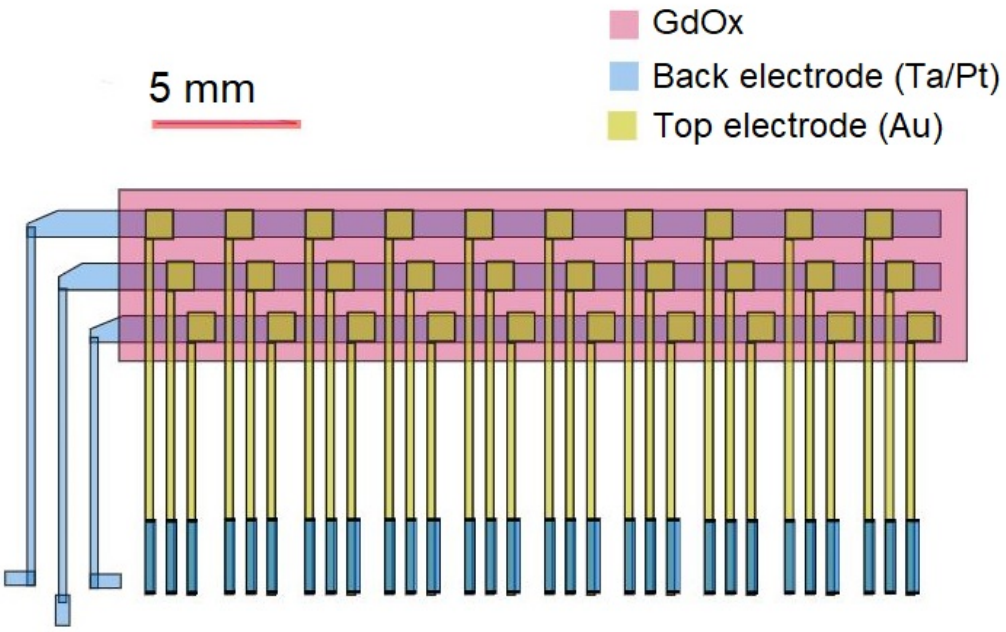

Figure 4-9: Schematic of the patterned sample, where the blue region is the Ta/Pt back electrode, the pink region is the oxide, and the yellow region is the Au top electrode. The Co (plus a 4 nm GdOx capping layer to protect the Co from oxidation during sample growth) was deposited on the back electrode only in the pink region, so as to leave a region of Ta/Pt open to the air to make electrical contact to the back electrode.

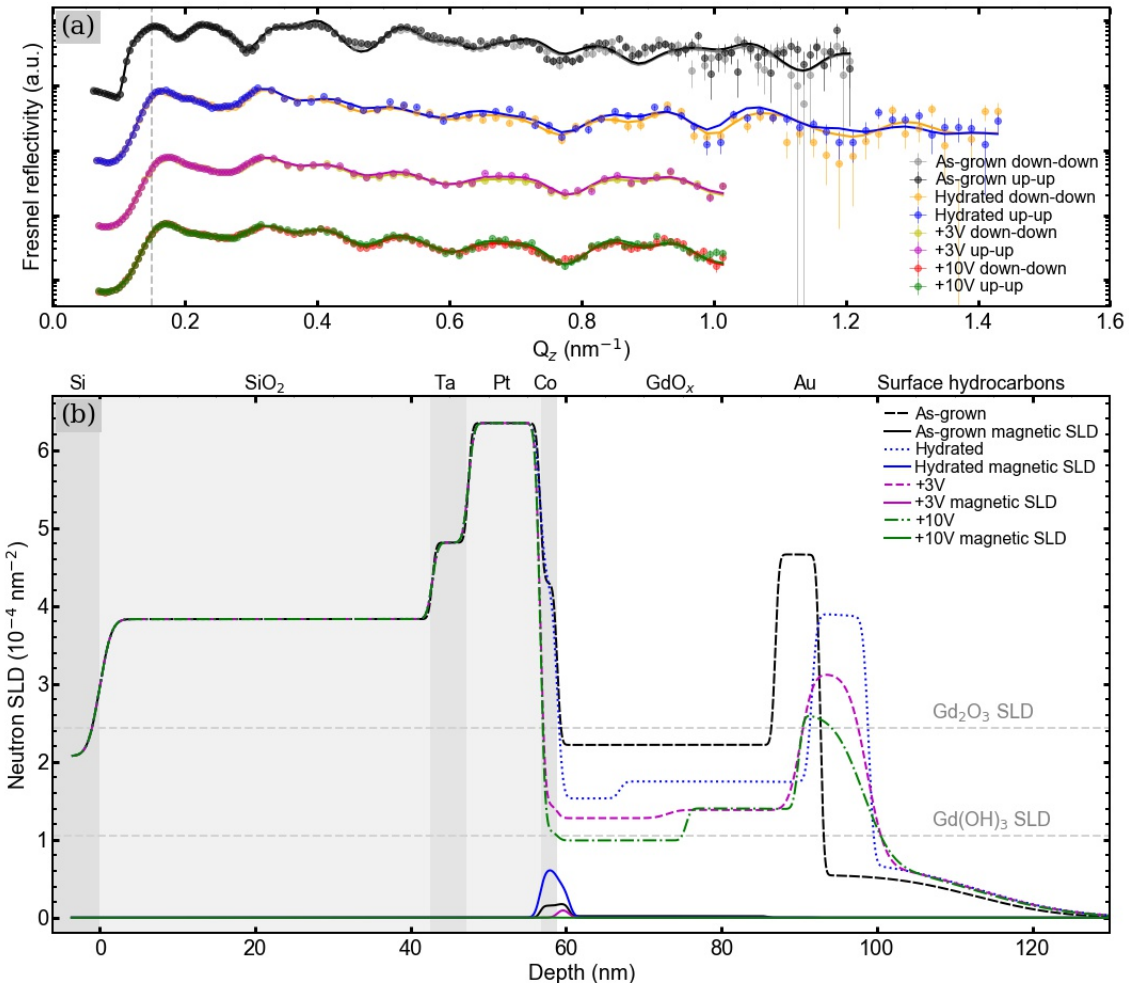

Figure 4-10: PNR data for the patterned device in as-grown, hydrated, +3V gated, and +10V gated states. a) Non-spin-flip (↑↑ and ↓↓) Fresnel reflectivities for all four conditions. b) Best fit SLD profiles from the reflectivity data in a). Both real nuclear and magnetic SLDs are plotted. See "PNR data reduction and fitting" section for fitting details.

holder ensuring that both films are exposed to the sputter plume for the same time and are therefore as identical as possible). The films were sputtered reactively. An Au capping layer was grown on one film in situ directly after the GdO_x was deposited, without a vacuum break. Both films were then hydrated under the same conditions. XRR data shows that the uncapped film expanded and decreased in density, indicating that it was transformed to $Gd(OH)_3$ as expected. The Au-capped film thickness and density did not change, indicating that the water vapor from the air could not pass the Au barrier. This is relevant for our devices, since it shows that they must be hydrated before the top electrode is deposited, or they need to be allowed sufficient time for lateral diffusion to hydrate the area underneath the electrode. The amount of time required will depend on the electrode area. In the case of the PNR sample, this factor explains why the hydration of the patterned devices with Au top electrodes caused expansion of only 25% in 6 days rather than the 50% expansion experienced by the unpatterned, uncapped oxide films discussed in Section 4.1. If the Au prevented hydrogen incorporation, then hydration must have occurred through lateral diffusion and may have been slower or incomplete. This could also explain the lack of hydrated layer at the top of the GdO_x film, unlike what was observed after hydration of the unpatterned film. Lateral diffusion may play a larger role at the Co/GdO_x interface, which could explain the decreased GdO_x SLD next to the Co layer in the hydrated state. Alternatively, increased defect concentration near the bottom interface may cause preferential H occupation. The GdO_x SLD starts near the expected bulk value for Gd_2O_3, 2.44×10^{-4} nm^{-2}, and approaches the expected $Gd(OH)_3$ SLD value of 1.05×10^{-4} nm^{-2} after hydration and gating. The low GdO_x SLD near the Co layer after gating is likely due to the low hydrogen solubility in Pt, which makes hydrogen accumulate near the Co interface as it is pumped in. It could also be due to the formation of a hydroxide layer at the bottom of the GdO_x layer which gets thicker as more H is pumped in. In either case, it is clear that H is being driven to the Co/GdO_x interface.

The transformation from oxide to hydroxide is corroborated with SIMS, which shows increased signal from GdO_xH_y ions after gating compared to the as-grown

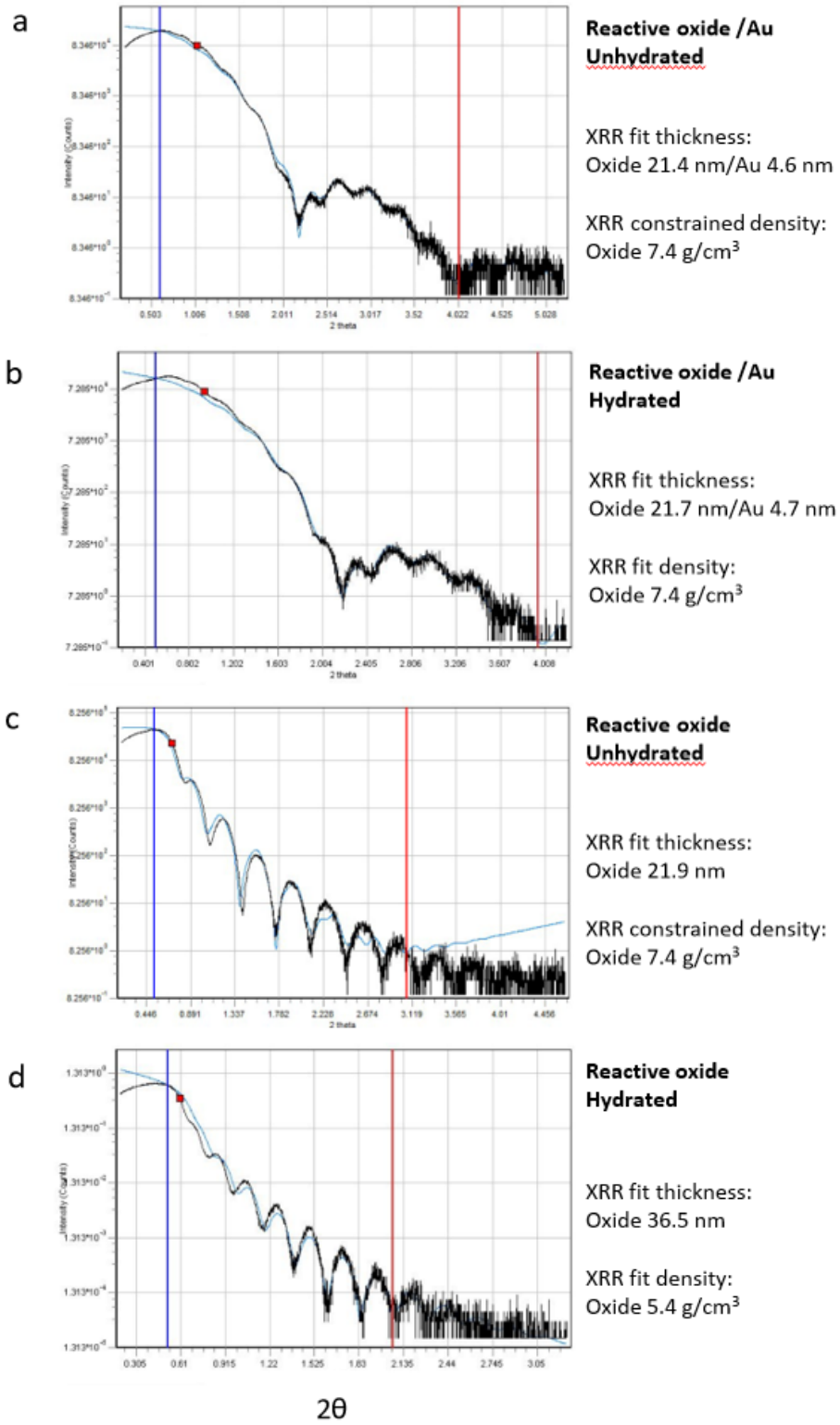

Figure 4-11: XRR spectra (black data), fit spectra (blue lines), fit thicknesses, and fit densities for reactively sputtered GdO_xH_y large area unpatterned films. a) Unhydrated film with 5 nm Au capping layer. b) The film from a) after 6 days hydration at 95 %RH. c) Unhydrated film without a capping layer. d) The film from c) after 6 days hydration at 95 %RH. The blue and red vertical lines indicate the region of the data that was fit.

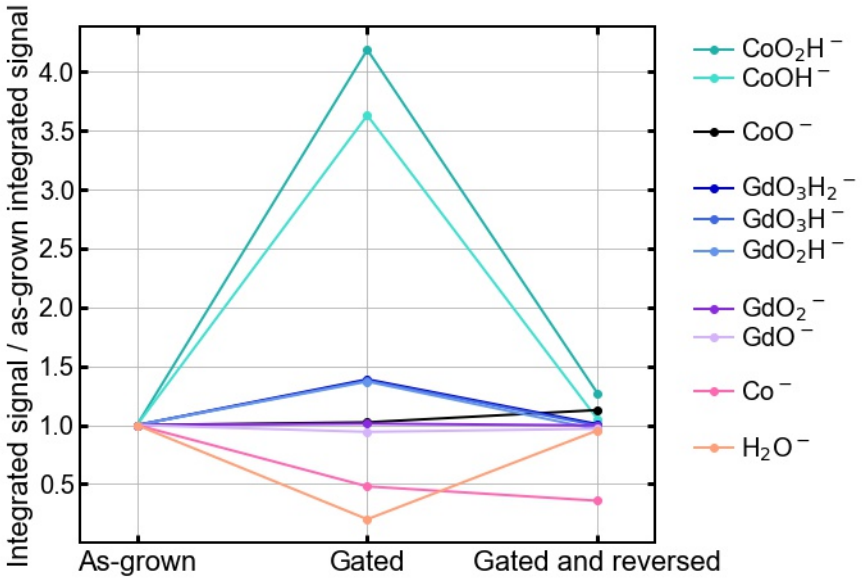

Figure 4-12: Integrated SIMS signal for CoO_xH_y, GdO_xH_y, Co, and H_2O ions, measured on three different unhydrated 1 mm^2 crossbar devices gated into different states. See the Methods section for further information about SIMS measurements.

state (Fig. 4-12). The SIMS devices were unhydrated, with any initial hydrogen in the GdO_x coming from exposure to ambient conditions. The presence of GdO_xH_y only after gating therefore confirms that significant additional hydrogen enters the oxide during positive biasing. The SIMS signal for H_2O decreases with positive bias, likely since the H_2O on the surface (and also possibly in the oxide at grain boundaries) is split and incorporated into the hydroxide.

The Au exhibits slight thickness increase and significant SLD decrease upon hydration, which is consistent with water and hydroxide accumulation on the surface. The Au layer roughens significantly and decreases further in thickness upon gating (corroborated with atomic force microscopy in Figure 4-13, which is consistent with Au oxidation[77, 78] or surface adsorbates. An alternative interpretation is that the GdO_xH_y expands nonuniformly, causing a roughened interface that spreads Au out in Z, giving an apparently thicker, lower SLD film. The increase in diffuse scattering from the Au electrode after gating can be seen by eye, consistent with the significant increase in roughness in the fit. We note that a significant amount of water or hydro-

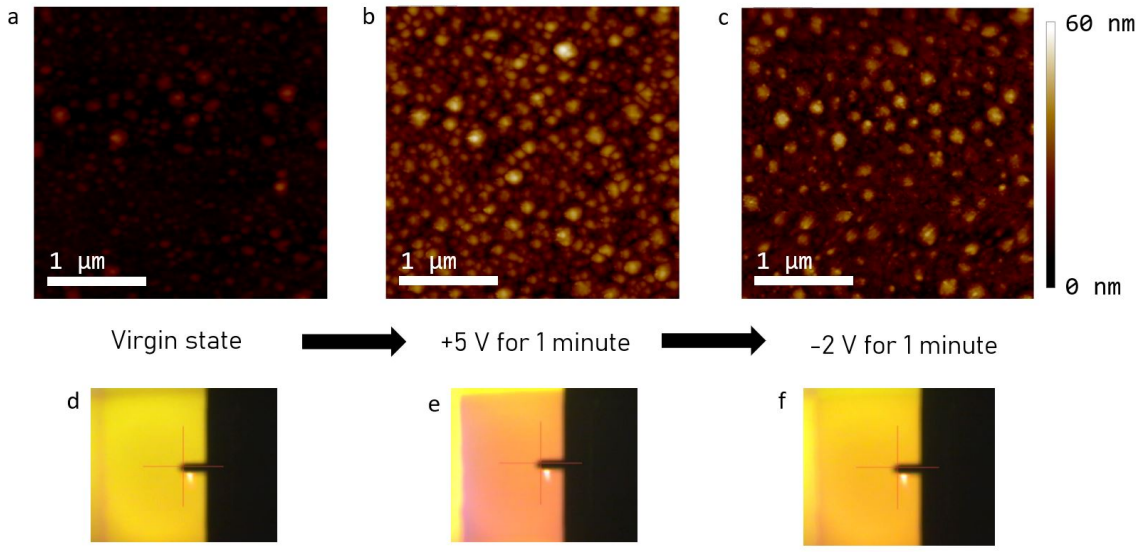

Figure 4-13: Atomic force microscopy (AFM) on a device (a) in virgin state, (b) after +5 V gating for 1 min (device held at +5 V for the duration of the AFM scan, a total of 9 min), and (c) after -2 V gating for 1 min (device held at -2 V for the duration of the 9 min scan). These scans show the partially reversible roughening of the device during gating. (d-f) Optical images of the device in the same three states, showing the visible changes in color and diffuse scattering.

gen adhering to this layer may add apparent roughness unrelated to a change in the structure of the underlying gold. Thus, there is considerable uncertainty regarding the gated Au roughness values presented here.

In the as-grown and hydrated fits, the Co layer SLD is 4.29×10^{-4} nm^{-2}, closely matching that of bulk CoO. Partial or complete Co oxidation is unsurprising, as it was exposed to oxygen during reactive sputtering of GdO_x. Upon gating, the Co layer SLD decreases to 1.4×10^{-4} nm^{-2}. While we expect both reduction of the CoO to Co and incorporation of hydrogen to decrease the Co layer SLD, the optimized value is significantly below the bulk Co value of 2.27×10^{-4} nm^{-2}, which is consistent with a significant degree of hydrogenation. For additional context, we calculate that the bulk nuclear SLD of cobalt hydroxide ($Co(OH)_2$) is 1.54×10^{-4} nm^{-2} while the optimized values for the +3 V and +10 V gated conditions are 1.44×10^{-4} nm^{-2} and 1.11×10^{-4} nm^{-2}, respectively. Co reduction under positive bias was previously reported in this system, and H incorporation is what depressed the SLD of the surrounding GdO_x, so it is likely that both processes occurred in the Co layer to reduce its SLD.

Increased porosity in the Co upon reduction from CoO could also explain the lowered SLD. However, the SIMS data in Fig. 4-12 show a small Co^- signal that decreases upon gating by 61%, while the $CoOH^-$ and $CoOH_2^-$ signals increase by 217% and 328% respectively. Further, while SIMS confirms the presence of CoO compounds in the device, the gating does not result in a significant change to the integrated CoO intensity. Instead, the largest variations in SIMS intensity are confined to hydrogen-containing species, supporting hydration as the major cause of SLD reduction over increased porosity. It is not possible to explicitly distinguish the contributions of these possible mechanisms to the SLD reduction of the Co layer, but likely, both play a role, with the H incorporation dominating. Note that we looked extensively in the SIMS data for any evidence of cobalt hydrides (CoH_x) and found none. CoH_x compounds typically form only at extremely high pressure, so while we see evidence of H in the Co layer, a CoH_x phase is unlikely.[79]

4.2.2 Magnetic characterization

We found several unexpected results in the magnetic portion of the PNR and in the SIMS data, which lead us to a more complex model of the chemistry of the Co magnetic layer and surrounding interfaces. Our first unexpected finding is that in all states, as-grown, hydrated, and gated, the Co layer had much smaller magnetic SLD than expected – only 15% the bulk Co value of 1400 emu/cm^3 (1 emu/cm^3 = 1 kA/m), which corresponds to an expected magnetic SLD of 4.12×10^{-4} nm^{-2}. An in-plane field of 700 mT was applied during measurement to pull the Co magnetization in-plane, so any magnetization should be visible in the magnetic SLD profile (Fig. 4-10b). One way to explain this is to assume that only a few devices contained unoxidized ferromagnetic Co. However, constraining the fit to have a very small "active device" area with metallic ferromagnetic Co worsens the fit significantly, so we do not believe this is a likely explanation. Enough Co was present in all as-grown devices to measure a polar MOKE signal displaying PMA (see Figure 4-14 for a representative MOKE loop). Thus, in the as-grown state, the diminished Co magnetization can be explained by a mixed phase of CoO and Co, in accordance with the structural analysis.

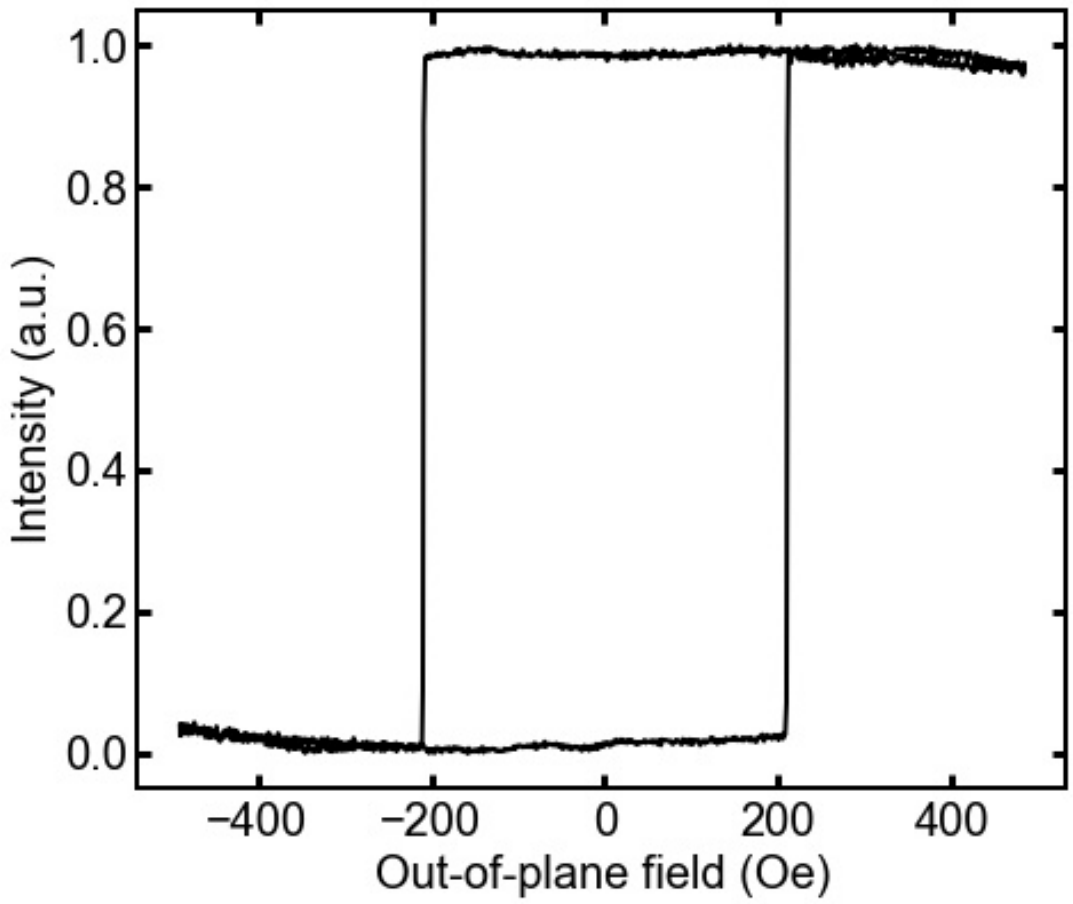

Figure 4-14: Polar MOKE loop for one device on the patterned sample, done before the as-grown PNR scan. This loop is representative of the initial state for the other devices on the sample.

The second unexpected result is that the Co magnetization grows after hydration and decreases during biasing. To understand why the magnetic SLD is fit this way, we examine the Fresnel spin difference, or the difference of the non-spin-flip reflectivities ($\uparrow\uparrow$ minus $\downarrow\downarrow$), normalized by the theoretical reflectivity of the bare Si substrate. Fig. 4-10a shows the spin-dependent neutron reflectivities for the four measurement conditions, and Fig. 4-16 shows the Fresnel difference of those reflectivities. Figures 4-16b-e show detailed views of the low-q regions. The amplitude of the oscillations in the Fresnel difference is proportional to the total magnetization in the film. The Fresnel difference oscillates in all conditions, and for the first four (lowest q) peaks, the amplitude of the oscillation in the positive biased state is smaller than the amplitude in the hydrated state, implying that the magnetization has decreased during positive biasing. Figure 4-15 gives the statistical analysis of these data. Our analysis indicates that the hydrated state must have a larger magnetic SLD than the as-grown and biased states. Based on previously reported MOKE measurements, we would expect CoO to be reduced to Co with the presence of H_2O under positive bias, which (absent any other chemical or structural changes) should increase the net magnetization. It is possible that some CoO is in fact reduced, changing the relative amounts of CoO and Co, but that other effects, discussed below, obscure the effect on the measured magnetization.

The third unexpected result is that the Fresnel spin difference below the critical edge ($Q_{crit} = 0.1$ nm^{-1}) is nonzero (shown clearly in Figure 4-15a), indicating that some magnetization is co-located with a neutron absorber (Gd) in the film. Co and GdO_x were thought to be distinct layers, while the GdO_x itself is not magnetic. The best description of this feature appears when a layer of GdO_x near the Co/GdO_x interface is allowed to express a net magnetization in the model. This interfacial magnetization is notably reduced upon gating. One explanation for magnetized Gd is an intermixed sub-layer of Co and GdO_x (or even Pt, Co, and GdO_x). Paramagnetic behavior in Co-doped nanocrystalline GdO_x at room temperature has been observed.[80] The intermixing could have occurred during sputtering, which is common especially for heavy elements.[81] The sample was also held at 90 °C for 6 days

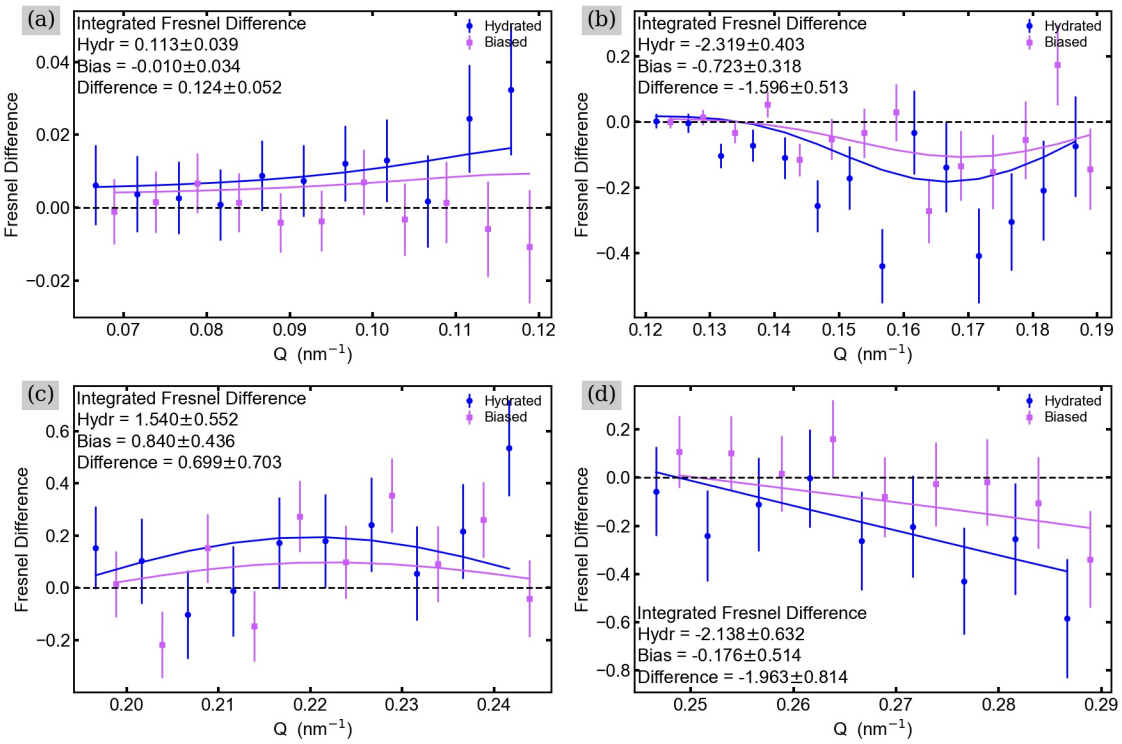

Figure 4-15: The first four peaks in the Fresnel spin differences for the hydrated and +3 V biased states. Subplots a-d show windows with increasing q ranges corresponding to the first four oscillations shown in Fig. 4-16c and d. The total integrated value of the Fresnel spin difference for each window is given. For each oscillation, the amplitude and total integrated value in the hydrated state is greater than that in the positive biased state.

during hydration, possibly allowing atoms around the magnetic layer to rearrange. Intermixing can explain the suppression of Co magnetization below the bulk value in the as-grown and hydrated states, especially if the Co and Gd develop antiparallel moments. It could similarly explain the increase in magnetization upon hydration and the suppression during gating. If indeed Co and Gd intermixing leads to magnetization suppression in the as-grown state, deconvoluting the chemistry controlling the net moment becomes nontrivial, with Co and Gd reacting with O and H in ways which may have offsetting effects.

The SIMS results lend credence to this picture. SIMS shows that CoO_xH_y ions are present and that the total signal from $CoOH^-$ and $CoOH_2^-$ increases after positive gating and decreases back to initial values upon negative gating. These results imply that some oxygen remains in the Co layer (or intermixed layer) and that the hydrogen driven in during positive gating penetrates this layer and forms a cobalt hydroxide phase. We conclude that the model of toggling between completely metallic and completely oxidized states is not fully accurate. In reality, CoO, Co, and CoO_xH_y phases may co-exist, with the relative prevalence of each phase changing under different hydration and gating conditions. These complexities would not be observable in MOKE measurements, which primarily probe the metallic Co. The $Pt/Co/GdO_x/Au$ devices in which CoO/Co toggling was previously measured using MOKE[4, 10] may or may not have displayed Pt, Co, and Gd intermixing and mixed Co, CoO, and CoO_xH_y phases. As long as some metallic Co was present, MOKE could still show transitions between a CoO/CoO_xH_y nonmagnetic state and Co-containing magnetic states.

The best fit also includes slight paramagnetism (less than 2 emu/cm^3) in the rest of Gd, including regions that are not next to Co, for all conditions. GdO_x nanoparticles have been shown to be paramagnetic at room temperature, so slight paramagnetism in the nanocrystalline GdO_x film is reasonable.[82]

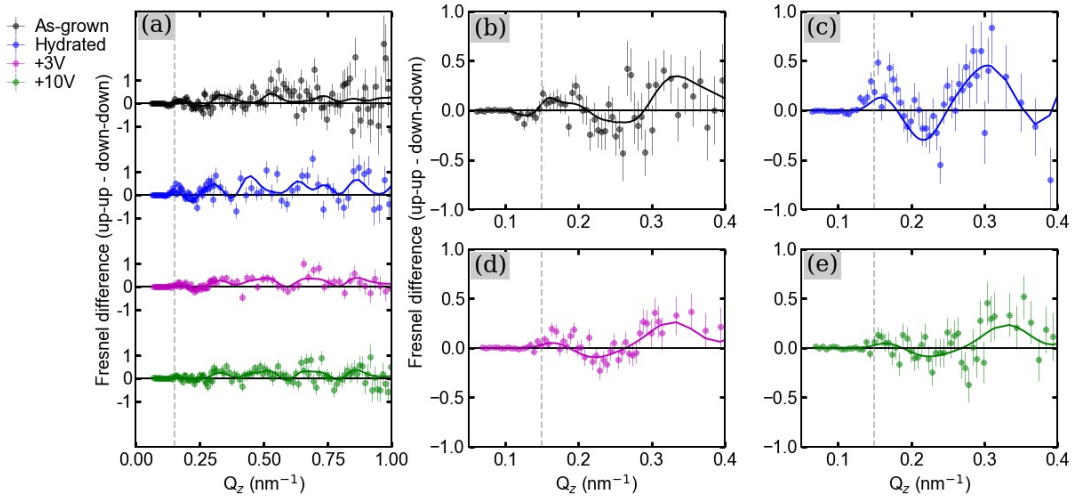

Figure 4-16: a) PNR Fresnel spin difference (↑↑ minus ↓↓) for the patterned sample, calculated from data in Fig. 4-10a. b-e) Enlarged views (Q_z=0 to Q_z=0.4) of the first four oscillations for each condition.

4.3 Conclusions from PNR and SIMS

We set out to investigate the effects of hydration and voltage gating on the structure and magnetization of the Pt/Co/GdO_xH_y/Au system. The structural PNR results showing depressed SLD due to hydrogen and the SIMS result showing signal from GdO_xH_y ions are the first direct measurements of hydrogen in the Pt/Co/GdO_xH_y/Au system and serve to support the models for phase transformation from oxide to hydroxide during hydration of GdO_x films and for water splitting and proton incorporation during positive biasing. NR results showed that during hydration, the SLD of the hydroxide layer is relatively constant, with the thickness increasing as the oxide/hydroxide interface moves deeper into the film. Upon vacuum annealing, the SLD of the hydroxide layer increases (reduces H content) uniformly before the layer thickness decreases. We observe an increase in the total integrated SLD of the GdO_x layer, which we attribute to irreversible uptake of oxygen. During voltage gating, H accumulates in the Co layer and in the GdO_x layer near the Co/GdO_x interface. The hydrogen concentration, the depth of the phase transformation front, and the amount of GdO_xH_y compounds all increased further with gating, indicating that incomplete

hydration of the film can be compensated by adding hydrogen during biasing. The gadolinium oxide layer was found to be either $Gd(OH)_3$, non-stoichiometric $Gd(OH)_3$, or a mixture of hydrated Gd_2O_3 and $Gd(OH)_3$ phases, and films of this material will be referred to as GdO_xH_y in the remainder of this work.

The prevailing model of this system suggested that voltage gating induced complete transformations between a nonmagnetic CoO state, an in-plane Co state with H loaded at the GdO_xH_y interface, and a PMA Co state with no H loaded. This work complicates that model. The PNR and SIMS results reveal the presence of CoO, CoO_xH_y, and a smaller-than-expected amount of Co, as well as a possibly intermixed layer of Pt, Co, and Gd that suppresses the net magnetization below the expected value. We conclude that lower temperatures during hydration or more optimized deposition could reduce intermixing and the evolution of unwanted species. Further, it may be possible to substantially tune the switching behavior and magnetization changes through judicious selection of the initial Co state. A partially oxidized CoO layer, for example, appears to evolve some fraction of Co hydroxide species, while such reactions may be suppressed in completely metallic Co. This work sheds light on the complicated interface chemistry and chemical irreversibility crucial to understanding and tuning voltage-controlled magneto-ionic devices.

4.4 Methods

4.4.1 Sample Growth and Hydration

Ta (4 nm)/Pt(10 nm)/Co (0.9 nm)/GdO_x (24 nm)/Au (3 nm) films were fabricated on thermally oxidized Si (100) substrates using magnetron sputtering at room temperature and 3.0 mTorr Ar pressure (except for the Au, which was grown at 3.5 mTorr Ar pressure). The metal layers were grown by DC sputtering. All GdO_x layers were deposited using DC reactive sputtering with P_{O_2} of 0.07 mTorr. 1mm by 1mm crossbar devices were patterned using shadow masks. In order to fit more devices within the neutron beam footprint, the arm width of the Au top electrode in the crossbars

outside of the active device area was reduced to 0.3 mm. The unpatterned GdO_x film for NR measurements was hydrated at 50 °C and 90% RH for 20 hours while NR scans were running continuously. The unpatterened sample for PNR measurements was hydrated for 6 days at 90 °C with a saturated K_2SO_4 solution keeping the humidity at 95% RH. The SIMS samples were unhydrated.

4.4.2 Gating

Device gating was done with a Keithley 2450 Sourcemeter. Devices were contacted with silver electrodes connected to a gold wire. See the PNR and SIMS methods sections for gating procedures before and during those experiments.

4.4.3 NR

Unpolarized neutron reflectometry was performed using the Polarized Beam Reflectometry (PBR) instrument at the NIST Center for Neutron Research (NCNR). The neutron beam was incident on the sample and the spin-dependent neutron reflectivities were measured as a function of the momentum transfer vector along the film normal direction ($\mathbf{Q}$). Measurements were performed in a temperature-controlled Al-walled chamber with relative humidity controlled by flowing nitrogen carrier gas through a dew point generator. See the supplemental section of Ref. [83] for further information about the humidity control. For the NR measurement of the hydration process of the unpatterned GdO_x film, the relative humidity was stable at 90% RH.

4.4.4 PNR

PNR measurements were performed using the Polarized Beam Reflectometry (PBR) instrument at the NIST Center for Neutron Research (NCNR). The incident neutron beam was spin-polarized parallel or antiparallel to the applied field, and the spin-dependent neutron reflectivities were measured as a function of the momentum transfer vector along the film normal direction ($\mathbf{Q}$). A 700 mT in-plane field was applied during measurements to saturate the magnetization in-plane. Since the samples

were expected to be saturated by this large field, we assume that there is no net in-plane magnetization component perpendicular to the applied field. Therefore, we measured only the non-spin-flip neutron reflectivities in which the spin of the neutron is the same before and after scattering. The two non-spin-flip reflectivities are $\uparrow\uparrow$ and $\downarrow\downarrow$, and are sensitive to the depth profiles of the nuclear SLD and the in-plane magnetization along the applied field direction. The spin-flip reflectivities, which are sensitive to the depth profile of the net in-plane magnetization perpendicular to the applied field, are assumed to be zero and were not measured. Reflectivities (R) are plotted as Fresnel reflectivities (R/R_{Si}) on a log scale throughout this paper.

PNR data reduction and fitting

PNR data reduction was performed using the Reductus software package,[84] and modeling of the reflectivity data was performed using the Refl1D software package.[85] The fitting parameters and constraints for this complex system of multiple layers, multiple regions, and multiple environmental conditions required careful consideration in order to give a reasonable physical result. Importantly, the incident neutron beam interacted with 7 distinct regions on the surface of the patterned sample, so that the resulting reflectivity must be modeled as an incoherent sum of the reflectivities originating in each layer, weighted by their relative cross sectional areas.[86, 87, 88, 85, 89] The probed surface included 40 mm^2 of device area:

1. $Si/SiO_2/Ta/Pt/Co/GdO_x/Au$

and a series of non-active regions:

2. Si/SiO_2
3. $Si/SiO_2/Ta/Pt$
4. $Si/SiO_2/GdO_x$
5. $Si/SiO_2/Au$
6. $Si/SiO_2/GdO_x/Au$
7. $Si/SiO_2/Ta/Pt/Co/GdO_x$.

See Figure 4-17 for SLD profiles for regions 2-7.

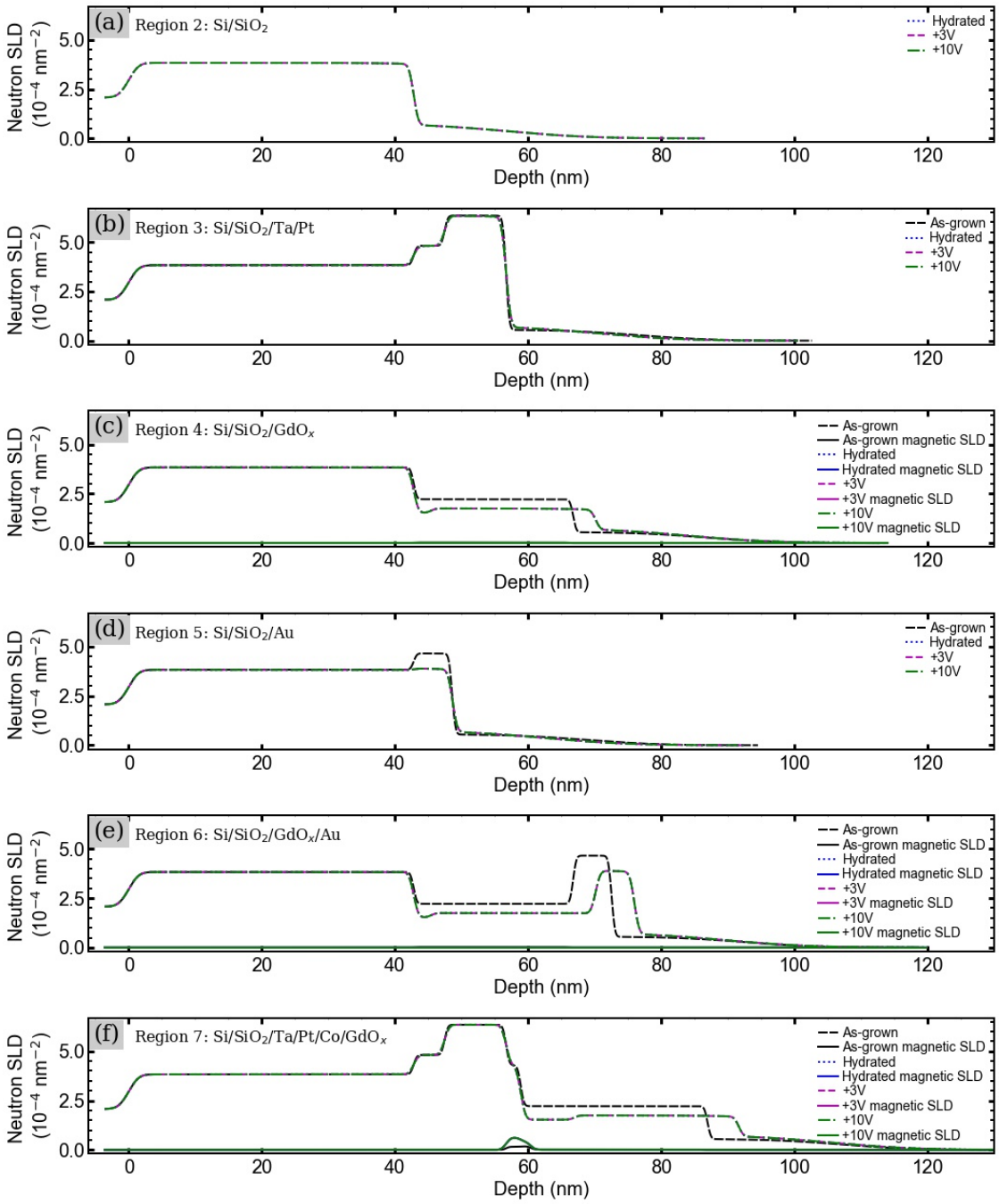

Figure 4-17: SLD profiles for all nonactive regions (i.e. non-device area) on the PNR sample. Plots a-f show profiles for regions 2-7, respectively.

In order to address the extremely wide accessible parameter space and potential for solution degeneracy when fitting PNR data as an incoherent sum of a 7 different regions, models were built using extremely strict constraints to enforce physicality and achieve consistency across all regions. Specifically, the following constraints were enforced:

a. The relative cross sectional areas of regions were determined by taking a photo of the sample on the sample holder with the mask defining the in-plane extent of the neutron beam in place. Region areas were determined directly from pixel areas with image processing software (ImageJ).[90] All relative areas were fixed to these ratios with the exception of region 2 (the SiO_2), which was allowed to vary to account for spread of the neutron beam due to vertical divergence, and the active device area, which was allowed to be a variable fraction of the total device area.

b. All layer thicknesses were constrained to match across regions. That is, all regions were assumed to have the same SiO_2 thickness, all regions with a Pt layer are constrained to have the same Pt thickness, etc. The only exception to this is the GdO_x layers grown on top of Co, where the Co layers are capped with a thin layer of GdO_x prior to the main GdO_x deposition process. Thus, regions 1 and 7 are fit with an identical, additional GdO_x layer in between the Co and main GdO_x region.

c. All layer SLDs were constrained to match across regions. That is, all regions were assumed to have the same SiO_2 SLD, all regions with a Pt layer are constrained to have the same Pt SLD, etc. The only exception to this is the active device region under bias, where the Au, GdO_x, and Co layer SLDs were allowed to vary relative to other regions to account for voltage-induced changes.

d. We measured the spin dependent neutron reflectivities under 4 conditions: as-grown, post-hydration, under bias at +3V, and under bias at +10V. For the post-hydrated state, PNR showed an increase in the GdO_x thickness and an associated reduction in the real SLD of this layer, as expected with increasing H concentration.

The total amount of Gd in the system was constrained to remain at its as-grown value, which we found by integrating the total imaginary SLD (neutron absorption) in the single layer of GdO_x in the as-grown state. This calculation is possible because Gd is a strong neutron absorber and is the only neutron absorbing element present in the stack. In the post-hydrated state and biased state, the absorption from the Gd was then divided between the two fit layers, allowing for the layers to have different thicknesses and neutron SLDs while conserving the total amount of Gd in the film. The thicknesses and SLDs of the two GdO_x layers were allowed to vary between the as-grown, post-hydration, and biased states, with the exception of the inactive device area, which was constrained to be identical in the post-hydration and biased states.

e. In addition to being constrained to be identical across regions, the Ta and Pt thicknesses and SLDs were fit but were constrained to be identical across all regions and under all conditions, since we do not expect hydrogen uptake in those layers.

f. The Co thickness was fit but was not allowed to vary between conditions, while the Co SLD was allowed to vary between the conditions.

g. Interface roughnesses were tightly constrained. In the as-grown and hydrated conditions, the Si/SiO_2 and surface adsorbate interface roughnesses were fit independently while all other interfaces were constrained to be identical for all layers and regions within each condition. This was also true for the +3 V and +10 V biased conditions, except for the active device region, where independent interface roughnesses were fit for SiO_2/Ta/Pt, Pt/Co/GdO_x, GdO_x/Au, and Au/surface adsorbates.

h. The Si SLD was set to the calculated theoretical bulk value for all regions on the sample and all conditions.

i. Gating large device areas is often challenging due to pinholes in the oxide layer. Because of this, we allowed for the device area to be fit in two separate regions, an

"inactive" or shorted device area and an "active" area. The fits always gave a 0% "inactive" device area, indicating that all devices were working as designed.

By so tightly constraining the models to enforce physicality and self-consistency, we dramatically shrink the parameter space necessary to explore when fitting the data and allow firm conclusions to be drawn. We note that while many of these constraints are at best physical approximations, they appear to be valid enough to lead to high-quality fits. Further, less constrained models generally do not improve the goodness of fit sufficiently to justify the additional parameters. For example, the decision to fix Pt and Ta SLDs even in the biased regions was tested using counterexample models in which these parameters were allowed to vary. While allowing variation in the Au, GdO_x, and Co of the active device region did improve the goodness of fit, no significant improvement was noted when freeing the Pt and Ta SLDs of this region and allowing them to vary. We reached similar conclusions regarding fitting independent layer roughnesses. Thus, while these constraints are approximations, they appear to be relatively good ones.

SIMS

SIMS was performed at NIST using an IONTOF IV (Münster, Germany) equipped with a 30 keV Bi_3^+ liquid metal ion source for analysis, a 20 keV $Ar_{2600\pm1000}^+$ cluster source for sputtering, and a time-of-flight mass analyzer. Depth profiling was performed using 1 scan of analysis, 10 scans of sputtering, and 2 s of charge compensation per cycle, where both the analysis and sputter rasters were kept inside a (300 × 300) µm area. The corresponding ion doses were 1.9×10^9 ions/cm^2 (0.12 pA) for Bi_3^+, and 2.1 $\times10^14$ ions/cm^2 (5.1 nA) per cycle for the cluster source. To be able to reliably detect H- ions, the pressure in the chamber was less than 5×10^{-7} Pa to minimize contributions from residual gases. Negative ions were used to avoid matrix effects arising from changes in oxygen concentration in the system. Peak assignments were made carefully after considering factors such as isotopic distributions and similarity in profile shape to other known oxide and hydroxide species. All profiles were nor-

malized to the area of SiO_2^- to compensate for drift in Bi_3^+ target current. The 1 mm crossbar devices used for SIMS measurements were grown using the same DC magnetron sputtering parameters as the PNR samples described above. The layer structure was also the same Ta(4 nm)/Pt(10 nm)/Co(0.9 nm)/GdO_x(24 nm)/Au(3 nm). Three different devices were tested: one as-grown (never gated) device, one gated at +3 V for 10 minutes, and one gated at +3 V for 10 minutes and then -1 V for 30 minutes. Due to the time required to load the sample into the SIMS instrument and pump down, there was an approximately 30 minute to 1 hour gap between gating and the SIMS measurement, during which the device was uncontacted (held at open circuit).

XRR

XRR was performed at the MIT Materials Research Science and Engineering Center on the Bruker D8 High Resolution XRD. The measurements were performed with Cu K-α x-rays (8.04 keV) with a beam current of 40 mA. The samples were heated from room temperature to 300°C in steps of 10°C, for 2 temperature cycles. It took about 3.5 minutes to reach the set temperature at each step, after which the sample was held at the temperature for 30 s, before running the XRR scan for about 2.5 minutes.

Chapter 5

Electrical characterization of $Pt/GdO_xH_y/Au$ device

The $Pt/GdO_xH_y/Au$ stack is the simplest case, a device with no magnetic layer and no charge storage in the electrode (platinum has much lower hydrogen solubility and diffusivity compared to the palladium used in other stacks). This allows us to measure proton transport and hydrogen storage properties of GdO_xH_y itself. All measurements in this chapter were done on a $Si/SiO_2/Ta$ (4 nm)/Pt (10 nm)/GdO_xH_y (22 nm)/Au (5 nm) crossbar device. The dimensions of the devices were 350μm $\times$350μm (see Figure 3-1 for a schematic and optical image of the crossbar device).

5.1 Typical current vs time and IV curves

These devices have properties of batteries, capacitors, and memristors. The resistance of a "working" device can range from kΩ to GΩ depending on the area, electronic resistance, humidity, and time spent under positive bias (there is some evidence that "easy" proton conduction pathways can be established during gating, decreasing the device resistance from its initial value[23]). For a capacitor, we expect a square IV curve and a current vs time charging curve that drops off within an RC time constant as the capacitor reaches its maximum charge state. This applies for both the electronic capacitance and the ionic capacitance (charging of the double layer).

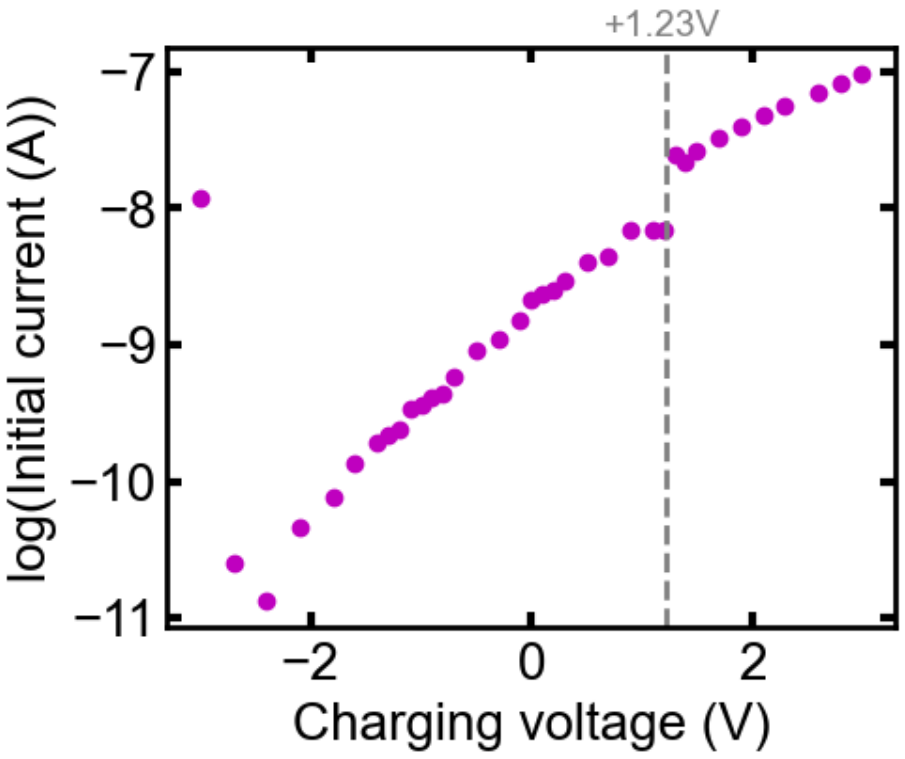

Figure 5-1: Log of the initial current after a voltage step to the given voltage, showing the jump in current with the onset of ionic current at the water splitting voltage (+1.23 V).

Figure 5-1 shows the initial (transient) current as a function of voltage. For each data point, the device was completely discharged by holding it at -3 V for 100s, then the voltage was stepped up to the charging voltage and held for 30 s. There is a jump in current at +1.23 V, the voltage required for water splitting at the top electrode, indicating that an ionic current flows at voltages above this value.

The GdO_xH_y devices conduct both electronic and ionic current, which can both respond differently to voltage and to environmental conditions. Both electronic and ionic current can be thought of as a single charge-transfer reaction at the interface, modeled by a Schottky barriers (with different barrier heights). The electronic charge transfer can occur at any overpotential, while the ionic charge transfer occurs through a redox reaction with the water adsorbed on the electrode (Equation 2.2) and only "turns on" once this water splitting overpotential is reached.

The electronic resistance state of a given device can vary. If the formation of an

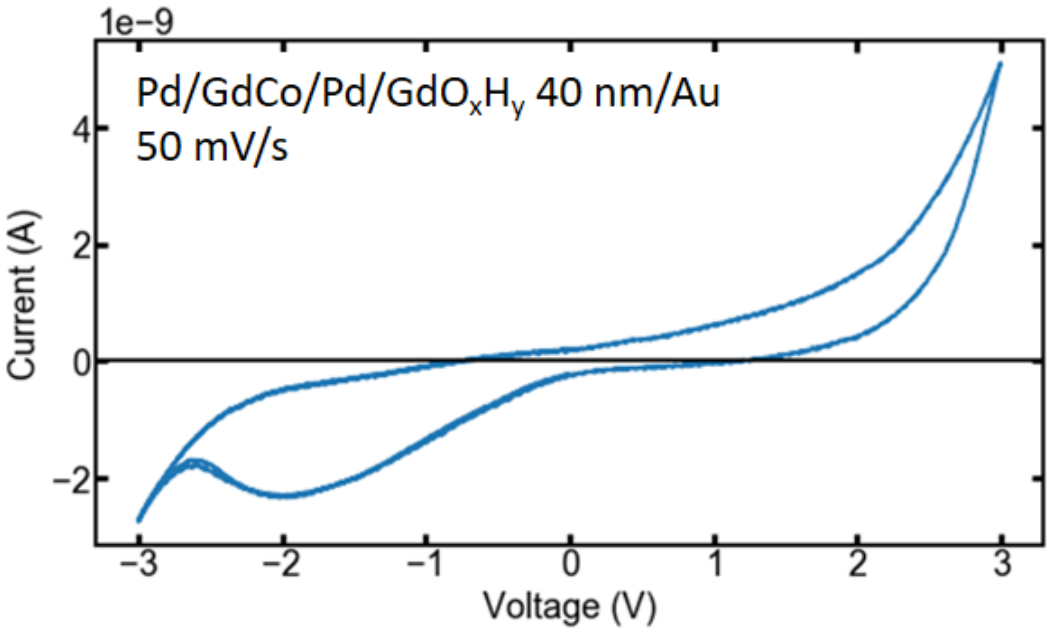

Figure 5-2: A typical hysteretic CV curve, taken at a sweep rate of 50 mV/s. The peaks in the CV curve indicate diffusion-limited reactions, telling us that redox reactions are occuring in the device and protonic current is flowing.

electronic-conducting filament occurs (similar to a VCM memristor device), the device can jump from a high-resistance state dominated by ionic current to a low-resistance state dominated by electronic current. The IV curve shifts from the hysteretic "butterfly curve" shown in Figure 5-2 to the higher-current, non-hysteretic IV curve shown in Figure 5-3. The ionic current is highly dependent on the relative humidity. This makes sense because the protons injected into the device at the Au electrode come from ambient water vapor. The amount of ionic current therefore depends strongly on voltage and on %RH. The electronic current does not depend on %RH. Figure 5-4 shows this difference in %RH dependence for devices that are in the ionic-dominated (high resistance) and electronic-dominated (low resistance) states.

While it is useful to think of the "low-resistance" and "high-resistance" states as binary options, the reality is the the resistance state can take on intermediate values (i.e. the device behaves as a memristor with many possible resistance states). We found that the devices can jump between resistance states seemingly stochastically, especially at high voltages (typically ±3 V or greater), although we have not inves-

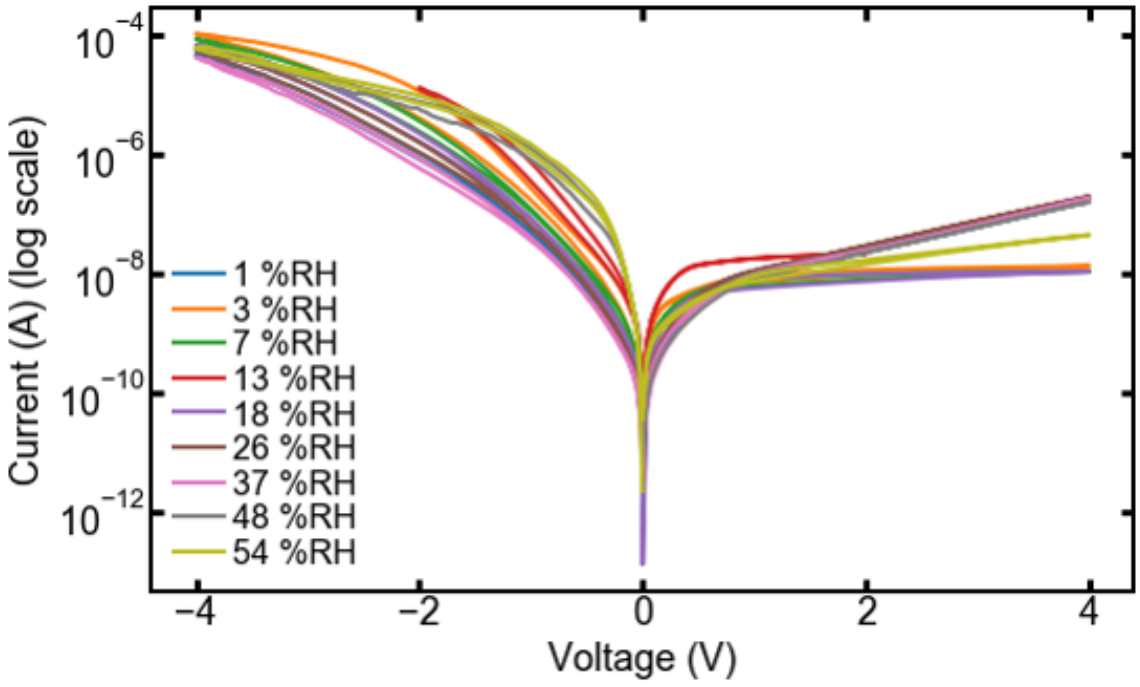

Figure 5-3: A typical set of non-hysteretic IV curves in the low-resistance state, dominated by electronic current. Here the device is Ta/Pd/GdCo/Pd/GdO_xH_y (40 nm)/Au, measured at a series of %RH values.

tigated this in a statistical way. Sudden resistance switching also seems to happen more often at higher RH. This can make consistent operation of the device difficult. We assume that this is due to conductive filament formation, leading to the sudden formation of a highly conductive electronic pathway.

5.2 Measuring ionic current and stored charge

For most electrochemical measurement techniques, the material is assumed to be either an electronic or ionic conductor. Due to the very thin dimension of the GdO_xH_y devices, we must always be aware that both ionic and electronic currents are present. For example, when measuring the amount of hydrogen stored or released while charging or discharging a device, we must assume that a significant fraction of the current is electronic, not due to proton transport, and is not contributing to the hydrogen storage.

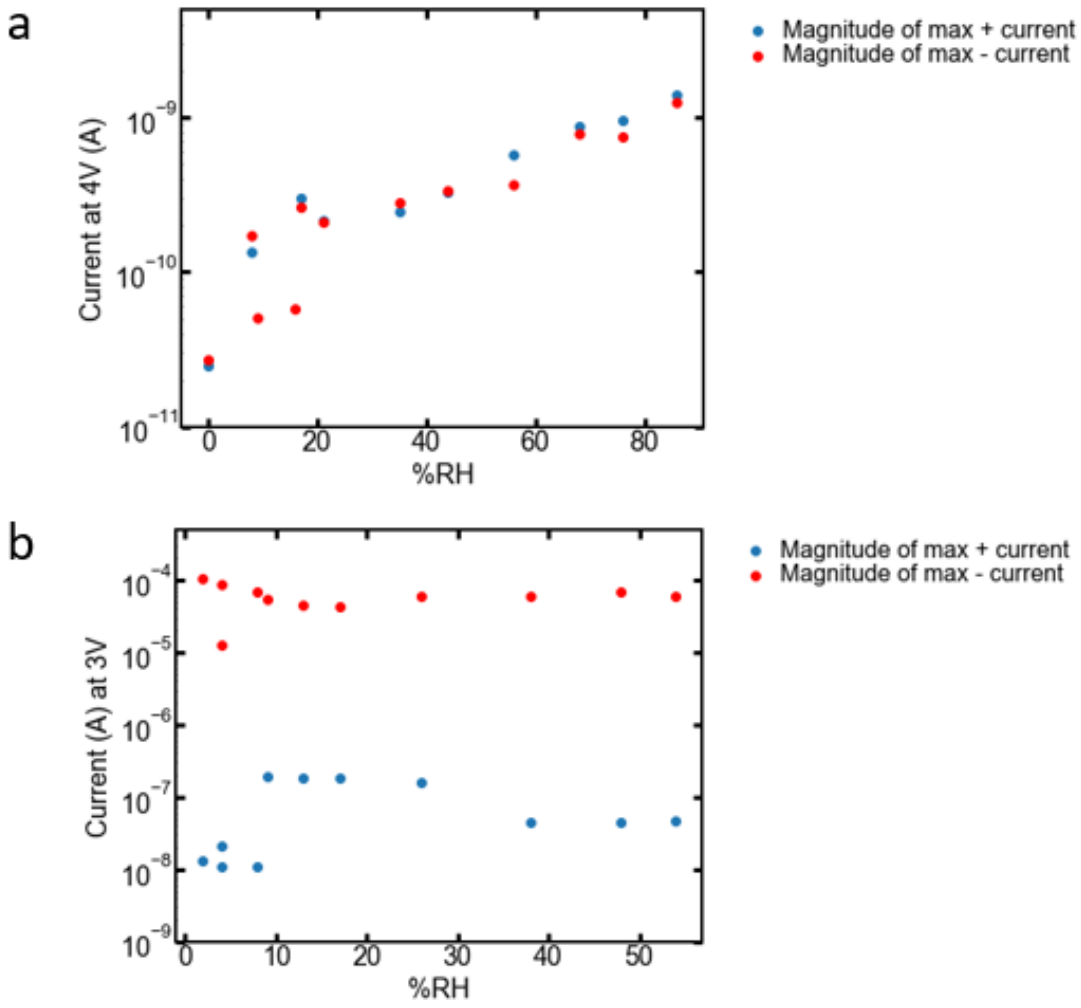

Figure 5-4: a) Current value at +4 and -4 V taken from IV curves for a device in the high-electronic-resistance state (characterized by IV curves shown in Figure 5-2). The magnitude of the current increases exponentially with %RH. b) Current value at +3 and -3V for a device in the low-electronic-resistance state (data taken from Figure 5-3). The magnitude of the current is constant with changing %RH. Note that the %RH and current ranges are different for each subplot. Here the device is again a Ta/Pd/GdCo/Pd/GdO_xH_y (40 nm)/Au. A GdCo device was used for convenience; since we are not measuring charge storage or magnetic switching, the Pd and magnetic layers in the device should not affect the measurement.

We have measured the conductivity of the GdO_xH_y using electrochemical impedance spectroscopy (see section 2.3.2 for a description of this technique), in collaboration with Dr. Sunho Kim from Professor Harry Tuller's lab group. We were not able to extract the proton conductivity from this data due to the large number of overlapping semicircles representing different conduction mechanisms with very similar RC timescales. This was attributed to the nanocrystalline, possibly multiphase nature of the GdO_xH_y films, in addition to the possibility that heating the film was causing a layer of less hydrated hydroxide or oxide. The grain boundary contributions in addition to multiple layers with different hydration states could have contributed to the existence of 6 or 7 different overlapping semicircles. See Dr. Kim's thesis, Ref. [73] for the impedance spectroscopy data and analysis (in that reference "oxide from collaborators in the Beach group" refers to the RF sputtered GdO_xH_y examined in this thesis).

To deal with this, we have developed a technique based on CV to measure the ionic current during discharge of a device. The ionic discharge current cannot flow forever – once there is no more hydrogen left to discharge, it must go to zero, leaving only electronic current. To take advantage of this, we do several negative sweep cycles (where one cycle is e.g. 0V to -3V and back to 0V) at a fixed sweep rate. The ionic current flows during the first cycle, discharging stored hydrogen (which leads to one or more CV peaks, indicating that this is a diffusion-limited process). Typically, by the second cycle, all of the hydrogen has been driven out, so the second, third, fourth, etc. cycles lie more or less on top of each other. We assume that these currents are entirely electronic, since there are no more ionic species to transport. Figure 5-5 shows an example of a series of CV sweeps demonstrating this phenomenon.

To calculate the total ionic charge discharged, we subtract the last cycle (the purely electronic current) from the first cycle. Assuming the electronic current value (electronic resistance state) has not changed during this process, this leaves only the ionic current. While it is conceivable that the electronic conductivity of the electrolyte could depend on the concentration of hydrogen in the electrolyte, Figure 5-6 shows that the electrical current through the device is similar in the loaded and unloaded

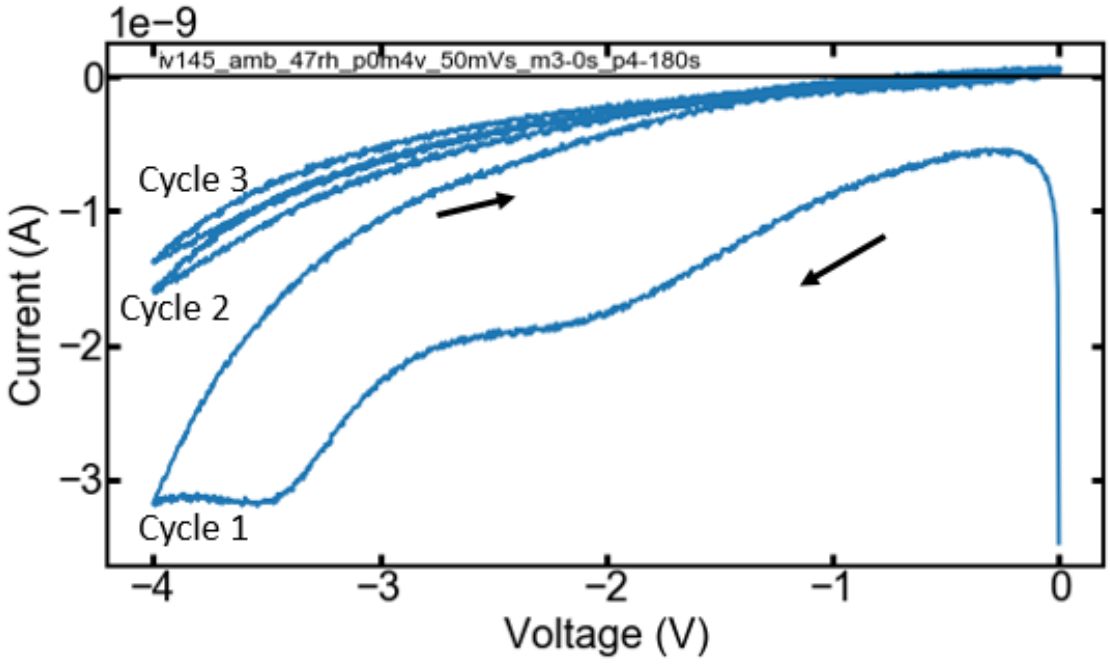

Figure 5-5: Example of a multi-cycle cyclic voltammetry sweep, showing that the stored charge is discharged through the first sweep (leading to 2 CV peaks), and only electronic current is present in the subsequent two cycles. This Ta (4 nm)/Pd (6 nm)/GdCo (8 nm)/Pd (6nm)/GdO_xH_y (22 nm)/Au (3 nm) device was held at +4V for 180s, then discharged over 3 CV cycles with a sweep rate of 50 mV/s.

states. We integrate this ionic current to get the total ionic charge, which corresponds to the amount of hydrogen driven out.

5.3 Model of charge storage

Figure 2-5 shows how charge is stored in the Pt/GdO_xH_y/Au battery. During charging (positive bias), water is split at the top electrode and protons are incorporated into the oxide. The protons are transported through the oxide by the electric field. When they reach the back electrode, the protons are reduced to atomic hydrogen. In the Pt/GdO_xH_y/Au device, the hydrogen is stored primarily in the oxide itself. In Chapter 6, we will see that the hydrogen can also diffuse into adjacent layers to modulate their properties, either through interface effects or through diffusion into the bulk.

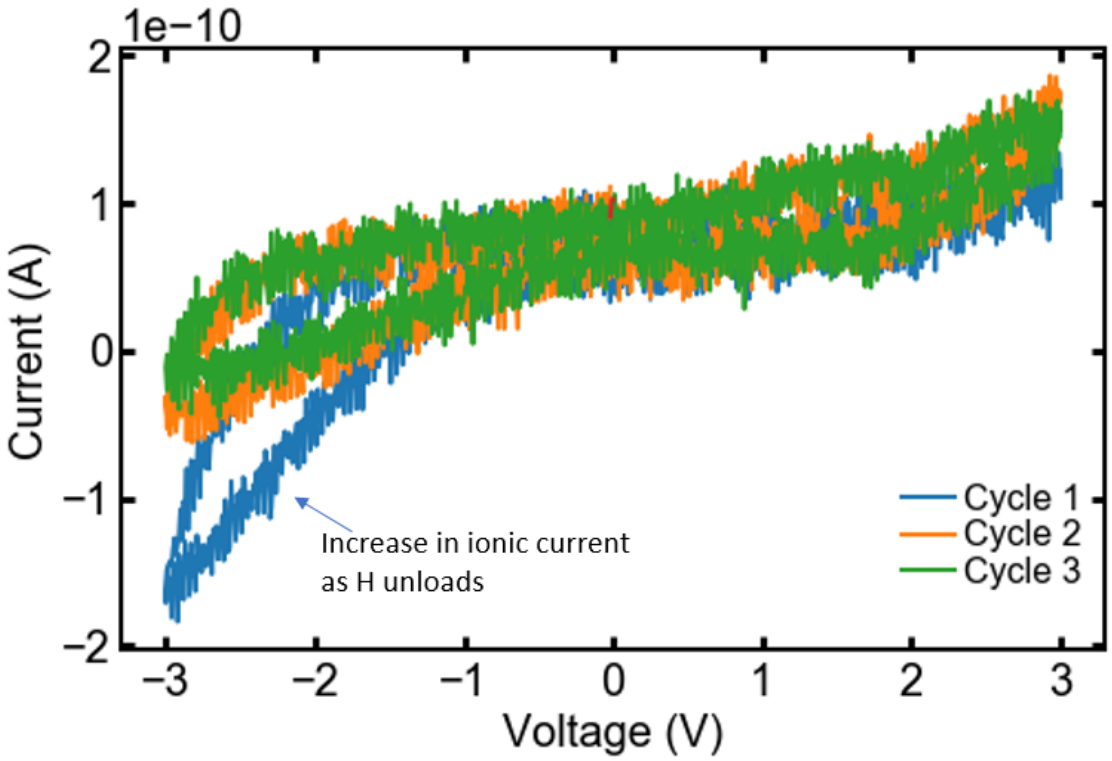

Figure 5-6: IV sweeps demonstrating that the current is the same in the hydrogen-loaded and -unloaded states. This Ta (4 nm)/Pd (6 nm)/GdCo (8 nm)/Pd (6nm)/GdO_xH_y (22 nm)/Au (3 nm) device was charged at +3 V for 150 s. The device changed from light colored to dark colored, indicating hydrogen was being stored. The probe was then lifted and the chamber was pumped down to a vacuum pressure of 1 mTorr. The device color remained the same, meaning that the hydrogen did not leak out during pumping and the device was still in the loaded state (the color would have lightened had the device discharged during pumping[6, 5]). The probe was relanded and the voltage was swept from 0 to +3 to -3 and back to 0 V three times. The positive current in the loaded state (Cycle 1) is the same as the positive current in the unloaded state (Cycles 2 and 3). The more negative current in the negative sweep of Cycle 1 is the ionic current generated as the hydrogen discharges and is released into the environment as hydrogen gas (due to the lack of oxygen).

As we can see in Figure 3-1b, the oxide is grown as a continuous layer (the oxide appears blue in the photo, and covers the entire field of view). This is done to avoid unnecessary patterning steps during device fabrication. It was previously assumed that the area under the electrodes was the only active area in the device, and that the protons traveled directly to the back electrode, and that the hydrogen was stored either at the Pt/GdO_xH_y interface or in the oxide within the device volume. However, since the oxide is a continuous large area film, protons can also diffuse laterally outside the device area. This lateral diffusion over time allows us to measure the diffusivity of the protons in the oxide.

5.3.1 Diffusivity measurement

When protons enter the GdO_xH_y (increasing the proton concentration in the hydroxide), they can change the refractive index.[6] This phenomenon leads to a lightening of the film, visible in areas where the oxide is on top of the Pt back electrode (see Figure 5-7). Measuring the position of this white proton front as a function of charging time allows us to calculate the diffusivity of protons in the GdO_xH_y, as the transport of the protons outside the square device area is purely diffusive. For a constant-concentration source, the diffusion front position is related to time by the equation $x = \sqrt{Dt}$. Figure 5-8 shows a plot of the position versus the square root of time and the linear fit (with $R^2 = 0.9894$) which gives a diffusivity value of $D = 2.07 \times 10^{-7}$ cm^2/s.

We can also measure the diffusivity magnetically, by putting the MOKE laser spot off of the device and measuring how long it takes to see a magnetic change after beginning gating of the nearby device. With the laser spot 14.8 um off edge of 50x50 um GdCo device, it took 378 s at +3 V to switch. This gives a diffusivity value of $D = 5.8 \times 10^{-9}$ cm^2/s. This value is two orders of magnitude smaller than that calculated with the Pt/GdO_xH_y/Au device. This difference could be due to extra time needed for the hydrogen to diffuse through the Pd capping layer over the GdCo (effectively adding 6 nm more material to diffuse through) or the time required for the hydrogen to diffuse into the GdCo itself. It could also be that a much lower concentration

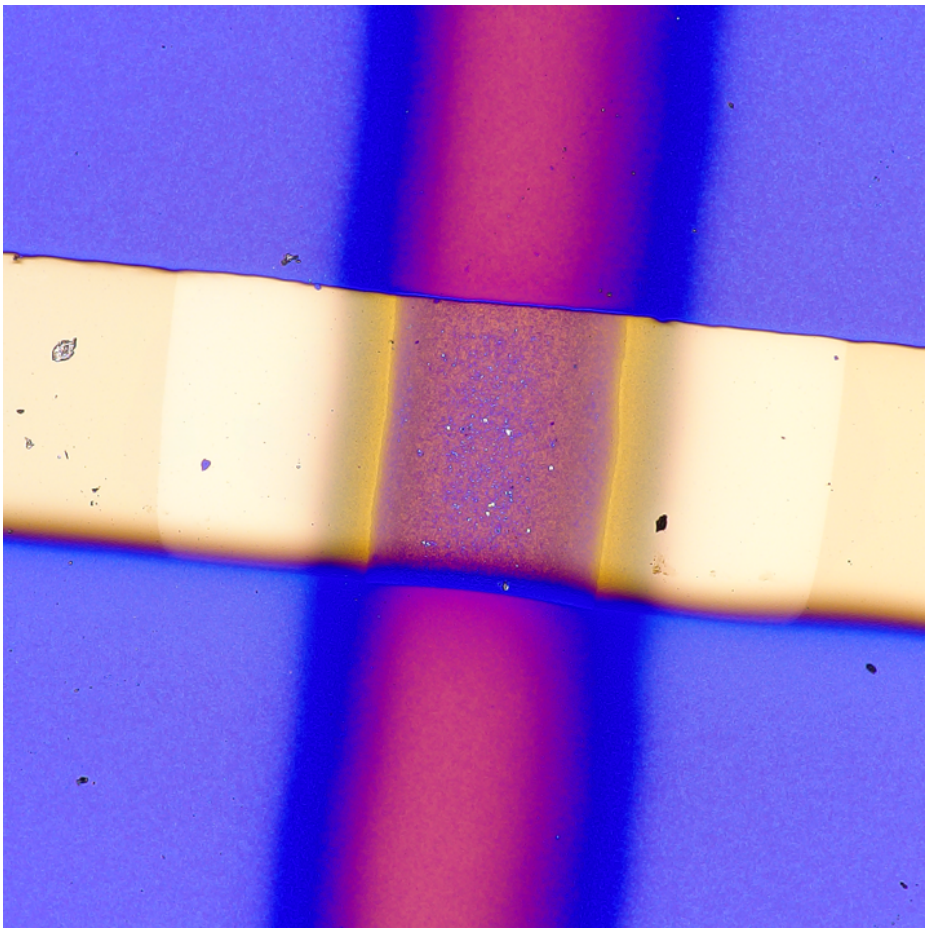

Figure 5-7: Optical image showing the lighter area of higher proton concentration on top of the horizontal Pt back electrode. The vertical stripe is the Au top electrode, which lies on top of the oxide. The square is therefore the device area. The white area is initially not present and extends out farther from the device with longer charging at positive voltage.

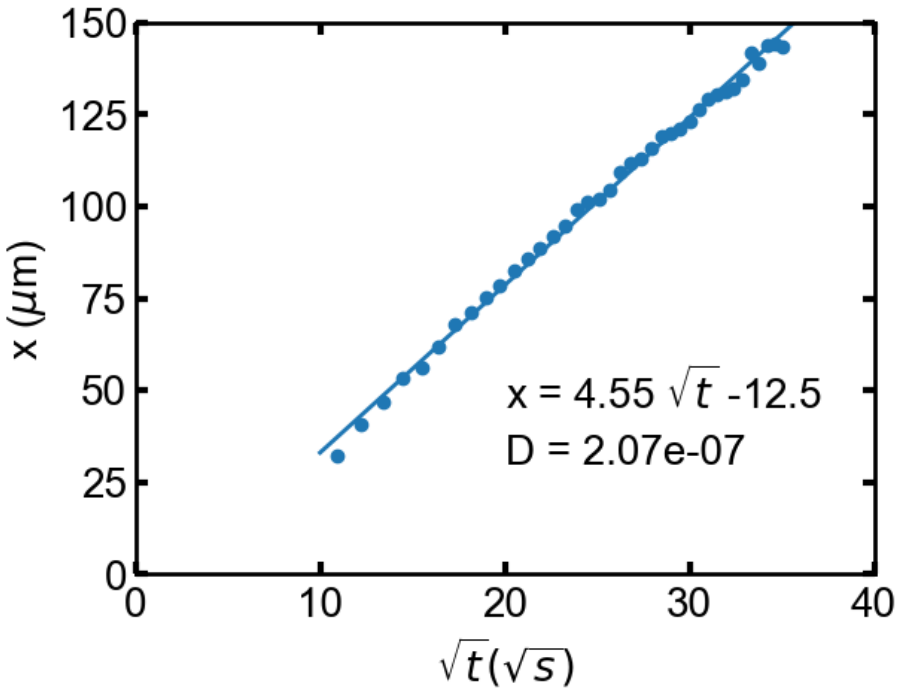

Figure 5-8: Position of the proton front (white region) vs square root of time for the device shown in Figure 5-7. The slope is equal to the square root of the diffusivity, D, giving a value of $D = 2.07 \times 10^{-7}$ cm^2/s.

of protons is required to change the refractive index of the oxide (causing the visible whitening of the oxide which allowed us to measure the diffusivity above) as compared to the concentration required to get enough hydrogen into the GdCo to cause magnetic switching. This is less likely given that relatively small amounts of hydrogen have been shown to successfully induce switching in GdCo, as discussed in Chapter 6. Going forward, we take the diffusivity measured in the Pt/GdO_xH_y/Au device as the proton diffusivity value in GdO_xH_y, given the confounding factors present in the Pd/GdCo/Pd/GdO_x/Au device.

5.3.2 Implications for device charge capacity

Initially we began measuring the "capacity" of Pt/GdO_xH_y/Au devices using standard battery techniques, i.e. charge for some time and then discharge at a fixed small current and measure the amount of current that comes out to get the total amount of charge stored. This does not quite work for these devices for several reasons.

First, the oxide is a mixed ionic and electronic conductor (MIEC), and therefore a significant fraction of the current is electronic rather than Faradaic (due to redox reactions from hydrogen being stored and released). This is also true of traditional batteries, but to a much lesser extent, since microbatteries are typically thicker and have significantly higher electronic resistance and lower electronic current. Second, a traditional battery capacity measurement assumes that most of the charge that is stored will come back out during discharge. In our devices, the hydrogen is not only stored in the oxide in the active device volume under the electrode, but can also diffuse away from the electrode. This charge is "lost", as some of it will diffuse far enough away that it is not recovered during the negative CV sweeps we use to measure ionic current discharged. Figure 5-9 demonstrates that for longer charging times, less and less of the charge that was put in is recovered during discharge, for the same set of charging voltages. The figure shows the total integrated charging current and the total integrated ionic current during discharge (calculated by subtracting the final CV loop from the initial, as described in section 5.2) for a range of charging voltages and for four different charging times. The total charging current for each voltage was approximately the same for each charging time, (i.e. the ratio of electronic current to ionic current during charging was the same for each charging time), therefore this loss of efficiency cannot be explained by higher electronic current or lower ionic current during charging. Focusing on the shortest charging time, 5 s, in Figure 5-9a, we can use the integrated discharge current to estimate the amount of charging current that was protonic vs electronic. For example, we see that the integrated ionic current during discharge is about 75% of the value of the total integrated charging current at +3 V. For this short charging time, it is reasonable to assume that nearly all protons that were put in were recovered, since the protons would have been able to diffuse only 10 μm and would not have been able to leave the device area. Therefore, we estimate that about 75% of the charging current at +3 V was protonic current.

In the Pd/GdCo/Pd/GdO_xH_y/Au devices described in the next chapter, the atomic hydrogen can also diffuse into the Pd and can be lost that way. The Pd has a very large hydrogen solubility and a diffusivity near the same value that was

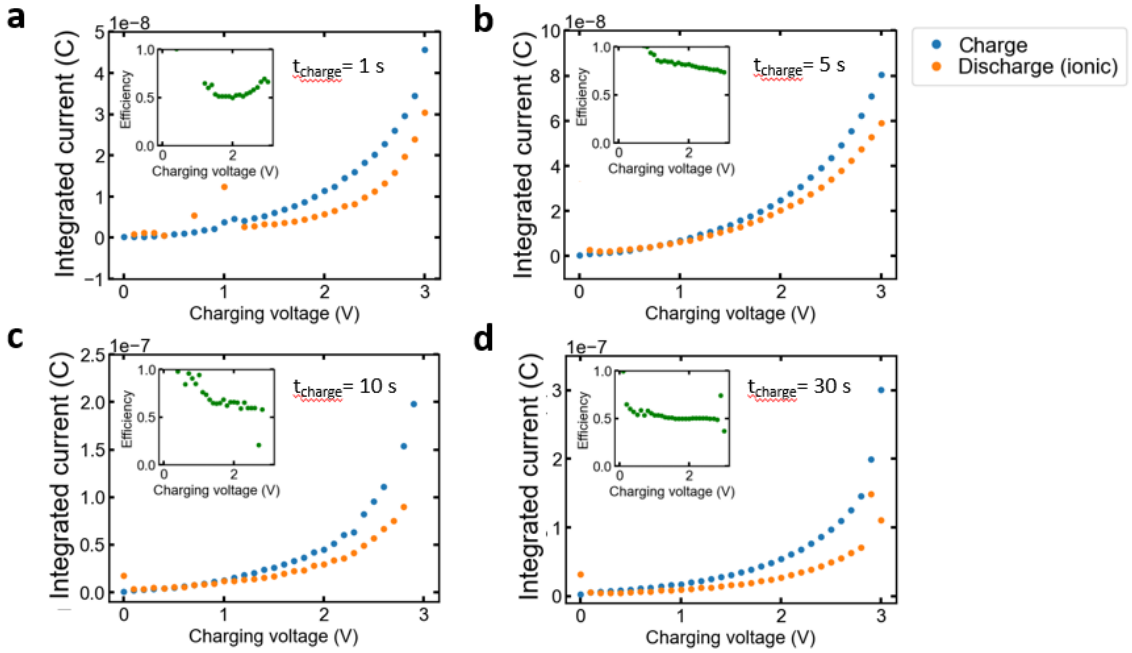

Figure 5-9: a) $t_{charge} = 1$ s, b) $t_{charge} = 5$ s, c) $t_{charge} = 10$ s, d) $t_{charge} = 30$ s

measured for protons in GdO_xH_y, around 3×10^{-7} cm^2/s. In devices with a Pd layer (intended to protect the GdCo magnetic layer from oxidation), the measured capacity continues increasing for very large charging times at +3 or +4 V (upwards of 1 hour) since the oxide and the Pd both have effectively infinite capacity for protons and hydrogen (Figure 5-10). Even for these large charge times, the amount of hydrogen in the Pd is estimated to be less than 1% of the total H capacity of $PdH_{0.7}$, the theoretical maximum capacity of PdH_x.

The charging voltage also affects the amount of hydrogen that can be recovered from the device. Figure 5-11 gives the integrated charging and discharge ionic currents for a range of charging times at three different voltages. The apparent capacity plateaus in each case, likely due to the injected protons diffusing away from the electrode and not being recovered during the discharge period (which has a fixed length for each trial). For a longer charge time, the protons have more time to diffuse away, and only the protons within the diffusion radius determined by the discharge time can be recovered as ionic current during discharge. For the calculated proton diffusivity of 2.07×10^{-7} cm^2/s and a typical discharge time of 6 minutes, the radius

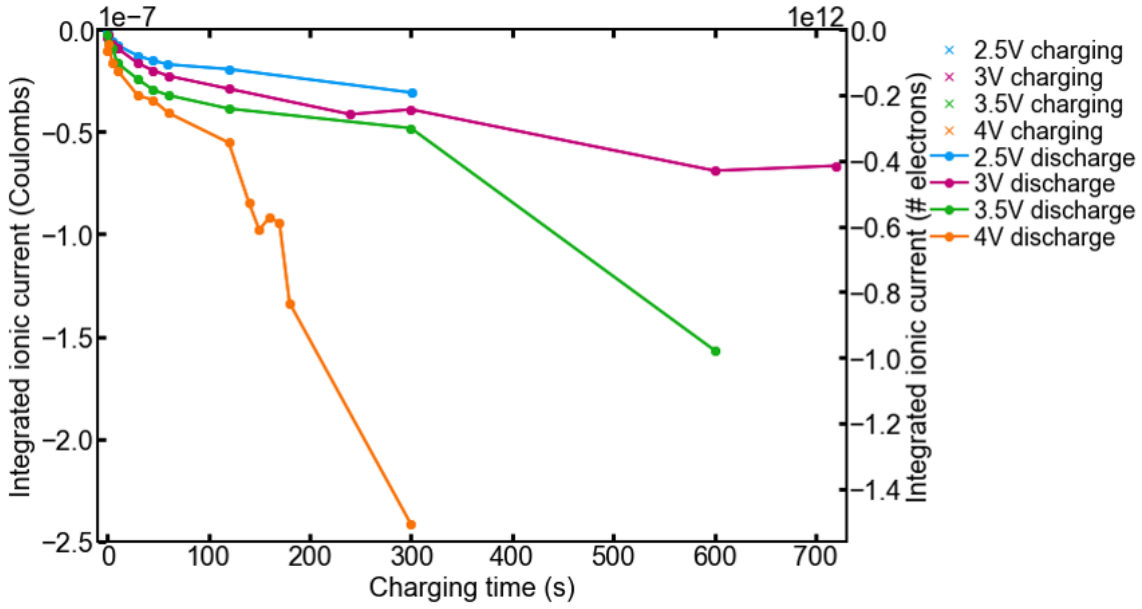

Figure 5-10: Integrated ionic charge measured using the CV method described in section 5.2 as a function of charging time for a Pd/GdCo/Pd/GdO_xH_y/Au device. The charge stored does not level off even for very long charging times, indicating that the hydrogen is being stored in the Pd.

from which protons in the oxide can be recovered is about 9 μm. At +1 V, the saturation capacity is about 1.5×10^{-7} C; at +2 V it is about 4×10^{-7} C, and at +3 V it is about 1.5×10^{-6} C (one order of magnitude greater than the value for +1 V). A possible explanation for this phenomenon is that the higher voltage pumps more hydrogen in faster, but the diffusion rate away from the electrode stays constant, meaning that for larger charging voltage the concentration of protons in the oxide near the electrode is higher. This means more protons make it back to the electrode during discharge, leading to a higher apparent capacity.

Here we note that the device does show some measurable charging at +1 V despite being below the theoretical water splitting voltage. It is not clear why this is; it could be due to free water internal to the device acting as the proton source and still allowing for water splitting and proton incorporation at the top electrode.

Lastly, we measure the charge storage as a function of RH during charging. Results are shown in Figure 5-12. The protonic charge to total charge ratio can again be taken to represent the amount of the original charging current that was protonic. These

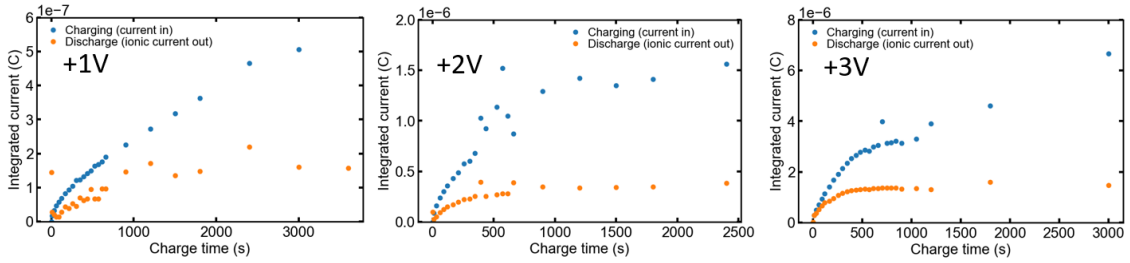

Figure 5-11: Ionic current integrated during discharge as a function of charging time for charging voltages of a) +1 V, b) +2 V, and c) +3 V. These plots show an apparent increase in charge storage capacity for increased charging voltage.

measurements were taken for a long charging time (300 s), so the measured ratios of protonic current out to total current in are lower than they should be (around 0.2 rather than the >50% protonic current measured in similar devices at short charging times. However this data does show us the general trend of increasing protonic current for increasing RH, as expected for a device where transport of H_2O to the top electrode or the water splitting reaction itself plays an important role in the device kinetics.

5.4 Device modeling

It is useful to build a general model of devices to predict their performance under different conditions or stack modifications. To this end, we modify a device model developed by Huang et al. to describe electrochemical ionic synapses (EIS).

An EIS is a device that mimics a neural synapse by changing the electrical conductance of a channel. The conductance is modified by pumping ions (e.g. protons) into the channel; controlling the ion concentration in the channel changes the conductance in a predictable way. An EIS has a reservoir layer that acts as an ion source, a channel layer across which the conductance can be measured, and an electrolyte material between the reservoir and the channel with a high ionic conductivity. Electrical contact is made to the reservoir layer with a gate electrode. Electrical contact is made across the channel with separate source and drain electrodes, such that current can flow across the channel independently of the gate current that modulates the ion flow into or out of the channel (similar to a transistor). Figure 5-13 illustrates the

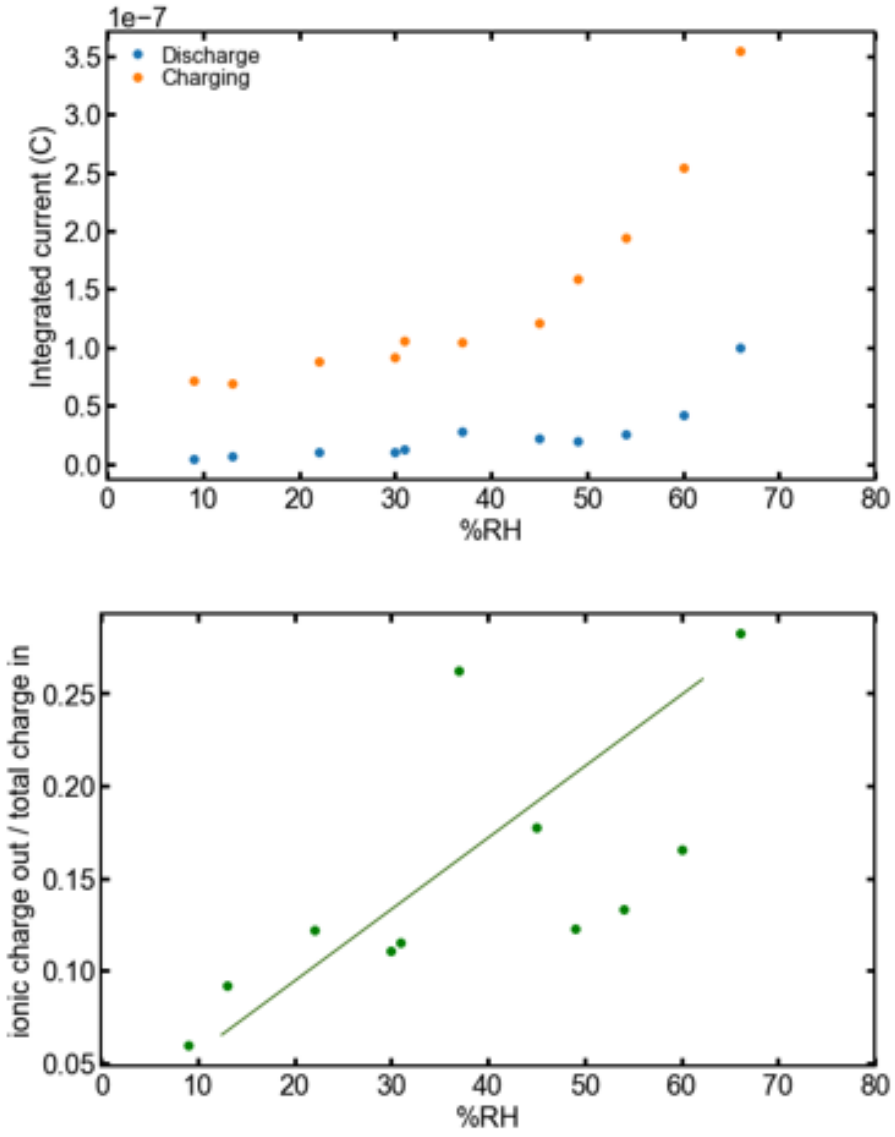

Figure 5-12: a) Total current integrated during charging (orange) and protonic current integrated during discharge (blue) as a function of %RH during charging at +3 V for 300 s. b) Ratio of the discharge charge capacity to the charging current (ratio of blue to orange from a)), indicating how much of the charging current was protonic.

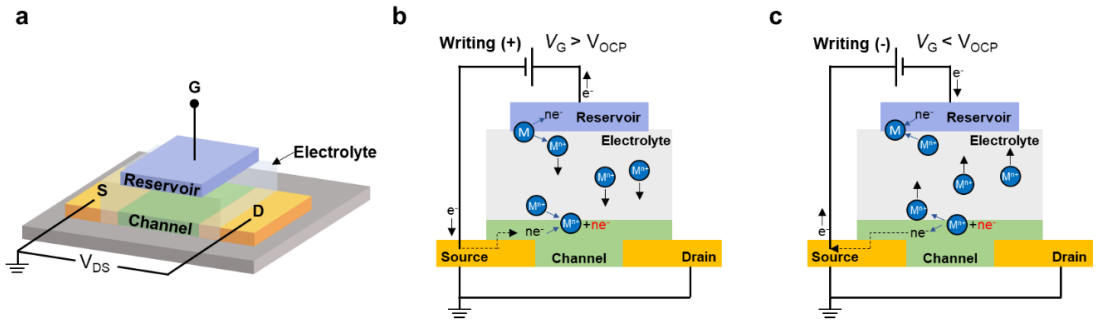

Figure 5-13: a) EIS device schematic illustrating the gate electrode, reservoir, electrolyte, channel, source, and drain. b) For a gate voltage (V_G) greater than the open circuit voltage (V_{OCP}), ions from the reservoir are oxidized and travel through the electrolyte into the channel, modulating the channel conductance. c) For $V_G < V_{OCP}$, the reverse process occurs and ions are extracted from the channel. Figure reprinted from Reference [11] under a CC BY-NC 4.0 license.

structure and operation of an EIS.

EISs are very similar to our GdO_xH_y devices; the main differences are that our "reservoir" is just the ambient water vapor, and that we do not always have a channel layer, as hydrogen can be stored in the GdO_xH_y electrolyte itself. For the magneto-ionic devices described in Chapter 6, the Pd/GdCo/Pd magnetic layer into which we pump hydrogen is the channel layer, and rather than modulating the conductance, we are modulating the magnetic properties.

The EIS model developed by Huang et al. describes this device with an equivalent circuit model that consists of three parallel R-C circuit elements in series – one for the reservoir-electrolyte interface, one for the electrolyte itself, and one for the electrolyte-channel interface. Thus, the R and C components of the interfaces and the electrolyte can be described separately. The authors found that the key parameters that predict device performance are the exchange current density j_0, which describes the reaction current at the interfaces, and the ionic conductivity of the electrolyte, σ_0. To have a fast device, we need both the interface reactions and the transport across the electrolyte to be fast. The authors found that fast operation (<10 ns voltage pulses) requires $j_0 > 0.1 - 1$ A/cm^2 and $\sigma_0 > 10^{-4}$ S/cm.

To calculate j_0 for our GdO_xH_y devices, we assume a Butler-Volmer model for the

redox reactions at interfaces. The Butler-Volmer model for a single charge transfer reaction assumes that the reaction current density at the electrode, j, is exponentially dependent on the overpotential η:

$$j = j_0 \left(\exp\left[\frac{(1-\alpha)zq}{k_B T}\eta\right] - \exp\left[\frac{-\alpha zq}{k_B T}\eta\right]\right) \tag{5.1}$$

where α is the charge transfer coefficient (describing the symmetry of the forward and backward reactions, with $\alpha = 0.5$ giving symmetric current values for both directions), z is the number of electrons involved in the charge transfer reaction, q is the elementary charge, k_B is the Boltzmann constant, and T is the temperature. The log of this current density versus voltage (a Tafel plot) should have a straightforward linear fit from which we can calculate j_0. Figure 5-14 shows the Tafel plot for a $Pt/GdO_xH_y/Au$ device. The j_0 value extrapolated from the linear fit is 1.6×10^{-8} A/cm^2, which is 7 orders of magnitude smaller than the target value given by Huang et al. This indicates that the interface reactions in our devices are limiting their operation speed, and we may not be able to achieve 10 ns operation.

Next, we need to estimate the value of σ_0 for the device, in order to compare the relative speed of proton transport across the oxide electrolyte. We first use the proton diffusivity value calculated in section 5.3.1, and use the Einstein relation to calculate the proton mobility:

$$\frac{D}{\mu} = \frac{k_B T}{q} \tag{5.2}$$

Our diffusivity value of $D = 2.07 \times 10^{-7}$ cm^2/s gives a proton mobility of $\mu = 8.0 \times 10^{-6}$ cm^2/Vs. Conductivity is calculated from mobility using the following equation:

$$\sigma = \mu q c_{\text{ion}} \tag{5.3}$$

where c_{ion} is the ion concentration and q is again the elementary charge. Plugging in the proton mobility and estimating the proton concentration as that of stoichiometric $Gd(OH)_3$, $c_{\text{ion}} = 4.8 \times 10^{22}$ cm^{-3}, we get an estimated ionic conductivity of 6.3×10^{-2} S/cm. This is 2 orders of magnitude above the minimum value given by Huang et

al. This indicates that the transport through the GdO_xH_y electrolyte in our devices is relatively fast compared to the interface reactions. Even for a lower proton concentration (non-stoichiometric $Gd(OH)_3$, or perhaps partially hydrated Gd_2O_3 which could have a proton concentration several orders of magnitude lower than $Gd(OH)_3$), transport through the oxide should not be the limiting step.

This is higher than the conductivity value for YSZ, a known good proton conductor which has a room temperature conductivity around 10^{-4} S/cm. The high proton conductivity of YSZ is attributed to small grain size and the presence of physisorbed and chemisorbed water in the grain boundaries, as opposed to Grotthuss type proton conduction through the bulk.[91] Given the 5-10 nm grain size in the RF sputtered GdO_xH_y, it is not unreasonable that proton conduction in our films uses a similar mechanism, which would explain why the conductivity is so much higher than that found for bulk Gd_2O_3[37]. Dr. Sunho Kim's work on proton conduction in gadolinia supports this finding for textured columnar gadolinia deposited by pulsed laser deposition[73]. He found through TGA measurements that above 50°C, much of the water in our GdO_xH_y is driven out; however at room temperature, there is likely free water in grain boundaries and at interfaces.

Previous work in the group found a total GdO_x conductivity at room temperature between 10^{-12} and 10^{-11} S/cm, calculated by measuring the current as a function of temperature.[5] However, this is only a lower bound, since the contributions from the interface reactions and transport through the oxide were not separated. Our calculation of proton conductivity in this work does separate out the contributions of redox reactions at the interface and proton transport through the GdO_xH_y, and the much higher proton conductivity we find through these methods indicates that the previous measurement was dominated by the slower interface reactions. A j_0 value of 10^{-8} as calculated from the Tafel plot above would give an overall conductivity value of around 10^{-9} S/cm at 0.5 V, according to the following equation that calculates the conductivity from the differential resistance given by the Butler-Volmer equation (Equation 5.1):

$$\sigma(V) = j_0 L \left(\frac{zq(1-\alpha)}{k_B T} \right) \exp \left[\frac{zq(1-\alpha)V}{k_B T} \right] \tag{5.4}$$

. This is about 2 orders of magnitude higher than the previously calculated value of overall conductivity of 10^{-11} S/cm. It does not exactly match, but indicates that the device is interface-reaction limited rather than limited by proton transport through the oxide as previously assumed.

This is a somewhat surprising result, as these devices were previously assumed to be limited by the proton conductivity through the oxide. These results indicate that nanoscale devices are thin enough and the proton conductivity is high enough that, unlike typical microscale devices such as proton conducting fuel cells, the transport through the bulk oxide is not limiting device performance. The implication is that the interface reactions and availability of protons at the interface are more fruitful places to focus future attention. In particular, adding a proton storage layer (e.g. Pd) at the top electrode rather than relying on atmospheric water vapor could dramatically improve the device interface kinetics and lead to faster and more reliable property toggling. This would also allow for devices to be enclosed, and would therefore not rely on ambient relative humidity being high enough for the device to work.

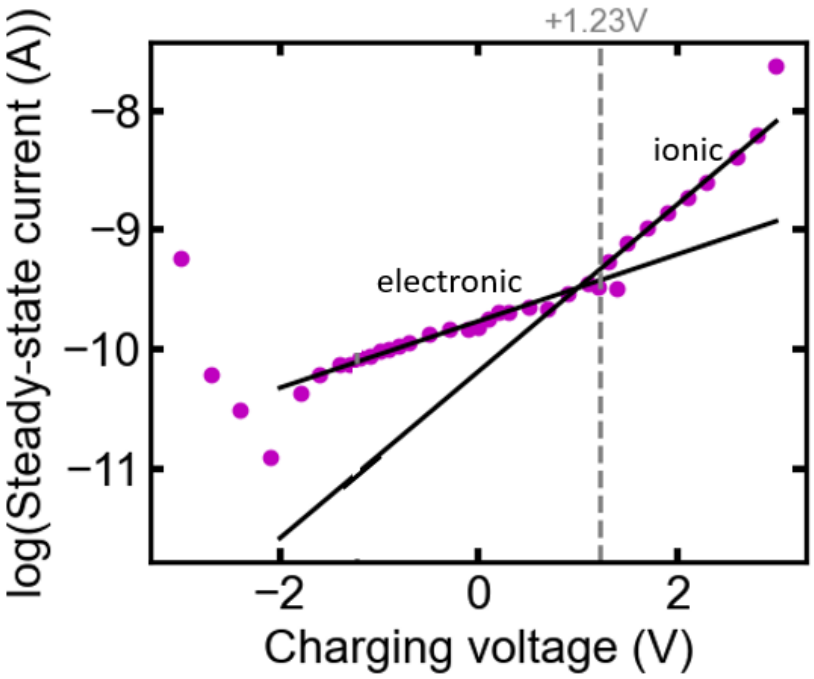

Figure 5-14: A Tafel plot (log of current vs. voltage) for a Pt/GdO_xH_y/Au device, with a linear fit for the ionic current.

Chapter 6

Magnetic switching in $Pd/GdCo/Pd/GdO_xH_y/Au$

6.1 Ferrimagnets and applications to magnetic memory

In previous sections, we have seen that voltage control of ions can be used to cause magnetic switching (specifically switching of magnetic anisotropy) in ferromagnets. We now turn to a slightly different type of magnetic material, ferrimagnets, and demonstrate that protons can also be used to toggle their properties. In magnetic memories, it is desirable to have bits with antiparallel magnetizations, for easier reading and less volatility. The changes in anisotropy in the ferromagnetic Co layer produced a 90° change rather than a 180° rotation of the magnetization. In a ferromagnet, the magnetic moments in their lowest energy state line up parallel to one another, and to rotate the magnetization of the film, all of the individual moments rotate together to preserve this ferromagnetic coupling. In a ferrimagnet, simliar to an antiferromagnet, there are two sublattices in the material with antiparallel moments. In an antiferromagnet, the up and down sublattices have equal moments that exactly cancel each other out, producing zero net moment in the material. In a ferrimagnet, the sublattices can have different moments which do not cancel out, leading

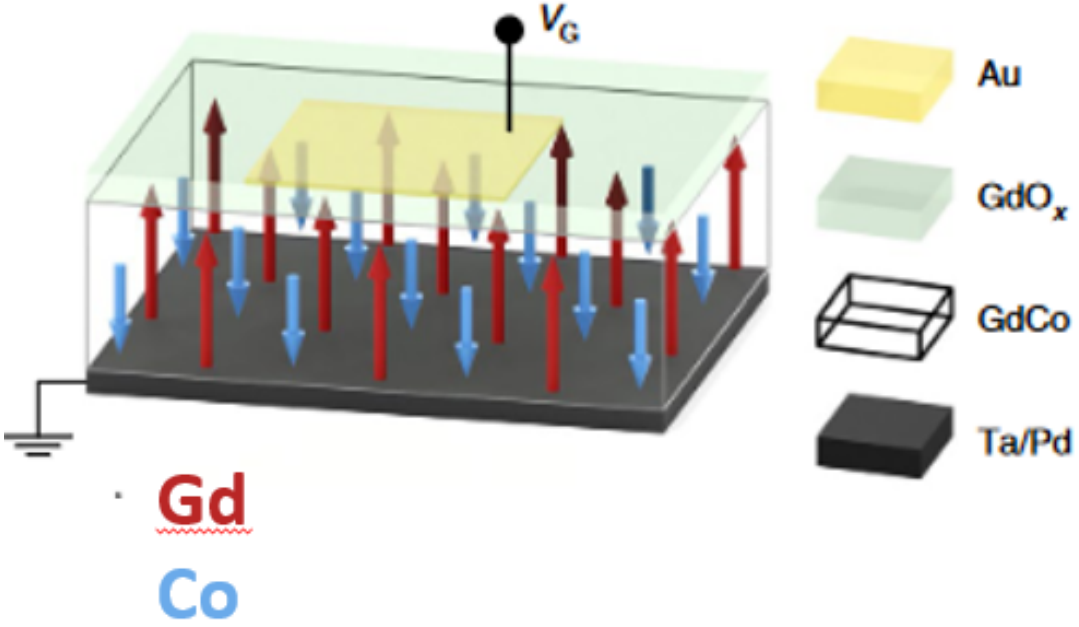

Figure 6-1: Schematic reprinted from Reference [12] showing the structure of GdCo. The red arrows are the Gd magnetic moments, and the blue arrows are the Co magnetic moments. The sublattices have antiparallel moments with different magnitudes, leading to a net magnetization in the material.

to a material with a relatively small net moment. This built-in structure of antiparallel moments lends itself to 180° switching of the net moment, if you can control the relative magnitudes of the moments on each sublattice.

This is exactly what we do with GdCo, a ferrimagnetic rare-earth transition-metal (RE-TM) amorphous alloy. In GdCo, there is a Gd sublattice (red arrows in Figure 6-1) and a Co sublattice (blue arrows) with antiparallel moments. Previously, we used x-ray magnetic circular dichroism to measure the individual sublattice moments before and after gating, finding that inserting hydrogen into GdCo disrupts the Gd-Co exchange coupling (J_{Gd-Co}), causing the Gd moment to shrink.[12]. For a GdCo layer that is Gd-dominated but close to compensation, shrinking the Gd moment pushes the film over the threshold and allows Co to dominate, causing an effective 180° rotation in net magnetization. Figure 6-2, from Reference [12], illustrates the proton gating of GdCo and the transition from Gd-dominated to Co-dominated magnetization.

This phenomenon also allows GdCo near compensation to be used as a relatively

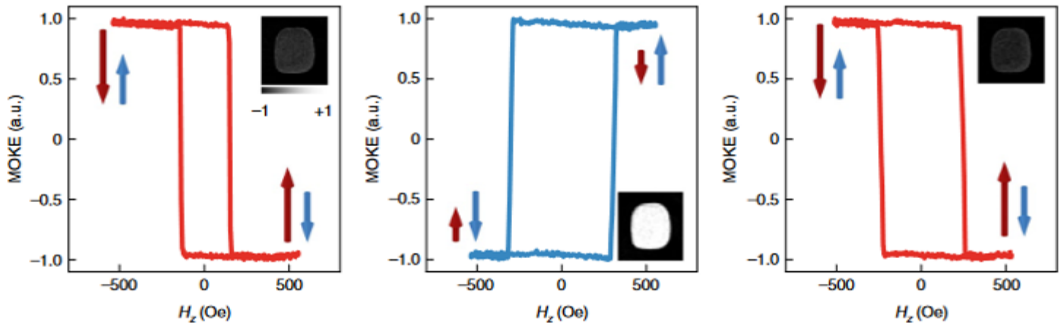

Figure 6-2: Figure reprinted from Reference [12] showing the MOKE hysteresis loops for GdCo starting in the Gd-dominated state, gating under positive voltage to the Co-dominated state, and then reverting to the Gd-dominated state upon application of a negative voltage. The red arrows denote the magnitude and orientation of the Gd sublattice moments, while the blue arrows denote the magnitude and orientation of the Co sublattice moments. Note that the MOKE loop tracks the Co sublattice, so that the MOKE loop is "positive" when the Co sublattice is dominating.

sensitive measure of the presence of hydrogen; effectively it is a magnetic sensor that allows us to determine whether or not hydrogen has reached the GdCo layer in the device stack. This gives some insight into the transport of protons through the electrolyte layer as compared to the GdCo layer itself.

6.2 Device description and sample fabrication

The samples used for the following experiments were Si/SiO2/Ta/Pd/GdCo/Pd/GdO_xH_y/Au. In this stack, the Ta/Pd/GdCo/Pd serves as the back electrode, GdCo is the ferrimagnetic layer, the Pd serves as a capping layer through with hydrogen can readily diffuse but oxygen cannot, the GdO_xH_y is the proton-conducting electrolyte, and the Au is the top electrode. The devices are crossbars with dimensions ranging from 10 um to 50 um.

The sample was sputtered at a background pressure of around $1 \times 10^{-}7$ mbar. The Ar pressure was 3.0 mbar. The GdCo was sputtered with a wedge mask to produce a gradient in composition, such that some devices would be guaranteed to be near compensation. The Gd current was 0.24 A and the Co current was 0.4 A. The Gd and Co were co-sputtered for 180 s to form an approximately 10 nm layer. The GdO_xH_y

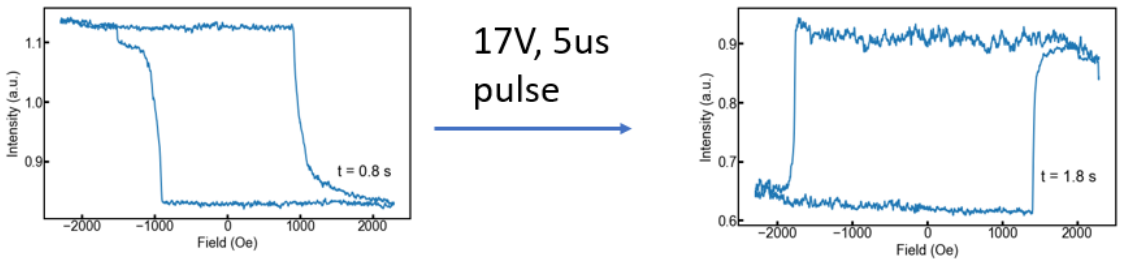

Figure 6-3: MOKE loops for a Ta 3nm/Pt 3nm/GdCo 6nm/Pd 6nm/GdO_xH_y 11nm/Au 3nm device to which a +17 V voltage pulse has been applied for 5 μs. The loop switches from a negative polarity loop (Gd-dominated case) to a positive polarity loop (Co-dominated).

layer was RF sputtered using a Gd_2O_3 target at 100 W with 0.7 mbar O_2 (flow rate of 9.8 sccm) and 3.0 mbar Ar (flow rate of 30 sccm).

6.3 Magnetic switching with voltage

6.3.1 Magneto-ionic switching of a ferrimagnet

First, we carried out voltage-step measurements (DC voltage application) to observe the evolution of the MOKE loop as the device switches from Gd-dominated to Co-dominated. Since the MOKE measurement is sensitive primarily to the Co magnetization, when the Co sublattice has the higher moment (and the Co moments are therefore tracking the externally applied field), the loop has the normal positive polarity (the measured magnetization is pointing in the direction of the applied field, so the loop has a high value at positive field and low value at negative field). When the Gd moments are greater than the Co, the Gd tracks with the applied field. However, the MOKE is still measuring the Co moment, which now points opposite to the applied field, giving a negative polarity or "backwards" MOKE loop. Figure 6-3 shows the switching of a Ta 3nm/Pt 3nm/GdCo 6nm/Pd 6nm/GdO_xH_y 11nm/Au 3nm device from the Gd-dominated state to the Co-dominated state.

6.3.2 Time scale for GdCo moment switching with voltage pulses

Next, we used short current pulses to investigate the magnetic response under different voltage and %RH conditions. These short pulses demonstrate the sensitivity of the GdCo magnetization to small amounts of hydrogen (small amounts of energy required to switch). We evaluate the voltage and RH ranges required to effectively switch the devices.

Because we are looking for the minimum pulse time required for any magnetic change in the GdCo in order to measure how long the hydrogen takes to get to the magnetic layer. Therefore, we do not need to inject enough hydrogen to change the GdCo magnetism from fully Gd-dominated to fully Co-dominated. Instead, we can look for small changes in coercivity. We look for an increase in coercivity for the Gd-dominated case, or a decrease in coercivity for the Co-dominated case, as the hydrogen injection effectively decreases the compensation temperature, moving the device effectively up the coercivity curve shown in Figure 6-4.[12]. Figure 6-5 shows an example of a voltage pulse causing a small change in the coercivity of the device. Figure 6-6 shows the summary of voltage pulse data for Ta 4 nm/Pd 6 nm/GdCo 8 nm/Pd 6 nm/GdO_xH_y 40 nm/Au 3 nm devices. Note that this plot aggregates data from around 20 devices, since the large voltages applied to the devices for too long could cause breakdown of the electrolyte, leading to shorting. Note also that this is a log-log plot. For different RH values, the RH was allowed to equilibrate for 3-5 minutes at a given value before pulsed measurements were taken.

The plot gives a relationship of $\log \tau = -4.2 \log V + C$. For a device where hydrogen transport is mainly limited by transport across the electrolyte driven by the electric field, we would expect a relationship of $\tau = \frac{t^2 k_B T}{DqV}$, where t is the device thickness, q is the elementary charge, and V is the applied voltage across the electrolyte. The linear fit to the plot gives a relationship of $\tau \propto V^{-4.2}$ rather than the $\tau \propto V^{-1}$ relationship predicted by this calculation. The relationship also does not exactly fit the relationship expected if the redox reactions at the electrodes are limiting, which

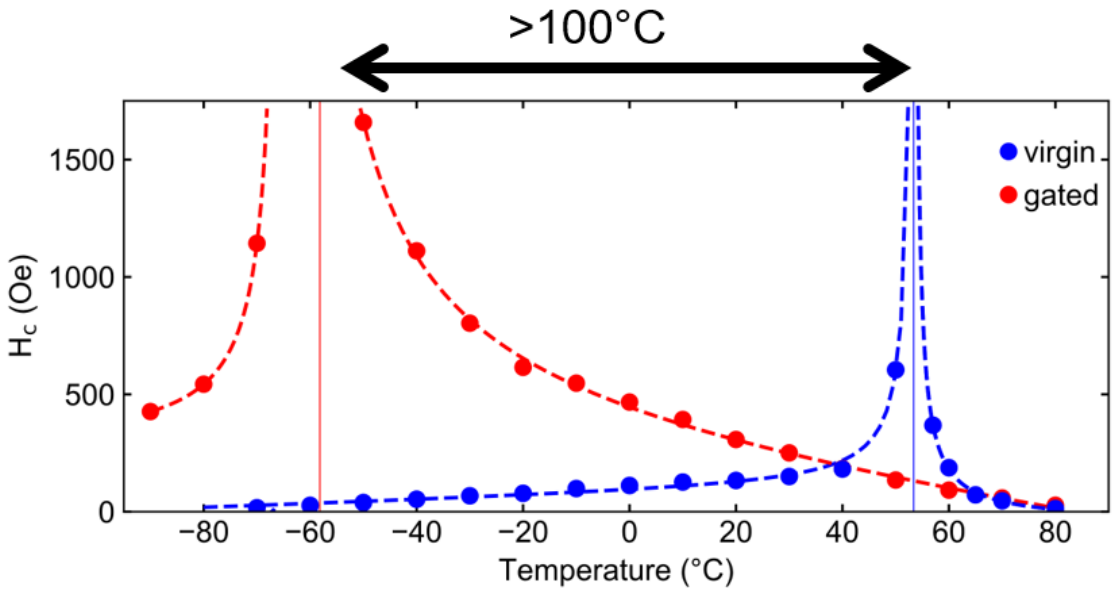

Figure 6-4: Coercivity of a GdCo film as a function of temperature, reproduced from Ref. [12]. Injecting hydrogen effectively reduces the compensation temperature by about 100 °C, moving the device from the blue curve to the red curve.

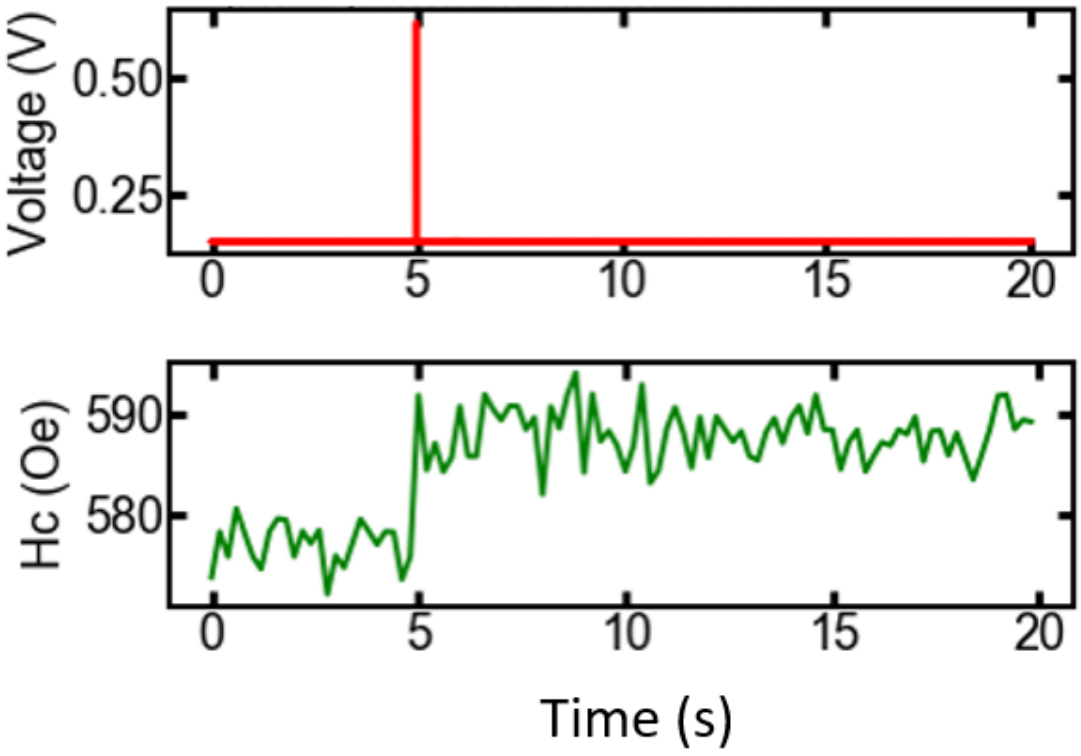

Figure 6-5: Voltage vs time and coercivity vs time for a voltage pulse applied to a Pd/GdCo/Pd/GdO_xH_y/Au device. After the 5 μs long voltage pulse at t=5 s, the coercivity of the GdCo increases by about 10 Oe.

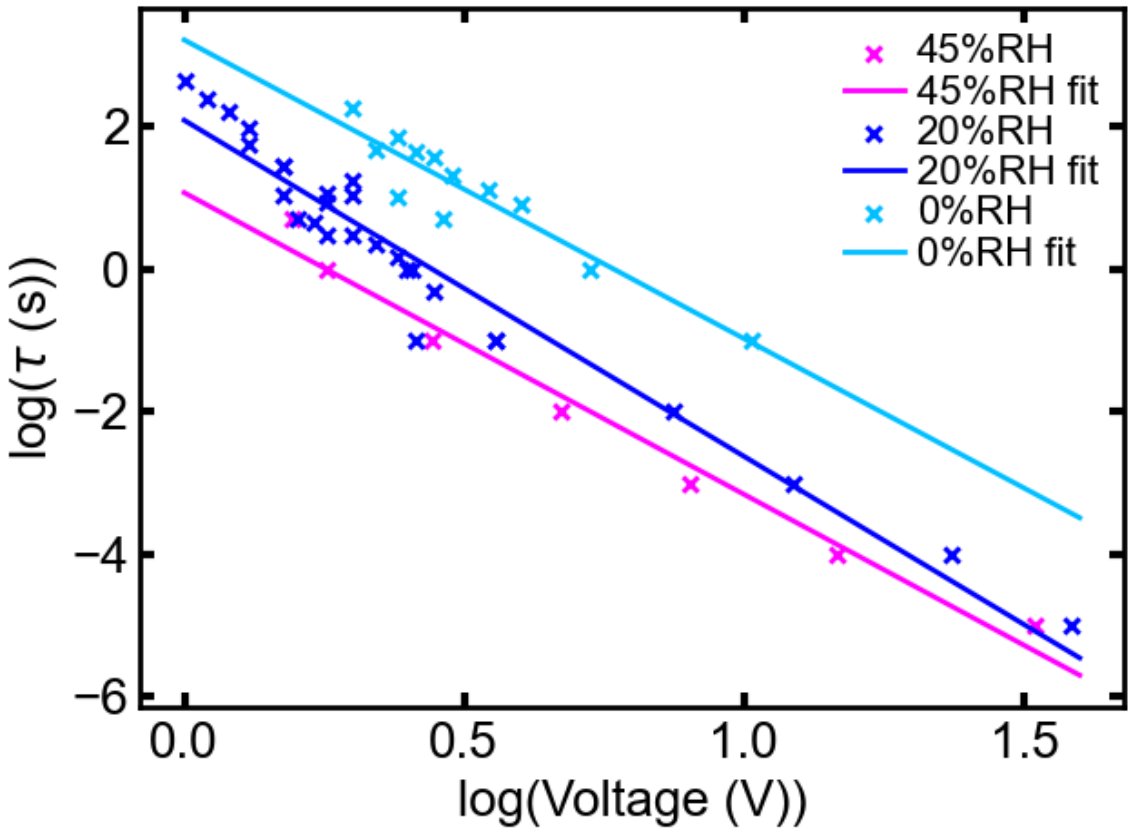

Figure 6-6: Log-log plot of τ (pulse time required to observe a coercivity change in the GdCo) as a function of pulse voltage. Several %RH values are plotted, showing that higher RH decreases the time required to switch the device. The voltage range is +0.8 V to +40 V.

would give $\tau \propto j^{-1} = j_0^{-1} \exp\left[-\frac{zq(1-\alpha)V}{k_B T}\right]$. The measured time to magnetic change is much more strongly dependent on voltage than expected. The voltage dependence predicted by interface reactions with Butler-Volmer kinetics is $\tau \propto \exp(V)$, which also does not fit this data. Likely, the assumptions made in predicting the $\tau \propto V^{-1}$ relationship and Butler-Volmer kinetics break down rapidly at high voltage. At higher voltages, the voltage is no longer limiting so the dependence on voltage falls off rapidly. Instead, it could be the amount of water in the air or in the oxide, the number of protonic defects, or electronic current dominating the total current (possibly due to reaching the dielectric breakdown voltage) that limits the amount of hydrogen put in and the speed at which it reaches the GdCo. While higher voltages are needed to get shorter and shorter pulse times for switching, the effect of increased voltage diminishes, which means that more and more energy is expended to reach switching at shorter pulse times.

The data for three %RH values (0, 20, 45) are shown. As expected, the switching gets faster for higher RH. This demonstrates that the protons that cause magnetic switching are being injected at the top electrode during the pulse and are not primarily protons that are already in the bulk of the oxide and are being driven from the middle of the electrolyte layer to the bottom interface during the voltage pulse. While the electrochemical data for the $Pt/GdO_xH_y/Au$ devices suggests that higher RH should continue to make the switching faster, the stochasticity of the electronic resistance state made it difficult to get more than a few data points at higher RH.

Given the results of the electrical and electrochemical characterization of the device in chapter 5, indicating that the proton conductivity through the bulk is not the limiting step in the transfer of hydrogen into the GdCo, we would expect that the thickness of the device should have little effect on the switching speed. Were the bulk transport limiting, we would expect a relationship of $\tau = \frac{t^2}{\mu V}$, where t is the oxide thickness. Figure 6-7 shows for two different values of relative humidity that the switching times for a 10 nm oxide film and a 40 nm oxide film are nearly identical. This corroborates the idea that these devices are limited by the interface reactions, not by transport through the oxide thickness.

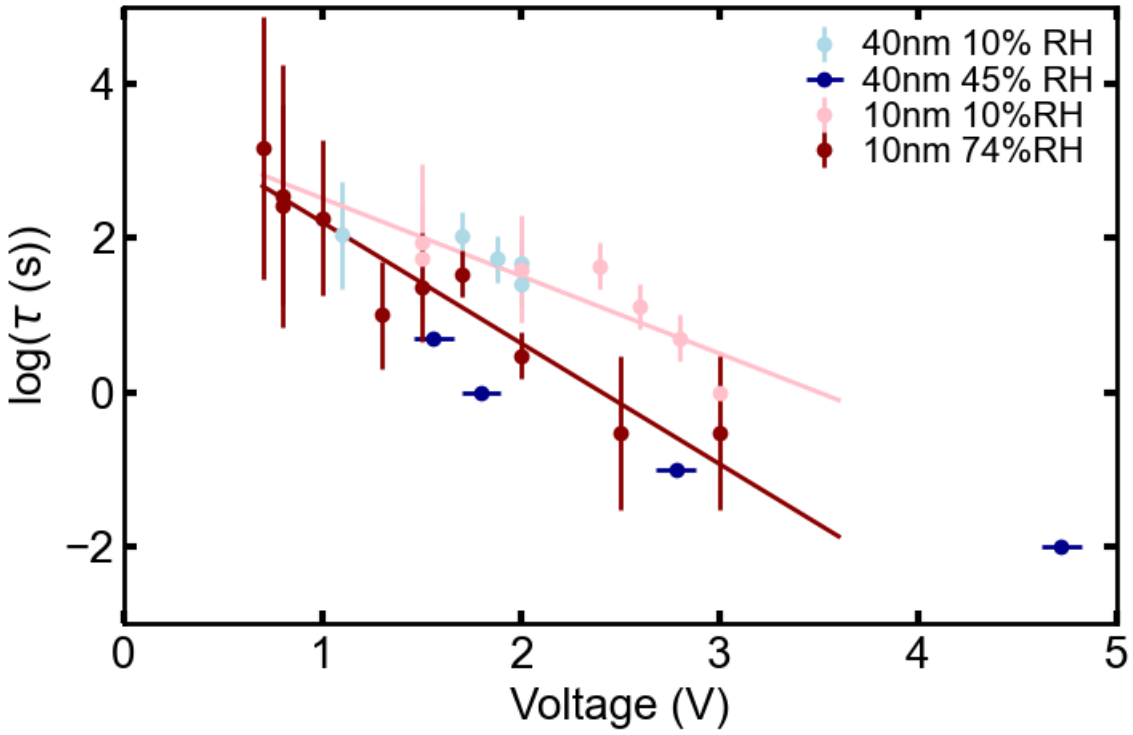

Figure 6-7: Log plot of τ (pulse time required to observe a coercivity change in the GdCo) as a function of pulse voltage. A high and a low %RH value curve is plotted for each device thickness, showing that higher %RH decreases the time required to switch the device. The high RH values are not the same due to the difficulty of obtaining very high %RH data on some devices (leading to stochastic switching of the resistance and inconsistent data).

6.4 Measuring hydrogen injected during voltage pulses

The amount of hydrogen required to induce a magnetic change in GdCo has not previously been estimated. The CV charge-counting measurements from chapter 5 allow us to estimate the protonic current flowing into the device during gating, which gives us a way to estimate the amount of hydrogen inserted into the device during gating of GdCo. This is a upper bound on the amount that enters the GdCo and causes the magnetic change, as some hydrogen may stay in the oxide or in the Pd capping layer after undergoing the reduction reaction at the bottom electrode.

To count the hydrogen injected during a pulse, we use the following equation:

$$N_H = \frac{if\tau}{qz} \tag{6.1}$$

where i is the current during the pulse, f is the fraction of the current that is protonic, q is the elementary charge, z is the number of electrons transferred per proton ($z = 1$), and τ is the pulse duration. For the devices shown in Figure 6-6, a typical low-voltage switching event at 20 %RH is a $\tau = 0.1$ s pulse at +3 V. The device current at +3 V is around 4 nA, and we assume based on our charge integration analysis from section 5.3.2 that 75% of the current in this case is protonic, leading to a protonic current of 3 nA, or a protonic current density of 1.2×10^{-4} A/cm^2. Applying this current for 0.1 s gives a hydrogen density of 7.5×10^{13} H/cm^2 at the bottom interface, or a total amount of 1.9×10^9 hydrogen atoms. The switching event in a Ta 3nm/Pt 3nm/GdCo 6nm/Pd 6nm/GdO_xH_y 11nm/Au 3nm device shown in Figure 6-3 was done at +17 V (for which we estimate a current of 100 μA and f=0.5) and has a switching pulse time of 5 μs, giving a total H count of 1.6×10^9 hydrogen atoms. This is remarkably consistent with the number we just calculated for the lower voltage pulse, although it should be noted that a similar calculation for the rest of the switching events in Figure 6-6 would not all give such close calculations, as the τ values for higher voltages are a few orders of magnitude above the +17 V, 5 μs switching event. Density functional theory (DFT) simulations done by Konstantin Klyukin indicate that in $GdCo_2$, the Gd moment is reduced in $GdCo_2H$ and the dominant lattice reverses at

$GdCo_2H_2$[12] The density of $GdCo_2$ is approximately 8.3 g/cm^3, which gives a density of 1.8×10^{22} Gd/cm^3 and 3.6×10^{22} Co/cm^3. This gives a surface or interface density of about 4×10^{12} Gd/cm^2 assuming a layer thickness of 220 pm. Assuming all injected H is at the interface, this gives a projected H:$GdCo_2$ ratio of 20:1. This is not a very reasonable assumption; it would be more reasonable to expect that only about 10% of the H makes it to the GdCo, which would match with the projected composition of $GdCo_2H_2$ for full switching. If we assume all the injected H diffuses uniformly throughout the 10 nm GdCo layer, we get a composition of $GdCo_2H_0.005$, which is several orders of magnitude less than the composition predicted by DFT. Uniform composition is probably also not a reasonable assumption; the real H distribution is most likely somewhere in between. Considering that the pulsed measurements were measuring small changes in coercivity, not full switching from Gd- to Co-dominated states, the DFT simulation projects that the composition should be $GdCo_2H$. The amount of injected hydrogen calculated here is a fairly wide range, but this range is reasonably in line with the H density of $GdCo_2H$ predicted for magnetic switching by DFT calculations.

Chapter 7

Conclusion

7.1 Summary

We made significant progress on understanding the structure and properties of GdO_xH_y and how they impact the operation of magneto-ionic devices.

First, we investigated the hydration process in a stand-alone GdO_xH_y film. We observed the hydration with a technique that allows for direct measurement of the hydrogen depth profile (neutron reflectometry) for the first time. SIMS measurements served to confirm the presence of GdO_xH_y ions in the device. We also used NR to observe the reversibility of the hydration process with vacuum annealing. We confirmed the differences in structure between reactively sputtered and RF sputtered GdO_xH_y. We confirmed the previous finding that reactively sputtered GdO_xH_y starts as Gd_2O_3 and undergoes a phase transformation to $Gd(OH)_3$ starting from the top surface when exposed to sufficiently high RH conditions. We discovered using XRR and XRD that RF sputtered oxide starts as $Gd(OH)_3$, explaining researchers' observation that RF oxide did not need to be hydrated before the devices worked.

We made progress in understanding the chemistry of the $Pt/Co/GdO_xH_y/Au$ device, finding with PNR that the Co layer is actually a mix of Co, CoO, and CoO_xH_y phases. This was confirmed with SIMS. The PNR also revealed that the $Pt/Co/GdO_xH_y$ interface is possibly intermixed, resulting in a suppressed Co magnetization.

In order to investigate the electrical and electrochemical properties of the GdO_xH_y, we used $Pt/GdO_xH_y/Au$ devices without a magnetic layer and without hydrogen-storing Pd. This simplified the stack so we could focus on the properties of the GdO_xH_y and the interface reactions. We measured a value for the proton diffusivity in GdO_xH_y for the first time, finding a value of $D = 2.07 \times 10^{-}7$ cm^2/s. This led to a proton conductivity value of σ_0 10^{-2} S/cm, which was much higher than the lower bound previously estimated. A low reaction current value of j_0 10^{-8} A/cm^2 led us to conclude that the device kinetics are limited by the interface redox reactions, not the proton conductivity. This is a significant development, as it was previously assumed that the room temperature proton conductivity would limit device speeds, and that improving the proton conductor would lead to the most device improvement. We demonstrated that the device can switch between low-resistance state (high electronic conductivity) and a high-resistance state (low electronic conductivity, dominated by protonic current). As expected, we found that in the low-resistance state, the current is insensitive to changes in RH, and in a high-resistance state, the current is sensitive to RH. This suggests that the water splitting reaction at the top electrode is likely the limiting reaction, as this is the reaction that depends on RH.

We introduced a novel method of measuring protonic current during device discharging, based on cyclic voltammetry. This allows for measurement of stored charge without interference from the electronic current.

We additionally found that protons and hydrogen are stored not just in the device volume, but also in the GdO_xH_y and Pd layers. The measured charge storage capacity of the $Pt/GdO_xH_y/Au$ devices levels off between 5 and 20 minutes of charging. This is because for a fixed discharge time, only protons within a fixed radius can diffuse back to the electrode to be counted during discharge. The large H capacity of Pd explains the apparently infinite charge storage capacity of the Pd devices. This realization allowed us to separate the phenomena of drift transport under the device electrode and diffusion in the GdO_xH_y outside the electrode area, making a diffusivity calculation possible. Device capacity measurements at low charging times allowed us to estimate the proportion of current that is protonic as opposed to electronic.

We used a GdCo ferrimagnetic layer as a magnetic sensor to probe the device kinetics and determine the switching time of the device for different voltage and RH conditions. We found a very strong voltage dependence ($\tau \propto V^{-4.2}$) that is much higher than would be predicted by interface reactions with Butler-Volmer kinetics ($\tau \propto \exp(V)$) or by a process limited by the transport through the GdO_xH_y electrolyte ($\tau \propto V^{-1}$). We confirmed using two different GdO_xH_y layer thicknesses that the thickness does not significantly impact the switching time, confirming that the transport through the GdO_xH_y is relatively fast compared to other processes. We used the understanding of proton transport and hydrogen storage gained from the $Pt/GdO_xH_y/Au$ device studies to estimate the amount of hydrogen injected during a pulsed switching event, finding that it is consistent with previous DFT measurements on similar GdCo devices.

7.2 Future directions

7.2.1 Proton storage layer

All the devices described in this work use protons from the water vapor in the air and rely on either the addition of water into the oxide during the hydration phase transformation or the water splitting reaction at the top electrode during gating to incorporate the protons into the GdO_xH_y. This was a convenient way to source sufficient protons for device operation, and to easily control the concentration of water in the reservoir (control the RH) for experimental determination of the oxide properties, the chemistry of the redox reactions with the Co magnetic layer, and the required operating conditions for the device. However, this thesis has shown that this reaction is likely the limiting step in the proton's path from the reservoir to the magnetic layer or other property-switching layer of interest. Moreover, using water sourced from ambient humidity was never a viable option for a commercial implementation of these devices, since it is not acceptable for operation to vary with environmental humidity.

Palladium could be a candidate for a hydrogen storage layer due to its high hydrogen solubility and diffusivity. Alternatively, a hydrogen storage layers like WO_3 (implemented, for example, in the electrochemical ionic synapses upon which the device modeling in this thesis is based) would be a reasonable solution.[11]

7.2.2 Diffusivity measurements

The simple crossbar device structure used throughout this work could be used to measure the proton diffusivity in other ceramic materials in a similar manner to the calculation done in section 5.3.1.

7.2.3 Understanding magnetic switching chemistry

We made progress in understanding the chemistry of the Pt/Co/GdO_xH_y/Au device, finding with PNR that the Co layer is actually a mix of Co, CoO, and CoO_xH_y phases. However, we have not investigated whether or not some of the redox reactions that produce these phases could be selected for or suppressed, and we have not studied how these mixed phases might influence the kinetics of the interface reactions (either oxidation or reduction of Co, or incorporation of H at the Co/GdO_xH_y interface to produce the magnetic reorientation transition to an in-plane state).

In the GdCo devices, we have used our new understanding of hydrogen injection to estimate the amount of H that causes the magnetic switching. However, we still do not know for sure how much H is involved or where it goes (Pd/GdCo interface or GdCo bulk). Further PNR studies could be useful in investigating this, as PNR is very sensitive to H and to the net magnetization of the sample (with the caveat that it measures only the in-plane magnetization; therefore PMA GdCo devices would need to have a sufficiently strong in-plane field to drive the magnetization in-plane).

Bibliography

[1] Mariya Ivanova, S Ricote, S Baumann, W A Meulenberg, F Tietz, Jose Serra, and Hannes Richter. Ceramic Materials For Energy and Environmental Applications: Functionalizing of Properties by Tailored Compositions. In *Doping: Properties, Mechanisms and Applications*, pages 221–276. 4 2013.

[2] Yngve Larring and Truls Norby. Protons in rare earth oxides. *Solid State Ionics*, 77(C):147–151, 1995.

[3] Mona Shirpour, Giuliano Gregori, Rotraut Merkle, and Joachim Maier. On the proton conductivity in pure and gadolinium doped nanocrystalline cerium oxide. *Physical Chemistry Chemical Physics*, 13(3):937–940, 2011.

[4] Aik Jun Tan, Mantao Huang, Can Onur Avci, Felix Büttner, Maxwell Mann, Wen Hu, Claudio Mazzoli, Stuart Wilkins, Harry L. Tuller, and Geoffrey S.D. Beach. Magneto-ionic control of magnetism using a solid-state proton pump. *Nature Materials*, 18(1):35–41, 2019.

[5] Aik Jun Tan. *Dynamic Modulation of Material Properties by Solid State Proton Gating*. PhD thesis, MIT, 2019.

[6] Mantao Huang, Aik Jun Tan, Felix Büttner, Hailong Liu, Qifeng Ruan, Wen Hu, Claudio Mazzoli, Stuart Wilkins, Chuanhua Duan, Joel K.W. Yang, and Geoffrey S.D. Beach. Voltage-gated optics and plasmonics enabled by solid-state proton pumping. *Nature Communications*, 10(1):1–8, 2019.

[7] Dmitri Kalaev, Harry L. Tuller, and Ilan Riess. Measuring ionic mobility in mixed-ionic-electronic-conducting nano-dimensioned thin films at near ambient temperatures. *Solid State Ionics*, 319:291–295, 6 2018.

[8] Dmitri Kalaev, Thomas Defferriere, Clement Nicollet, Tamar Kadosh, and Harry L. Tuller. Dynamic Current–Voltage Analysis of Oxygen Vacancy Mobility in Praseodymium-Doped Ceria over Wide Temperature Limits. *Advanced Functional Materials*, 30(11):1–13, 2020.

[9] Uwe Bauer. *Voltage Programmable Materials*. PhD thesis, 2009.

[10] Aik Jun Tan, Mantao Huang, Sara Sheffels, Felix Büttner, Sunho Kim, Adrian H. Hunt, Iradwikanari Waluyo, Harry L. Tuller, and Geoffrey S.D. Beach. Hydration

of gadolinium oxide (Gd Ox) and its effect on voltage-induced Co oxidation in a Pt/Co/Gd Ox/Au heterostructure. *Physical Review Materials*, 3(6):1–8, 2019.

[11] Mantao Huang, Miranda Schwacke, Murat Onen, Jesus del Alamo, Ju Li, and Bilge Yildiz. Electrochemical Ionic Synapses: Progress and Perspectives. *Advanced Materials*, 2022.

[12] Mantao Huang, Muhammad Usama Hasan, Konstantin Klyukin, Delin Zhang, Deyuan Lyu, Pierluigi Gargiani, Manuel Valvidares, Sara Sheffels, Alexandra Churikova, Felix Büttner, Jonas Zehner, Lucas Caretta, Ki Young Lee, Joonyeon Chang, Jian Ping Wang, Karin Leistner, Bilge Yildiz, and Geoffrey S.D. Beach. Voltage control of ferrimagnetic order and voltage-assisted writing of ferrimagnetic spin textures. *Nature Nanotechnology*, 16(9):981–988, 2021.

[13] Tohru Tsuruoka, Kazuya Terabe, Tsuyoshi Hasegawa, Ilia Valov, Rainer Waser, and Masakazu Aono. Effects of moisture on the switching characteristics of oxide-based, gapless-type atomic switches. *Advanced Functional Materials*, 22(1):70–77, 2012.

[14] I. Valov, E. Linn, S. Tappertzhofen, S. Schmelzer, J. Van Den Hurk, F. Lentz, and R. Waser. Nanobatteries in redox-based resistive switches require extension of memristor theory. *Nature Communications*, 4:1771–1779, 2013.

[15] Mantao Huang, Aik Jun Tan, Maxwell Mann, Uwe Bauer, Raoul Ouedraogo, and Geoffrey S D Beach. Three-terminal resistive switch based on metal / metal oxide redox reactions. *Scientific Reports*, (June):1–7, 2017.

[16] Michael Lübben, Stefan Wiefels, Rainer Waser, and Ilia Valov. Processes and Effects of Oxygen and Moisture in Resistively Switching TaOx and HfOx. *Advanced Electronic Materials*, 4(1):1–11, 2018.

[17] Uwe Bauer, Lide Yao, Aik Jun Tan, Parnika Agrawal, Satoru Emori, Harry L. Tuller, Sebastiaan Van Dijken, and Geoffrey S.D. Beach. Magneto-ionic control of interfacial magnetism. *Nature Materials*, 14(2):174–181, 2015.

[18] Uwe Bauer, Satoru Emori, and Geoffrey S.D. Beach. Voltage-controlled domain wall traps in ferromagnetic nanowires. *Nature Nanotechnology*, 8(6):411–416, 2013.

[19] M Nichterwitz, S Honnali, M Kutuzau, S Guo, J Zehner, K Nielsch, and K Leistner. Advances in magneto-ionic materials and perspectives for their application. *APL Materials*, 030903(February), 2021.

[20] Dustin A Gilbert, Justin Olamit, Randy K Dumas, B J Kirby, Alexander J Grutter, Brian B Maranville, Elke Arenholz, Julie A Borchers, and Kai Liu. Controllable positive exchange bias via redox-driven oxygen migration. *Nature Communications*, 7:1–8, 2016.

[21] Nianpeng Lu, Pengfei Zhang, Qinghua Zhang, Ruimin Qiao, Qing He, Hao Bo Li, Yujia Wang, Jingwen Guo, Ding Zhang, Zheng Duan, Zhuolu Li, Meng Wang, Shuzhen Yang, Mingzhe Yan, Elke Arenholz, Shuyun Zhou, Wanli Yang, Lin Gu, Ce Wen Nan, Jian Wu, Yoshinori Tokura, and Pu Yu. Electric-field control of tri-state phase transformation with a selective dual-ion switch. *Nature*, 546(7656):124–128, 2017.

[22] Subho Dasgupta, Bijoy Das, Qiang Li, Di Wang, Tessy T. Baby, Sylvio Indris, Michael Knapp, Helmut Ehrenberg, Karin Fink, Robert Kruk, and Horst Hahn. Toward On-and-Off Magnetism: Reversible Electrochemistry to Control Magnetic Phase Transitions in Spinel Ferrites. *Advanced Functional Materials*, 26(41):7507–7515, 2016.

[23] Ki Young Lee, Sujin Jo, Aik Jun Tan, Mantao Huang, Dongwon Choi, Jung Hoon Park, Ho Il Ji, Ji Won Son, Joonyeon Chang, Geoffrey S.D. Beach, and Seonghoon Woo. Fast magneto-ionic switching of interface anisotropy using yttria-stabilized zirconia gate oxide. *Nano Letters*, 20(5):3435–3441, 2020.

[24] Julius de Rojas, Alberto Quintana, Aitor Lopeandía, Joaquín Salguero, Beatriz Muñiz, Fatima Ibrahim, Mairbek Chshiev, Aliona Nicolenco, Maciej O Liedke, Maik Butterling, Andreas Wagner, Veronica Sireus, Llibertat Abad, Christopher J Jensen, Kai Liu, Josep Nogués, José L. Costa-Krämer, Enric Menéndez, and Jordi Sort. Voltage-driven motion of nitrogen ions: a new paradigm for magneto-ionics. *Nature Communications*, 11(1), 2020.

[25] Chong Bi, Yaohua Liu, T. Newhouse-Illige, M. Xu, M. Rosales, J. W. Freeland, Oleg Mryasov, Shufeng Zhang, S. G.E. Te Velthuis, and W. G. Wang. Reversible control of Co magnetism by voltage-induced oxidation. *Physical Review Letters*, 113(26):1–5, 2014.

[26] Guanhua Hao, Nicholas Noviasky, Shi Cao, Ildar Sabirianov, Yuewei Yin, Carolina C Ilie, Eugene Kirianov, Nishtha Sharma, Andrei Sokolov, Andrew Marshall, Xiaoshan Xu, and Peter A Dowben. Some device implications of voltage controlled magnetic anisotropy in Co/Gd2O3 thin films through REDOX chemistry. *Journal of Magnetism and Magnetic Materials*, 451:487–492, 2018.

[27] Masako Sakamaki and Kenta Amemiya. Observation of an electric field-induced interface redox reaction and magnetic modification in GdOx/Co thin film by means of depth-resolved X-ray absorption spectroscopy. *Physical Chemistry Chemical Physics*, 20(30):20004–20009, 2018.

[28] J Zehner, D Wolf, M U Hasan, M Huang, D Bono, K Nielsch, K Leistner, and G. S.D. Beach. Magnetoionic control of perpendicular exchange bias. *Physical Review Materials*, 5(6):1–8, 2021.

[29] Satoru Emori, Uwe Bauer, Seonghoon Woo, and Geoffrey S.D. Beach. Large voltage-induced modification of spin-orbit torques in Pt/Co/GdOx. *Applied Physics Letters*, 105(22):3–6, 2014.

[30] Rahul Mishra, Farzad Mahfouzi, Dushyant Kumar, Kaiming Cai, Mengji Chen, Xuepeng Qiu, Nicholas Kioussis, and Hyunsoo Yang. Electric-field control of spin accumulation direction for spin-orbit torques. *Nature Communications*, 10(1):1–8, 2019.

[31] Yu Chen, Aliona Nicolenco, Pau Molet, Agustin Mihi, Eva Pellicer, Jordi Sort, Yu Chen, Agustin Mihi, and Eva Pellicer. Magneto-ionic suppression of magnetic vortices. *Science and Technology of Advanced Materials*, 22(1):972–984, 2021.

[32] Aurélien Manchon, Clarisse Ducruet, Lucien Lombard, Stéphane Auffret, Bernard Rodmacq, Bernard Dieny, Stefania Pizzini, Jan Vogel, Vojtech Uhlir, Michael Hochstrasser, Aurélien Manchon, Clarisse Ducruet, Lucien Lombard, Stéphane Auffret, and Bernard Rodmacq. Analysis of anisotropy crossover due to oxygen in Pt / Co / MOx trilayer. *J Applied Physics*, 104(4):043914, 2008.

[33] Tohru Tsuruoka, Ilia Valov, Cedric Mannequin, Tsuyoshi Hasegawa, Rainer Waser, and Masakazu Aono. Humidity effects on the redox reactions and ionic transport in a Cu/Ta 2 O 5 /Pt atomic switch structure. *Japanese Journal of Applied Physics*, 55(6S1):06GJ09, 2016.

[34] Felix Messerschmitt, Markus Kubicek, and Jennifer L.M. Rupp. How Does Moisture Affect the Physical Property of Memristance for Anionic-Electronic Resistive Switching Memories? *Advanced Functional Materials*, 25(32):5117–5125, 2015.

[35] Felix Messerschmitt, Maximilian Jansen, and Jennifer L.M. Rupp. When Memristance Crosses the Path with Humidity Sensing—About the Importance of Protons and Its Opportunities in Valence Change Memristors. *Advanced Electronic Materials*, 4(12):1–10, 2018.

[36] Hao Bo Li, Nianpeng Lu, Qinghua Zhang, Yujia Wang, Deqiang Feng, Tianzhe Chen, Shuzhen Yang, Zheng Duan, Zhuolu Li, Yujun Shi, Weichao Wang, Wei Hua Wang, Kui Jin, Hui Liu, Jing Ma, Lin Gu, Cewen Nan, and Pu Yu. Electric-field control of ferromagnetism through oxygen ion gating. *Nature Communications*, 8(1), 12 2017.

[37] Truls Norbya. Proton conduction in oxides. *Solid State Ionics*, 40-41(PART 2):857–862, 1990.

[38] Yuxing Wang, Bo Liu, Qiuyan Li, Samuel Cartmell, Seth Ferrara, Zhiqun Daniel Deng, and Jie Xiao. Lithium and lithium ion batteries for applications in microelectronic devices: A review, 7 2015.

[39] R. Janski, M. Fugger, M. Forster, M. Sorger, A. Dunst, I. Hanzu, M. Sternad, and M. Wilkening. Lithium barrier materials for on-chip Si-based microbatteries. *Journal of Materials Science: Materials in Electronics*, 28(19):14605–14614, 10 2017.

[40] Harry L Tuller and Sean R Bishop. Point defects in oxides: Tailoring materials through defect engineering. *Annual Review of Materials Research*, 41:369–398, 2011.

[41] Neelima Mahato, Amitava Banerjee, Alka Gupta, Shobit Omar, and Kantesh Balani. Progress in material selection for solid oxide fuel cell technology: A review, 7 2015.

[42] Saddam Hussain and Li Yangping. Review of solid oxide fuel cell materials: cathode, anode, and electrolyte. *Energy Transitions*, 4(2):113–126, 12 2020.

[43] B C H Steele. Oxygen ion conductors and their technological applications. *Materials Science and Engineering: B*, 13(2):79–87, 1992.

[44] A. J. Grutter, D. A. Gilbert, U. S. Alaan, E. Arenholz, B. B. Maranville, J. A. Borchers, Y. Suzuki, Kai Liu, and B. J. Kirby. Reversible control of magnetism in La0.67Sr0.33MnO3 through chemically-induced oxygen migration. *Applied Physics Letters*, 108(8), 2 2016.

[45] Truls Norby, Marius Widerøe, Ronny Glöckner, and Yngve Larring. Hydrogen in oxides. *Dalton Transactions*, (19):3012–3018, 2004.

[46] K. D. Kreuer. Proton-Conducting Oxides. *Annual Review of Materials Research*, 33(2):333–359, 2003.

[47] Therald Moeller and Howard E Kremers. The Basicity Characteristics of Scandium, Yttrium, and the Rare Earth Elements. *Chemical Reviews*, 37(1):97–159, 1945.

[48] Sanghun Jeon and Hyunsang Hwang. Effect of hygroscopic nature on the electrical characteristics of lanthanide oxides (Pr2O3, Sm2O3, Gd2O3, and Dy2O3). *Journal of Applied Physics*, 93(10 1):6393–6395, 2003.

[49] Truls Norby. Solid-state protonic conductors: principles, properties, progress and prospects. *Solid State Ionics*, 125(1):1–11, 1999.

[50] Takeo Miyake and Marco Rolandi. Grotthuss mechanisms: from proton transport in proton wires to bioprotonic devices. *Journal of Physics: Condensed Matter*, 28(2):23001, 12 2015.

[51] Klaus-Dieter Kreuer. Proton Conductivity: Materials and Applications. *Chemistry of Materials*, 8(3):610–641, 1996.

[52] Ilia Valov and Wei D Lu. Nanoscale electrochemistry using dielectric thin films as solid electrolytes. *Nanoscale*, 8(29):13828–13837, 2016.

[53] J. E. Bauerle. Study of solid electrolyte polarization by a complex admittance method. *Journal of Physics and Chemistry of Solids*, 30(12):2657–2670, 1969.

[54] Wei Wang, Dmitry Medvedev, and Zongping Shao. Gas Humidification Impact on the Properties and Performance of Perovskite-Type Functional Materials in Proton-Conducting Solid Oxide Cells. *Advanced Functional Materials*, 28(48):1802592, 2018.

[55] Pooja Sawant, S Varma, B N Wani, and S R Bharadwaj. Synthesis, stability and conductivity of BaCe0.8xZrxY0.2O3δ as electrolyte for proton conducting SOFC. *International Journal of Hydrogen Energy*, 37(4):3848–3856, 2012.

[56] Donglin Han, Masatoshi Majima, and Tetsuya Uda. Structure analysis of BaCe0.8Y0.2O3δ in dry and wet atmospheres by high-temperature X-ray diffraction measurement. *Journal of Solid State Chemistry*, 205:122–128, 2013.

[57] Shaojing Yang, Yabing Wen, Sanpei Zhang, Sui Gu, Zhaoyin Wen, and Xiaofeng Ye. Performance and stability of BaCe0.8xZr0.2InxO3δ-based materials and reversible solid oxide cells working at intermediate temperature. *International Journal of Hydrogen Energy*, 42(47):28549–28558, 2017.

[58] T Seiyama, N Yamazoe, and H Arai. Ceramic humidity sensors. *Sensors and Actuators*, 4:85–96, 1983.

[59] Chuancheng Duan, Jianhua Tong, Meng Shang, Stefan Nikodemski, Michael Sanders, Sandrine Ricote, Ali Almansoori, and Ryan O'Hayre. Readily processed protonic ceramic fuel cells with high performance at low temperatures. *Science*, 349(6254):1321–1326, 2015.

[60] Emiliana Fabbri, Daniele Pergolesi, and Enrico Traversa. Materials challenges toward proton-conducting oxide fuel cells: a critical review. *Chem. Soc. Rev.*, 39(11):4355–4369, 2010.

[61] Qiyang Lu, Sean R Bishop, Dongkyu Lee, Shinbuhm Lee, Hendrik Bluhm, Harry L Tuller, Ho Nyung Lee, and Bilge Yildiz. Electrochemically Triggered Metal–Insulator Transition between VO2 and V2O5. *Advanced Functional Materials*, 28(34):1803024, 2018.

[62] Jeff Walter, Helin Wang, Bing Luo, C Daniel Frisbie, and Chris Leighton. Electrostatic versus Electrochemical Doping and Control of Ferromagnetism in Ion-Gel-Gated Ultrathin La0.5Sr0.5CoO3δ. *ACS Nano*, 10(8):7799–7810, 2016.

[63] X. Leng, J. Pereiro, J. Strle, G. Dubuis, A. T. Bollinger, A. Gozar, J. Wu, N. Litombe, C. Panagopoulos, D. Pavuna, and I. Božović. Insulator to metal transition in WO3 induced by electrolyte gating. *npj Quantum Materials*, 2(1), 12 2017.

[64] M Hamaguchi, K Aoyama, S Asanuma, Y Uesu, and T Katsufuji. Electric-field-induced resistance switching universally observed in transition-metal-oxide thin films. *Applied Physics Letters*, 88(14):142508, 4 2006.

[65] Yuan-Chang Yeh, Tseung-Yuen Tseng, and Deh-An Chang. Electrical Properties of Porous Titania Ceramic Humidity Sensors. *Journal of the American Ceramic Society*, 72(8):1472–1475, 8 1989.

[66] S G Ansari, Z A Ansari, M R Kadam, R N Karekar, and R C Aiyer. The effect of humidity on an SnO2 thick-film planar resistor. *Sensors and Actuators B: Chemical*, 21(3):159–163, 1994.

[67] Yuan He, Tong Zhang, Wei Zheng, Rui Wang, Xiangwei Liu, Yan Xia, and Jinwei Zhao. Humidity sensing properties of BaTiO3 nanofiber prepared via electrospinning. *Sensors and Actuators B: Chemical*, 146(1):98–102, 2010.

[68] Zhi David Chen and Chi-En Lu. Humidity Sensors: A Review of Materials and Mechanisms. *Sensor Letters*, 3:274–295, 2005.

[69] D Sander, W Pan, S Ouazi, J Kirschner, W Meyer, M Krause, S Müller, L Hammer, and K Heinz. Reversible H-Induced Switching of the Magnetic Easy Axis in $\mathrm{N}\mathrm{i}/\mathrm{C}\mathrm{u}(001)$ Thin Films. *Physical Review Letters*, 93(24):247203, 12 2004.

[70] K Munbodh, F Perez, Cameron Keenan, Mikhail Zhernenkov, M Fitzsimmon, and David Lederman. Effects of hydrogen/deuterium absorption on the magnetic properties of
}Co/Pd multilayers. *Phys. Rev. B*, 83, 2 2011.

[71] Takayoshi Katase, Takaki Onozato, Misako Hirono, Taku Mizuno, and Hiromichi Ohta. A transparent electrochromic metal-insulator switching device with three-terminal transistor geometry. *Scientific Reports*, 6(1):25819, 2016.

[72] Thomas Defferriere, Dmitri Kalaev, Jennifer L.M. Rupp, and Harry L. Tuller. Impact of Oxygen Non-Stoichiometry on Near-Ambient Temperature Ionic Mobility in Polaronic Mixed-Ionic-Electronic Conducting Thin Films. *Advanced Functional Materials*, 31(14):1–14, 2021.

[73] Sunho Kim. *Defect and Electrical Properties of High-κ Dielectric Gd2O3 for Magneto-Ionic and Memristive Memory Devices*. PhD thesis, MIT, 6 2020.

[74] Laura Mazzei, Max Wolff, Daniele Pergolesi, Joseph A. Dura, Lars Börjesson, Philipp Gutfreund, Marco Bettinelli, Thomas Lippert, and Maths Karlsson. Structure and conductivity of epitaxial thin films of in-doped BaZrO3-based proton conductors. *Journal of Physical Chemistry C*, 120(50):28415–28422, 2016.

[75] S. Sheffels, P. P. Balakrishnan, M. Huang, S. Muramoto, J. A. Borchers, J. A. Dura, A. J. Grutter, and G. S.D. Beach. Insight on hydrogen injection and GdOx/Co interface chemistry from in operando neutron reflectometry and secondary ion mass spectrometry. *Applied Physics Letters*, 122(2), 1 2023.

[76] Ramincheraghali and Mustafa Aghazadeh. A Simple and Facile Electrochemical Route to Synthesis of Metal Hydroxides and Oxides Ultrafine Nanoparticles (M=La, Gd, Ni and Co). *Analytical and Bioanalytical Electrochemistry*, 8:64–77, 5 2016.

[77] Kotaro Ogura, Shiro Haruyama, and Kyuya Nagasaki. The Electrochemical Oxidation and Reduction of Gold. *Journal of The Electrochemical Society*, 118(4):531, 1971.

[78] Takashi Miyazaki, Ray Hasegawa, Hajime Yamaguchi, Haruhi Oh-oka, Hitoshi Nagato, Isao Amemiya, and Shuichi Uchikoga. Electrical Control of Plasmon Resonance of Gold Nanoparticles Using Electrochemical Oxidation. *J Phys Chem C*, 113:8484–8490, 2009.

[79] Mengnan Wang, Jack Binns, Mary Ellen Donnelly, Miriam Peña-Alvarez, Philip Dalladay-Simpson, and Ross T. Howie. High pressure synthesis and stability of cobalt hydrides. *Journal of Chemical Physics*, 148(14):1–5, 2018.

[80] B. J. Sarkar, A. Bandyopadhyay, J. Mandal, A. K. Deb, and P. K. Chakrabarti. Paramagnetic to ferromagnetic phase transition of Co doped Gd2O3 prepared by chemical route. *Journal of Alloys and Compounds*, 656:339–346, 2016.

[81] F. Letellier, V. Baltz, L. Lechevallier, R. Lardé, J. F. Jacquot, B. Rodmacq, J. M. Le Breton, and B. Dieny. Effects of sputter-deposition-induced and post-deposition thermally activated intermixing on the exchange bias properties of [Pt/Co] $\times 3$/(Pt)/IrMn films. *Journal of Physics D: Applied Physics*, 45(27), 2012.

[82] Chih Chia Huang, Tzu Yu Liu, Chia Hao Su, Yi Wei Lo, Jyh Horng Chen, and Chen Sheng Yeh. Superparamagnetic hollow and paramagnetic porous Gd2O3 particles. *Chemistry of Materials*, 20(12):3840–3848, 2008.

[83] Steven C. DeCaluwe, Paul A. Kienzle, Pavan Bhargava, Andrew M. Baker, and Joseph A. Dura. Phase segregation of sulfonate groups in Nafion interface lamellae, quantified via neutron reflectometry fitting techniques for multi-layered structures. *Soft Matter*, 10(31):5763–5776, 2014.

[84] B. Maranville, W Ratcliff II, and P Kienzle. reductus: a stateless Python data reduction service with a browser front end. *Journal of Applied Crystallography*, 51:1500–1506, 2018.

[85] B. J. Kirby, P. A. Kienzle, B. B. Maranville, N. F. Berk, J. Krycka, F. Heinrich, and C. F. Majkrzak. Phase-sensitive specular neutron reflectometry for imaging the nanometer scale composition depth profile of thin-film materials. *Current Opinion in Colloid and Interface Science*, 17(1):44–53, 2012.

[86] C. F. Majkrzak, N. F. Berk, S. Krueger, J. A. Dura, M. Tarek, D. Tobias, V. Silin, C. W. Meuse, J. Woodward, and A. L. Plant. First-principles determination

of hybrid bilayer membrane structure by phase-sensitive neutron reflectometry. *Biophysical Journal*, 79(6):3330–3340, 12 2000.

[87] C. F. Majkrzak, N. F. Berk, V. Silin, and C. W. Meuse. Experimental demonstration of phase determination in neutron reflectometry by variation of the surrounding media. *Physica B: Condensed Matter*, 283(1-3):248–252, 6 2000.

[88] K. Zhernenkov, S. Klimko, B. P. Toperverg, and H. Zabel. AC-polarized neutron reflectometry: Application to domain dynamics in thin Fe film. *Journal of Physics: Conference Series*, 211, 2010.

[89] Charles F. Majkrzak, Christopher Metting, Brian B. Maranville, Joseph A. Dura, Sushil Satija, Terrence Udovic, and Norman F. Berk. Determination of the effective transverse coherence of the neutron wave packet as employed in reflectivity investigations of condensed-matter structures. I. Measurements. *Phys. Rev. A*, 89:033851, 2014.

[90] Caroline A. Schneider, Wayne S. Rasband, and Kevin W. Eliceiri. NIH Image to ImageJ: 25 years of image analysis. *Nature Methods*, 9(7):671–675, 2012.

[91] Sindre Østby Stub, Einar Vøllestad, and Truls Norby. Mechanisms of Protonic Surface Transport in Porous Oxides: Example of YSZ. *Journal of Physical Chemistry C*, 121(23):12817–12825, 6 2017.